POLITECNICO DI TORINO

Master's Degree
in Mechanical Engineering

Master's Degree Thesis

Development of a control strategy accounting for the battery ageing and state of health for hybrid electric vehicles

Supervisors

Prof. Daniela Anna Misul

Candidate

Giuseppe Di Talia

April 2021

To my grandfather Benedetto,
my great mentor in life.

Abstract

The hybridization degree of the vehicles is getting bigger due to the felt need to fight and reduce tail pipe emissions. Internal combustion engine efficiency-oriented optimization on its own is not effective in reducing fuel consumption to withstand increasingly stringent regulatory restrictions. Hybrid Electric Vehicles (HEVs) represent a viable and absolutely-concrete alternative to the conventional powertrains. While the Battery Electric Vehicles (BEVs) are still an utopia, HEVs exist and apply to replace non-hybrid vehicles in the near future. Full-electric vehicles do not represent a credible solution for several reasons, two out of all, the limited autonomy and the absence of infrastructures on the national territory. Furthermore full-electric vehicles must be analyzed in terms of *well-to-wheels* to take into account the entire electricity production chain. The ever-growing hybridization degree of the powertrain requires intense research activity. One of the biggest bottleneck that hinders the HEV proliferation is definitely represented by the on-board energy system. Battery capacity and performance must be the best possible to accommodate the transition towards e-mobility.

Battery compartment is more and more solicited and plays an increasingly central role in this transition toward renewable energy for vehicles propulsion. Also the battery represents an important cost in the total cost of the vehicle and it is clear why an health-conscious management of the electrochemical system is crucial in achieving the best possible benefit, not only in terms of fuel consumption. A severe exploitation of the electrochemical system leads to an increase in HEVs operating costs absolutely not legitimised by a costs reduction associated to the fuel consumption reduction.

Furthermore battery performances change over time and as the time goes on they decrease inexorably. Besides the "operative" reactions, within the battery there are some side, undesirable, reactions which deplete battery performance. Complex aging mechanisms take place inside the battery and involve different battery areas. These aging mechanisms are strictly related to the battery operating conditions and severely restrict battery characteristics in operation: the more severe the operating conditions of the battery the higher the aging will be.

This work proposes an innovative way of looking at the on-board energy management problem. An ageing model has been parametrized and developed in the first section of the thesis and used to solve the optimization problem in the second part. More in detail, the model chosen is an *energy-throughput-based aging model* that links the capacity fade to the operating conditions. The selection of this kind of model is not casual, rather it has been done in view of the application in a future *hybrid control strategy*. The strength of this aging-model has to be found in

its intrinsic simplicity and reliability. Moreover, this ageing model has been used in tandem with an "hybrid" version of the ECMS to find an optimal compromise between fuel consumption and battery degradation in time.

The main objective of the work is to make the traditional ECMS aware of the battery performance fade mechanisms in order to gain the maximum benefit from hybrid propulsion. The on-board electrochemical system represents an important percentage in the total cost of a HEV hence it needs to be preserved in operation. The "hybridization of the powertrain" is surely driven by the exigency to reduce fuel consumption but the battery health acquires an increasingly pivotal role in establishing the HEV control strategy. Its cost makes the battery a critical component that has to be wisely managed in order to prolong its life dwindling attached operating costs.

Acknowledgements

First and foremost I am extremely grateful to my supervisor, Prof. Daniela Anna Misul for her invaluable advice, continuous support, and patience during my thesis work. Her professionalism and plentiful experience have encouraged me in doing this work in the best possible way. Thanks for believing in me and for giving me this incredible chance.

I would also like to thank Alessia Musa, Pier Giuseppe Anselma and Claudio Maino for their technical support on my study and their cordiality in promptly dismiss my doubts. Their help has been fundamental to achieve these results.

I deeply thank my parents and my sister for their unconditional trust and endless patience. Without them I would not have been here today and surely I would not be who I am. A special thank to my father who believed in me before anyone else did. I am extremely grateful to him for the unceasing encouragement and support. Thank you for being my super hero. I am very grateful to my mother for being my safe harbor, always. Thanks for your unconditional love and boundless support that have been, and will be, the pillars of my life. I would also like to thank my sister Raffaela for her ongoing support and her profound belied in my work.

A very special gratitude to my grandmother "Mena", a fundamental figure of my life. Thanks for the infinite love and all the precious life-teachings. I would also to express my gratitude to my grandfather Benedetto, my *great mentor in life*. He really wanted to be here, with me. To him I dedicate this work.

And finally, last but by no means least, a very special thank to my half, Adele. Thanks for your incredible moral and emotional support during the last very intense years, thanks for being there with me throughout all of this.

I'd also like to extend my gratitude and appreciation to all my family members for their contribution during all of these university years.

I also place on record, my sense of gratitude to one and all, who directly or indirectly, have lent their hand in this incredible venture.

Table of Contents

List of Tables VI

List of Figures VIII

1 Introduction 1

1.1 Lithium ion battery . . . 1
1.2 Aging mechanisms of lithium-ion batteries . . . 2
1.2.1 Reactions at the carbonaceous anode . . . 4
1.2.2 Reactions at the metal oxide cathode . . . 6
1.2.3 Reaction involving other battery areas . . . 7
1.3 External factors impacting battery aging . . . 8
1.3.1 Temperature effects . . . 9
1.3.2 Charge-discharge rate effects . . . 9
1.3.3 Depth of discharge effects . . . 10
1.4 Aging diagnostic methods for LIBs . . . 11
1.4.1 Disassembly-based post-mortem analysis . . . 11
1.4.2 Curve-based analysis . . . 12
1.4.3 Model-based analysis . . . 13

2 Lifetime prediction of electrochemical systems 16

2.1 Physico-chemical ageing model . . . 17
2.2 Event-oriented ageing model . . . 19
2.3 Weighted Ah ageing model . . . 22
2.4 Life model for graphite - LiFePO4 cells . . . 24
2.4.1 Life model development for C/2 rate . . . 29
2.4.2 Life modeling for high C-rates . . . 31
2.5 Life model for a A123 Systems cell . . . 34
2.5.1 Model parametrization . . . 34
2.5.2 Unified life model for different c-rates . . . 35

3 State-of-health estimation 38
3.1 Results on different driving cycles 43
3.1.1 WLTC driving cycle 46
3.1.2 HWFET driving cycle 46
3.1.3 UDDS driving cycle 47
3.1.4 Conclusions 48
3.2 Comparison between different SoH models 51
3.3 Simulink model for SoH estimation 56
3.3.1 Aging model block 57
3.3.2 Cycles block 58
3.3.3 Instantaneous State-of-Health block 58
3.4 Simulink model for battery life estimation 60
3.5 Results on different driving cycles 61

4 Equivalent Consumption Minimization Strategy 65
4.1 HEV powertrain modeling 68
4.1.1 Equations of motion 69
4.1.2 Forward and Backward modeling approaches 69
4.2 Jeep® Renegade 4xe PHEV modeling 71
4.3 ECMS 80
4.4 Multi-Objective ECMS 84
4.5 MG power saturation level 86
4.6 MO-ECMS calibration and results 89
4.7 Gearshift strategy 96
4.8 Internal resistance analysis 100

Conclusions 105

Bibliography 107

List of Tables

2.1 Capacity fade equations at a given discharge rate. Model parameters have been obtained with the procedure explained before [18]. 31
2.2 Generalized life model: pre-exponential factor values for different c-rate values [18]. 33
2.3 $LiFePO_4$ cell data made by A123 Systems. 35

3.1 SoH lost per cycle, WLTC repetitions and expiring distance for three different SoH approaches. Results obtained considering a battery pack of 16 kWh. 43
3.2 SoH lost per cycle, number of repetitions such that SoH=0 and striking distance. Results obtained with a battery pack of 5.16 kWh. Results obtained with the SoH model of *Anselma et al.* [24]. 50
3.3 Influence of battery pack capacity on the useful battery life along the WLTC. Results obtained with the SoH model of *Anselma et al.* [24]. 51
3.4 Analytical comparison between different SoH models along the WLTC: LIB* is the *lithium ion battery* life considering a capacity of 5.16 kWh while LIB** refers to a battery capacity of 16 kWh. 55
3.5 Different SoH models and resulting mileage. 62

4.1 Results obtained with different regeneration control strategies in terms of fuel consumption, battery life and SoC at the end of the mission. Results obtained with $s_1 = [1.93,1]$ and $s_2 = 88.2$. 87
4.2 Main results of the analysis in terms of fuel consumption and battery life for the three calibration seen before. Results obtained with the *SoH* model of *Ebbensen revised*. 95
4.3 Analytical comparison between gear strategies with different induced delay. The equivalence factors used in the ECMS to obtain these results are $s_1 = [1.93, 1]$ and $s_2 = 88.2$. Gearshift strategies are compared in terms of fuel consumption, battery expiring distance, SoC at the end of the mission and number of gearshifts. 97

4.4 Fuel consumption (F.C.) and battery life (B.L.) out of the optimal SoC window ($SoC_0 = 25\%$) and within the optimal SoC window ($SoC_0 = 84\%$). Results obtained with $s_1 = [1.93,1]$ and $s_2 = 88.2$. . 103
4.5 Fuel consumption (F.C.) and battery life (B.L.) with a new calibration of the ECMS. Results obtained with $s_1 = [1.93, 1]$ and $s_2 = 81.84$. 103
4.6 Fuel consumption (F.C.) and battery life (B.L.) out of the optimal SoC window ($SoC_0 = 25\%$) and within the second SoC window ($SoC_0 = 63\%$). Results obtained with $s_1 = [1.93,1]$ and $s_2 = 88.2$. . 104
4.7 Fuel consumption (F.C.) and battery life (B.L.) with a new calibration of the ECMS. Results obtained with $s_1 = [1.93, 1]$ and $s_2 = 87.5$. 104

List of Figures

1.1 Schematic illustration of the lithium-ion battery chemistry with a composite of graphite and SiO_x as active material for the negative electrode, a lithium transition metal oxide as active material for the positive electrode, and a liquid electrolyte based on organic carbonates [1]. 2

1.2 Aging mechanisms classification [2]. 3

1.3 Anodic reactions during different charging operations: (a) initial SoC (50%), (b) fully charged battery under normal conditions, (c) high rate charging operation and (d) overcharging [2]. 5

1.4 Charge/discharge profiles measured at 1 C_{nom} and 25 °C for cells under storage at SOC_{nom} = 100% and at temperature (a) 30 °C, (b) 45 °C, and (c) 60 °C [7]. 8

1.5 (a) Development of the relative discharge capacity versus EFC for a graphite//NMC lithium-ion cell; (b) Nyquist plots of the impedance and (c) slow discharge curves referring to the three spots in (a): New cell (blue), before the start of nonlinear aging characteristics (cyan) and after the occurrence of these (green) [12]. 10

1.6 (a) IC curves and (b) DV curves of NCA battery for different cycle number [2]. 12

1.7 Relationship between a) EIS spectrum, b) AR-ECM and c) ageing mechanisms [16]. 14

2.1 Physico-chemical ageing model [17]: general approach. 17

2.2 Equivalent circuit diagram of the positive electrode (left-hand side of the figure: grid; right-hand side: electrical path way through the electrolyte to the negative electrode). Electrode is split into three vertical levels and three horizontal levels within the active mass [17]. 18

2.3 Test matrix used in [18] to build the cycle life model for $LiFePO_4$ battery. Test matrix for accelerated cycle life study. Two cells are tested for each condition. The numbers in the test matrix indicate the number of cycles attained by the cell. Green background cells were still cycling when the paper was written while the red ones have reached end of life conditions. 25
2.4 Discharge curves of the battery cells cycled at three different conditions: (Cell A) 90% DOD, C/2, 0°C; (Cell B) 90% DOD, C/2, 45°C, and (Cell C) 90% DOD, C/2, 60°C. These results are extracted from [18]. 26
2.5 (a) Capacity retention at 60°C and a discharge rate of C/2 plotted as function of cycle number, data shown for 90, 80, 50, 20 and 10% DOD. (b) Capacity retention at 60°C and a discharge rate of C/2 plotted as function of time (days), data shown for 90, 80, 50, 20, and 10% DOD. The images have been extracted from [18]. 27
2.6 Image taken from [18]. Fit achieved when using equation to predict capacity loss as a function of temperature. Capacity loss is plotted as function of Ah throughput at 0, 15, 45, and 60 °C. *Linearity is obtained for each temperature level.* 28
2.7 Eq.(2.7) to determine the fitting parameters for the life prediction model in which $ln(Q_{loss})+E_a/RT$ is plotted as a function of ln(time). The activation energy was obtained from the best-fit values determined by non-linear regression, R^2. The slope and intercept of the linear fitting correspond to the power law factor, z, and the pre-exponential value, A, respectively. 29
2.8 Simulation of cycle-life model prediction model (line) and experimental data (dots) at 15, 45, 60 and a C/2 discharge rate. *Source:* [18]. 30
2.9 Model simulation results (lines) and experimental results (dots) at 2C (a), 6C (b) and 10C (c) discharge rates. Image taken from the paper of *Wang et al.* [18]. 32
2.10 Linear interpolation of the experimental data sets. The blue points represent the values of the pre-exponential factors determined by *Wang et al.*in [18].Pre-exponential factor [-] as function of c-rate h^{-1}. 34
2.11 Percent of capacity loss as function of total *Ah throughput* for different c-rate values. 36
2.12 Percent of capacity loss versus total Ah throughput: check with [18]. 37

3.1 Influence of battery *c*-rate (or equivalently battery power) on number of cycles before end-of-life. 40
3.2 *State-of-health* trajectories in time for different *c*-rate values. 40

3.3 Speed profile of the WLTC (upper plot), cell current in time (middle plot) and *State-of-health* in time (lower plot). Results obtained with a battery pack of 16 kWh and using the procedure indicated in [23]. 41
3.4 *State-of-health* trajectories in time along the WLTC. Results obtained with a battery pack of 16 kWh. (a) *State of Health* trend obtained with the procedure indicated in [23]. (b) *State of Health* trend obtained with the procedure of *Anselma et al.* [24]. 42
3.5 Speed profiles for different driving cycles: WLTC (upper plot), HWFET (middle plot), and UDDS (lower plot). 44
3.6 WLTC: speed profile in time (upper plot), current profile and C-rates in time (middle plot), and SoH variation in time (lower plot). Results obtained with a battery pack of 5.16 kWh. The approach used is that of *Anselma et al.* [24]. 46
3.7 HWFET: speed profile in time (upper plot), current profile and C-rates in time (middle plot), and SoH variation in time (lower plot). Results obtained with a battery pack of 5.16 kWh. The approach used is that of *Anselma et al.* [24]. 47
3.8 UDDS: speed profile in time (upper plot), current profile and C-rates in time (middle plot), and SoH variation in time (lower plot). Results obtained with a battery pack of 5.16 kWh. The approach used is that of *Anselma et al.* [24]. 48
3.9 State of Health trajectories in time for different driving cycles: WLTC (red), HWFET (blue), and UDDS (green). Results obtained with a battery pack caapcity of 5.16 kWh. The SoH model used is that of *Anselma et al.* [24]. 49
3.10 *SoH* trajectories in time for different driving cycles and with different models. In blue the model of *Ebbensen et al.* [23]. In green the model of *Anselma et al.* [24]. In yellow the model of *Ebbensen revised*, this model considers both N_{real} and N_{EOL} as charge-discharge like. . . . 52
3.11 WLTC: (a) comparison between different *SoH* models: in blue the model of *Ebbensen et al.* [23], in green the model of *Anselma et al.* [24], in yellow the model of *Ebbensen revised*, this model considers both N_{real} and N_{EOL} as charge-discharge like. In (b) comparison between Mod1 (red) and *Anselma et al.* model (dashed blue). Battery pack capacity: 5.16 kWh. 53
3.12 HWFET: (a) comparison between different *SoH* models: in blue the model of *Ebbensen et al.* [23], in green the model of *Anselma et al.* [24], in yellow the model of *Ebbensen revised*, this model considers both N_{real} and N_{EOL} as charge-discharge like. In (b) comparison between Mod1 (red) and *Anselma et al.* model (dashed blue). Battery pack capacity: 5.16 kWh. 54

3.13 UDDS: (a) comparison between different *SoH* models: in blue the model of *Ebbensen et al.* [23], in green the model of *Anselma et al.* [24], in yellow the model of *Ebbensen revised*, this model considers both N_{real} and N_{EOL} as charge-discharge like. In (b) comparison between Mod1 (red) and *Anselma et al.* model (dashed blue). Battery pack capacity: 5.16 kWh. 54
3.14 Simulink model to evaluate the SoH instantaneous variation on different driving cycles. The inputs for the model are the current and temperature profiles. The outputs are the instantaneous SoH variations (for two different SoH methods). 56
3.15 Aging model block to compute the maximum *amp-hours* processable by the battery before EOL. 57
3.16 Total number of cycles block. 58
3.17 Instantaneous State of Health block. 59
3.18 Battery life block. 60
3.19 WLTC: speed profile in time (upper plot), current profile in time (middle plot), and SoH in time (lower plot). 62
3.20 HWFET: speed profile in time (upper plot), current profile in time (middle plot), and SoH in time (lower plot). 63
3.21 UDDS: speed profile in time (upper plot), current profile in time (middle plot), and SoH in time (lower plot). 63
3.22 Uphill real driving conditions, starting from the upper part: speed profile in time, current versus time, altitude profile in time, and SoH in time. 64
3.23 Downhill real driving conditions, starting from the upper part: speed profile in time, current versus time, altitude profile in time, and SoH in time. 64

4.1 Information flow in a forward simulator [25]. 70
4.2 Information flow in a backward simulator [25]. 70
4.3 Source: *https://www.jeep-official.it/4xe-ibrido/renegade-4xe*. (a) Jeep® Renegade 4xe Plug-In Hybrid and (b) P4 architecture insights and real on-board implementation. 72
4.4 Schematic representation of a P4 Hybrid Electric Vehicle architectures. Source: *https://www.mathworks.com/help/autoblks/ug/explore-the-hybrid-electric-vehicle-p4-reference-application.html* 73
4.5 ICE map: *brake specific fuel consumption* as function of torque and engine speed. The full load curve is reported in red. 75
4.6 MG map: *MG efficiency* as function of torque and engine speed. . . 76
4.7 Equivalent circuit model of the battery [26]: U_{oc} is the open circuit voltage while R_i is the equivalent internal resistance. 77

4.8 Signal flow in the simulation model. 79
4.9 Energy path during discharge (a) and charge (b) in a parallel HEV [25]. 81
4.10 ECMS algorithm flow [25]. 82
4.11 MG power saturation level: (a) MG power in [kW] in time for different control candidates (43%, 57%, 70%, 85%, 100%) and (b) *c*-rate [1/h] in time for different control candidates (43%, 57%, 70%, 85%, 100%). The driving cycle considered is the WLTC. 86
4.12 Motor-Generator unit power in time for different regeneration-torque control-strategies: (a) no regeneration control; (b) regeneration control with one control variable (u); (c) regeneration control with two control variables. 88
4.13 Original ECMS, $s_1 = [1, 1]$ and $s_2 = 0$. Regeneration-torque control with u. (a) *State-of-Charge* trend in time along the WLTC and (b) *State-of-Health* trend in time along the WTLC. 89
4.14 Original ECMS: operating points on the ICE map (a) and on the electric machine map (b). 90
4.15 $s_1 = [2.12, 1]$ and $s_2 = 100$. Regeneration-torque control with u. (a) *State-of-Charge* trend in time along the WLTC and (b) *State-of-Health* trend in time along the WLTC. 91
4.16 $s_1 = [2.12, 1]$ and $s_2 = 100$. Operating points on the ICE map (a) and on the electric machine map (b). 92
4.17 $s_1 = [1.93, 1]$ and $s_2 = 88.2$. Regeneration-torque control with u. (a) *State-of-Charge* trend in time along the WLTC and (b) *State-of-Health* trend in time along the WTLC. 93
4.18 $s_1 = [1.93, 1]$ and $s_2 = 88.2$. Operating points on the ICE map (a) and on the electric machine map (b). 94
4.19 Pareto front between fuel economy and battery life for different s_1 values. Each front has been obtained by sweeping the equivalence factor s_2 (0, 20, 40, 60, 80, 100, 150, 200). 96
4.20 Gearshift strategy with 1 [s] delay in time. 97
4.21 Gearshift strategy with 2 [s] delay in time. 97
4.22 Gearshift strategy with 3 [s] delay in time. 98
4.23 $s_1 = [1.93, 1]$ and $s_2 = 88.2$. In (a) operating points on the ICE map with 2 s delay in the gearshift; (b) operating points on the MG map with 2 s delay in the gearshift; (c) operating points on the ICE map with 3 s delay in the gearshift; (d) operating points on the MG map with 3 s delay in the gearshift. 98
4.24 Engine speed [rpm] with 1 [s] delay (a) in the gearshift strategy; (b) engine speed [rpm] with 2 [s] delay in the gearshift strategy; (c) engine speed [rpm] with 3 [s] delay in the gearshift strategy. 99

4.25 Battery internal resistance as function of the c-rate and the *State-of-charge* during discharging operation. 100
4.26 Battery internal resistance as function of the c-rate and the *State-of-charge* during charging operation. 101
4.27 Internal charging resistance, red, and internal (discharging) resistance, blue, as function of the *state-of-charge* of the battery. Identification of the local minimum. 102

Chapter 1

Introduction

Lithium-ion batteries are now the dominant rechargeable technology in the market.For their high energy and power densities they have met with a great success both in academia and industry, which has led to a steady and constant improvement in their characteristics and performances accompanied by an important reduction in their cost. They are largely adopted in portable electronics (e.g., cellular phones, digital cameras, laptop) and are considered as the best candidates for the electric mobility (e.g., electric vehicles (EV) and hybrid electric vehicles (HEVs)).

Unfortunately also lithium-ion batteries, as other electrochemical systems, suffer capacity and power fade during both cycling and storage. Aging becomes crucial for EVs and HEVs applications where longer lifetime is requested. Capacity fade is mainly associated to different processes taking place within the battery such as: the loss of cyclable lithium, the loss of active materials and impedance increase of the cell (SEI film). Besides the cycling performance also storage performances are important. Researchers usually talk about cycle aging and calendar life aging.

1.1 Lithium ion battery

Efficient energy storage is considered crucial for the transition to renewable energy sources and definitely electrochemical energy storage technologies play a central role to make this transition physically possible. Lithium-ion batteries are nowadays the technology suitable for many different application: from the everyday electronics to the electric vehicle. Their success has to be traced back to their very high energy and power density, long cycle life, high safety and the continuous decreasing cost.

The revolution in the Li-ion battery was the substitution of lithium metal as an anode active material by carbonaceous compounds, mostly graphite. Moreover Li-ion batteries are better than other commercial rechargeable batteries in terms of gravimetric and volumetric energy.

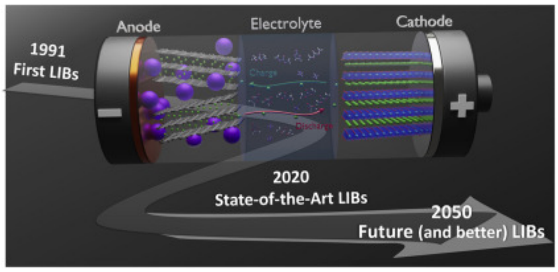

Figure 1.1: Schematic illustration of the lithium-ion battery chemistry with a composite of graphite and SiO_x as active material for the negative electrode, a lithium transition metal oxide as active material for the positive electrode, and a liquid electrolyte based on organic carbonates [1].

A Li-ion battery is constructed arranging Li-ion cells in parallel, to increase current, or in series, to increase voltage, or combined configurations. A Li-ion cell is constituted by a cathode, the positive electrode, an anode, which is the negative electrode and an electrolyte that contacts the two electrodes. The two electrodes are isolated from each other by a separator which allows the exchange of lithium ions between the electrodes but not electrons.

During the charging phase, the two electrodes are connected externally to an external electrical supply. The electrons are forced to leave the cathode moving towards the anode and they move externally. Similarly lithium ions move toward the anode but internally. In this way the external energy is stored inside the battery in the form of chemical energy in the anode and cathode materials with different chemical potentials.

The opposite happens during discharging operation: electrons move from the anode to the cathode externally, doing work on the external load connected, and the lithium-ion move toward the cathode internally, through the electrolyte. This is also known as "shuttle chair" mechanism, where the Li-ions shuttle between the anode and the cathode during charging and discharging phases.

1.2 Aging mechanisms of lithium-ion batteries

Batteries convert chemical energy in electrical energy through electrochemical reactions and they are widely used in very different field and applications. Among all the available technologies definitely Li-ion batteries have taken over for their improved performances with respect to the traditional technologies such as high working voltage and long cycle life.

For a more conscious and wise use of lithium-ion batteries special requirements have been placed on battery management strategy (BMS), especially in terms of all-climate, all-electricity ranges, full lifetime and high accuracy battery state estimation like the state of charge (SoC), state of health (SoH) and others. The estimation of these parameters is crucial for the battery optimal management.

Battery performances change in time and they progressively decrease. This degradation phenomenon unfortunately can not be stopped and completely neutralized but only slowed down to preserve longer battery characteristics in time. Obviously if the battery properties change in time also the performances of the vehicle, on which battery is installed, change as well. Not only performances of the vehicle will be limited but also some safety issues may appear.

Data collected on-board do not allow for precise battery ageing status estimation. It is necessary to study battery aging events for the establishment of a connection between the degradation of the battery external characteristics and internal side reactions, in order to provide reliable solutions to predict remaining useful life (RUL), estimate SoH and guarantees safe EV operations.

Until a few years ago we did not know exactly what was going on inside the battery and only with the advent of new and sophisticated technologies we are able to describe precisely what happens inside the battery and aging mechanisms have been better understood.

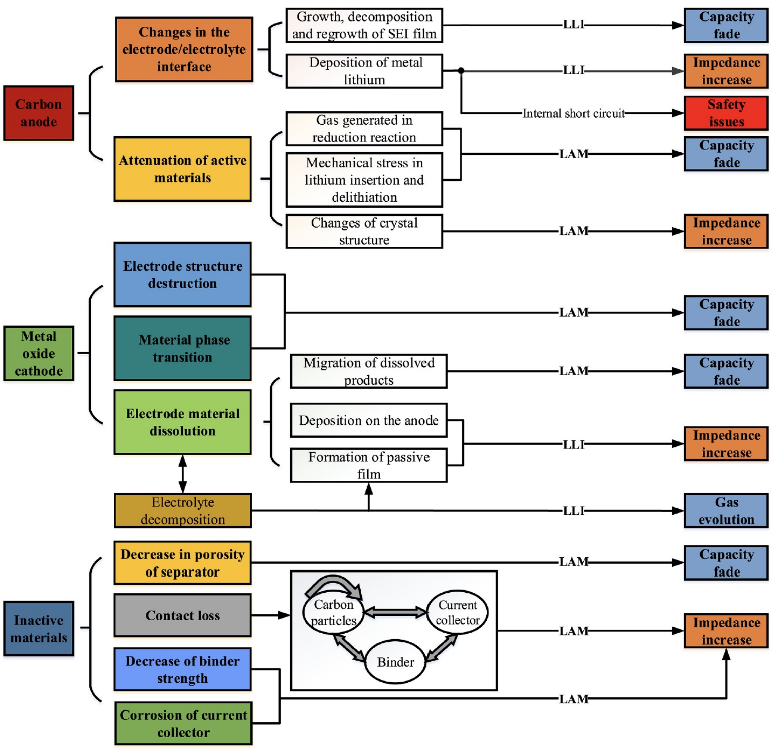

Figure 1.2: Aging mechanisms classification [2].

A lithium ion battery mainly consists of an anode (graphite), a metal-oxide cathode, a lithium salt electrolyte, and a separator that only allows lithium ions passage. The life of the battery comprises both the cycle life and the calendar life. The idea is that during the operation of the battery we have some side reactions other than main reactions that jeopardise battery power and capacity with a consequent increase in the internal resistance of the battery as the number of cycles increases. This is the cycle aging: cycle aging in mainly related to the number of charge/discharge cycles made by the battery. The calendar life, instead, is strongly related to the chronological age of the battery.

In fig.1.2 extracted from [2] the aging mechanisms happening inside the battery are classified according to the interested area of the electrochemical system. Moreover in the same figure it is also possible to see what are the external characteristics of the battery eroded by the aging mechanisms. *Xiong et al.* in [2] also divides these reactions into two main aging modes, the loss of lithium inventory (LLI) and the loss of active material (LAM).

The main aging mechanisms are surely the formation of the *solid electrolyte interface* (SEI) film at the electrode/electrolyte surface, lithium deposition, electrode structure decomposition, dissolution of active material and electrolyte decomposition. Most of the aging mechanisms occur at the positive and negative electrodes. Also the reaction involving the electrolyte are quite dangerous for the battery while the reactions on inactive materials contribute less to battery aging.

There are two kind of capacity loss within the storage process: one is reversible and the other one is irreversible. The first mechanism of capacity loss is related to self-discharge and the other one is mainly due to the changes in battery storage conditions. Calendar aging happens when the cell is stored without electric load [3]. Obviously the second kind of capacity loss happens irreversibly and the capacity lost cannot be re-established or restored in any way.

1.2.1 Reactions at the carbonaceous anode

The main reaction involving the anode is the formation of the SEI film that more precisely is a process of formation, growth, decomposition, and regrowth of the SEI film. This mechanism not only causes loss of lithium inventory also the anode/electrolyte surface diffusion resistance is likely to increase. When the battery is first charged a primary formation of SEI film is going to happen due to the reduced electrolyte on the anode surface.

It is convenient to underline that the onset electrolyte potential of SEI film formation is not constant but is strongly related and linked to the composition of the electrolyte. Also the presence of additives within the battery can modify the above mentioned potential [2].

As said before this formation mechanism is not straightforward in the sense that it is not simply a formation process. This process comprises several reactions which involve various components in the electrolyte. SEI film formation is a quite complex mechanism and it is quite difficult to isolate the single reaction involved within the process. The result of this mechanism is the formation of a film *which is roughly composed of the salt degradation products (inorganic components) and the partial or total reduction products of electrolyte solvent (organic components) [2].*

The formation of the SEI layer between the negative electrode and the electrolyte hinders the transition of the lithium ions from one electrode to the other. This will lead to LLI ageing mechanism since the amount of intercalated and deintercalated lithium ions during charging and discharging is reduced.

Furthermore the chemical structure, firmness and stability of the *solid electrolyte interface* mainly depend on the composition of the electrolyte and electrode but current and temperature play a crucial role. SEI film formation cannot be avoided, to retard battery aging it is convenient to maximize the stability of the film for example by using proper additives and think properly to the anode surface.

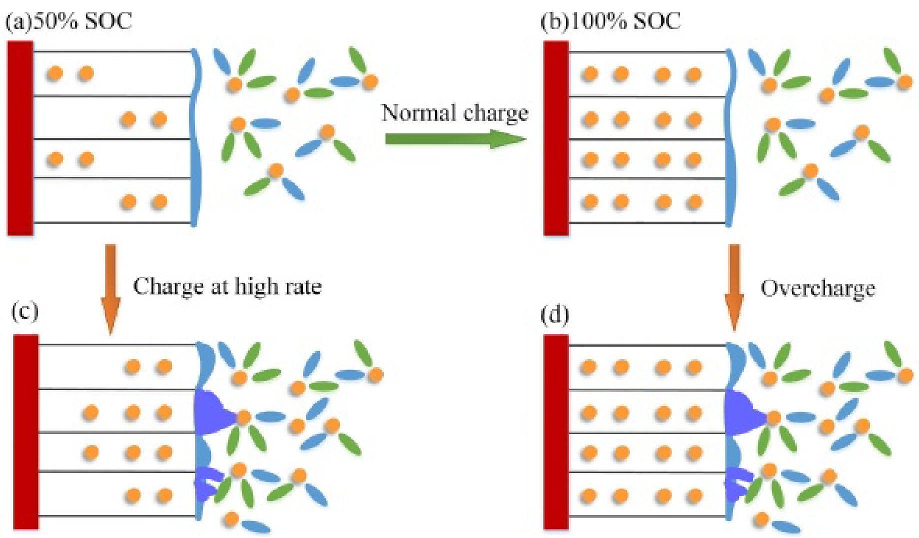

Figure 1.3: Anodic reactions during different charging operations: (a) initial SoC (50%), (b) fully charged battery under normal conditions, (c) high rate charging operation and (d) overcharging [2].

The deposition of metal lithium at the anode usually happens during harsh operating conditions like high charging rate and overcharging [4]. In fig.1.3 [2] it can be seen that lithium deposition does not happen under normal operating conditions. During extreme charging conditions instead lithium-ion enrichment is likely to happen at the anode/electrolyte interface. In these conditions the solubility of lithium ions in the liquid phase (electrolyte) greatly exceeds the solubility of lithium ions in the solid phase (carbonaceous anode). Lithium deposition verifies because the solubility of lithium ions in the liquid phase becomes bigger than the solubility in the solid phase (carbonaceous anode). The liquid phase (electrolyte) house an higher amount of lithium ions and lithium deposition can be encountered. This phenomenon brings to a series of problems. Firstly metal lithium deposition intensifies the anode polarization and somehow restrains anode performances. Furthermore metal lithium on the anode triggers some other side reactions together with the electrolyte. Another part of metal lithium could sink in the cell threatening safety during cell operation. This lithium foundering might create a short-circuit within the cell if lithium dendrites emerge withing the electrolyte giving rise to significant safety concerns.

Attenuation of active materials, fig.1.2, includes gas generated in reduction reaction, mechanical stress in lithium insertion and delithiation and changes of crystal structure. Lithium inclusion (insertion) and the subsequent delithiation, as well as the gas generated during anodic reduction reaction, generates important mechanical stress in the anode. When lithium-ions are *inserted* in the anode, graphitic planes move away from each other and this fractures the SEI film (on the outer surface of the anode). If the SEI film is cracked then part of "anodic active material" contacts the electrolyte generating a new SEI film, leading to intense *lithium consumption*. If lithium is consumed for these side reaction an irreversible capacity loss is observed.

The evolution of passive layers, i.e. the solid electrolyte interphase (SEI) at the anode and the solid permeable interphase at the cathode (SPI), takes on a key role in the aging of lithium-ion cells. Whereas the SEI ideally prevents any further reduction of the electrolyte at the anode after formation, the electrolyte is continuously oxidized at the cathode due to the SPI's incapability of full passivation. As the thickening and reconstruction of passive layers consume active lithium, there is a direct correlation to capacity loss [15], [16], [17], [18], [19], [20]. Under extreme operational conditions such as a high state of charge (SoC) or high temperatures, these layers can even isolate active material by growing into its porous structure or clog the separator's pores [16], [21].

1.2.2 Reactions at the metal oxide cathode

As illustrated in fig.1.2 the main reactions at the cathode are: electrode structure decomposition, material phase transition, electrode material dissolution. According to *R. Xiong et al.* the dissolution of active material is one of the most dangerous for battery cycle aging since this reaction is coupled with the migration of the dissolved products and the deposition at the anode. The dissolution reaction happening at the cathodic side of the cell quickens the electrolyte decomposition intensifying the formation of the *cathode electrolyte interface* CEI film.

According to *Balakrishnan et al.* in [5] the dissolution of Mn-based cathode is the most intense compared with the Ni-based cathode.

The CEI film is thinner than the SEI film, generally it does not entirely cover the cathode surface. However the consequences of the CEI film are very similar to that of the SEI film: as the film growth proceeds at the cathode/electrolyte interface the internal resistance increases as well as the cathode polarization.

Cation mixing and lithium vacancies are at the base of the cathode structural destruction. Some transition metal ions (Ni^{2+}, Fe^{2+}) and lithium ions have quite similar radius and this is the reason why the cation mixing happens at the transition metal cathode. This mechanism not only reduces battery capacity (some lithium ions become unable to intercalate) but also prohibits the diffusion of lithium ions leading to an increase in the overall battery polarization.

Also some phase transitions of the cathodic material may appear within the battery as aging goes on. Some of these phase transitions result in very severe mechanical stresses that sharply limit battery capacity.

1.2.3 Reaction involving other battery areas

Reactions at other parts of the battery mainly take place on the inactive materials such as current collectors, separators, conductive agents, and binders. Current collectors and binders will be consumed as the battery is progressively cycled. This corrosion mechanism results in a resistance increase and a contact loss with active materials [2]. Also, the separator within the cell acts as channel for ions, and its porosity change affects the ion through-rate hence battery capacity.

Battery storage can also reduce battery capacity due to its self-discharge, and some of the reduced capacity can be recovered through battery charging. Battery self-discharge can be caused by many factors, such as internal or external electron leakage, electrolyte leakage, electrode/electrolyte reactions, partial dissolution of active material, electrode passivation and mechanical decomposition [6]. Among those factors, the loss of active lithium ions, which is manifested by the growth of the passive film at the electrode/electrolyte interface, dominated the performance degradation during battery storage. It is pointed out by *Kassema et al.* [7] that the reconfiguration of SEI film at the graphite anode stored at a potential of 3 V is mainly driven by partial dissolution and secondary reaction with the electrolyte.

Furthermore *Kassema et al.* in [7] stored different graphite/LFP cells under 3 different conditions of temperature (30 °C, 45 °C, 60 °C) and SoC (30%, 65%, 100%) for 8 months. After 8 months with various non destructive electrochemical tests they study calendar aging phenomena. After 8 months-storage all of the cells exhibited capacity fade. The magnitude of capacity fade depends to a large extent on the temperature and to a lesser extent on the SoC level. Lithium loss was identified by *Kassema et al.* as the principal source of capacity fade. This lithium loss is a direct consequence of some side reactions happening at the anode (growth of the SEI film). Also the existence of reversible capacity loss suggests that also the cathode is subject to some side reactions which by the way are less important than the reactions involving the anodic side.

Fig.1.4 taken from [7] shows the charge/discharge profiles of 3 different cells at different storage periods at a fully charged state ($SoC_{nom} = 100\%$) and at temperatures (a) 30°C, (b) 45°C, and (c) 60°C. Upon storage, the cells stored at 45°C and 60°C undergoes capacity fade [7], which is higher for the cell stored at 60°C.

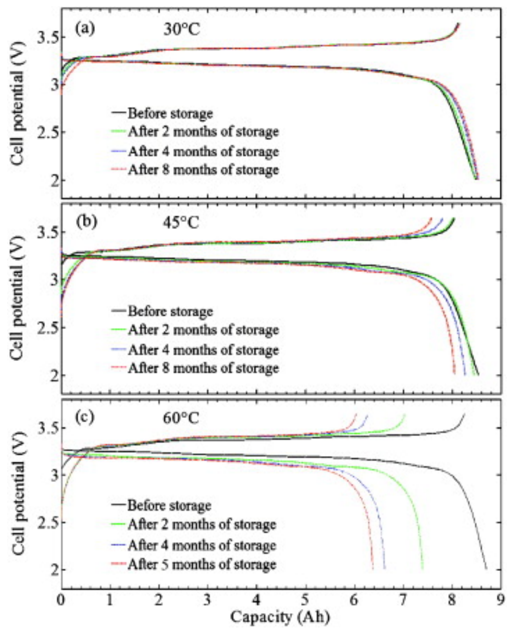

Figure 1.4: Charge/discharge profiles measured at 1 C_{nom} and 25 °C for cells under storage at $SOC_{nom} = 100\%$ and at temperature (a) 30 °C, (b) 45 °C, and (c) 60 °C [7].

1.3 External factors impacting battery aging

The study of capacity and power fade mechanisms by itself is not effective to fully understand and model battery aging mechanisms: a more in-depth investigation is needed to quantify and describe lithium-ion battery aging. Several experimental evidences prove that the aging rate and the *remaining useful life* (RUL) of the battery strongly depend upon external factors such as temperature, charge-discharge rate and depth of discharge. These factors are also used to accelerate aging tests.

In the following the effects of temperature, charge/discharge rate and depth of discharge will be investigated and make explicit.

1.3.1 Temperature effects

As shown in many tests, temperature plays a crucial role in determining battery capacity fade [8, 9]. *Rodrigues et al.* in [8] find that thermal fragility of the SEI film is one of the most important source of characteristics dacay in graphitic anodes. The researchers in [8] demostrate that the SEI can be strengthened by moving the formation cycle at higher temperature levels. Under these conditions infact it is possible to recreate a ticker and more protective layer to somehow retard aging.

Moreover the dominant aging mechanisms change for the different temperature ranges. When the temperature is above 25 °C, the higher the temperature the stronger the aging rate. For temperature level below 25 °C instead the lower the temperature the higher the aging rate, as demonstrated by *Waldmann et al.* in [10].

For temperature level lower than 25°C, lithium plating at the anode becomes predominant and this lithium-covering can hinder the intercalation dynamics of lithium ions. Moreover at such low temperature level lithium plating can give rise to serious safety hazards.

For temperature levels higher than 25°C, the reactions that determine and drive battery aging are those of thickening of SEI film and degradation of the cathode. In [11] *Guan et al.* find that the capacity degradation associated to cathode degradation at 45°C is 10 times higher than that of 25°C. High temperatures make the SEI film brittle and could hinder anode performances.

1.3.2 Charge-discharge rate effects

As the C rate rises, lithium covering and deposition involve the anode surface, accompanied by structure attenuation. The charge-discharge rates would deeply affect the time when the inflection point is reached on the battery capacity retention curve. When the inflection point is reached battery aging enters in the non-linear zone fig.1.5 extracted from [12]. Smaller charge rate and larger discharge rate can retards the emergence of the inflection point. A small charge rate tends to decrease the over-potential and inhibit lithium plating, and a large discharge rate helps to avoid severe delithiation of the anode [12].

According to *Schuster et al.* in [12] the evolution of passive layers (the *solid electrolyte interphase* and the *solid permeable interphase* (SPI) at the cathode) plays a vital and crucial role in lithium ion battery aging. While the SEI film potentially prevents further electrolyte reduction (avoiding active materials to contact electrolyte) the SPI is not capable of full passivation and electrolyte will be continuously oxidized at the cathode side. As discussed above the consumption of active lithium is one of the most important reason of batter aging. Under extreme operating conditions (e.g., high SoC and high temperature values) these layers isolate active material by growing into its porous structure[13]. *Vetter et al.* in [13] conclude that as the time goes on during cycling/storage operation the SEI penetrates into pores of the electrode and in addition may also penetrate into the pores of the separator. This may result in a decrease of the accessible active surface area of the electrode and an increase of the internal battery resistance.

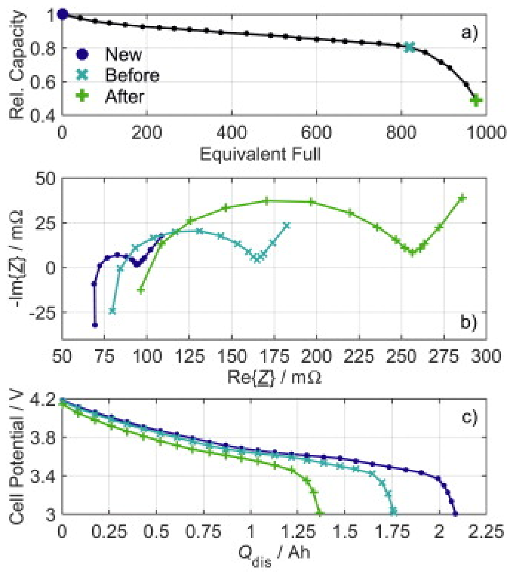

Figure 1.5: (a) Development of the relative discharge capacity versus EFC for a graphite//NMC lithium-ion cell; (b) Nyquist plots of the impedance and (c) slow discharge curves referring to the three spots in (a): New cell (blue), before the start of nonlinear aging characteristics (cyan) and after the occurrence of these (green) [12].

1.3.3 Depth of discharge effects

The cycle performances are also influenced by the *depth of discharge* (DOD) but the effect of this parameter varies with the cathode material. *Watanabe et al.* in [14] investigate the degradation of Li-ion cell during cycle with ΔDOD restriction. At the end of their analysis *Watanabe et al.* find an important result: *the deterioration was not strictly related to the upper and lower limits of DOD but to the width of the discharge cycle.* When *depth-of-discharge* is limited to 10% and 70% battery aging proceeds slower compared to a situation with DOD of 0% - 100%.

Furthermore they find that capacity fading and impedance increase were linked to ΔDOD and temperature. Even at 60 °C when ΔDOD was limited between 0-60% the effects on these two parameters turn out to be quite marginal. Conversely the effect on capacity fade and resistance increase was significant when the battery was tested with 100% DOD particularly for high temperature values.

Xiong et al. in [2] gather some indications to prevent battery aging or at least to postpone it to happen. For example *Markovsky et al.* in [15] figure out that the addition of some suitable additives in the electrolyte could be helpful and beneficial for the battery. In [15] *Markovsky et al.* prove that some common additives (e.g., VC - or Li-organo-borate complex (25 CE)) can increase the stability of the SEI film. This in turn prevent further side reaction to take place.

Obviously extreme temperature, large charge-discharge rate, and high DOD accelerate battery aging.

In [12], *Schuster et al.* find that high charge rate, low temperature, and high ΔV could accelerate the transition from linear aging to non linear aging. These conditions could shorten linear aging and speed up the non linear stage. The battery will age sharply during the non linear stage and definitely its performances vertically diminish. Lithium deposition rather than SEI film growth characterizes the non linear stage and this mechanism severely threatens safe battery operation. Since aging at low temperature risks prejudicing the safety the preheating method for batteries makes a great contribution to improve battery performance simultaneously reducing battery aging.

1.4 Aging diagnostic methods for LIBs

The aforementioned reactions severely restrict battery performances in operation both in terms of power and capacity. Diagnosis methods are essential not only to establish if the electrochemical system is compromised also they are very useful to study aging mechanisms to understand how they are going on within the battery. Nowadays there are three big families of diagnosis methods: *disassembly-based post-mortem analysis, curve-based analysis and model-based analysis.*

1.4.1 Disassembly-based post-mortem analysis

Post-mortem analysis consists in dismount aged batteries in a dedicated environment to observe each component of the batteries to determine aging mechanisms through material analysis. To be effective post-mortem analysis requires a dedicated environment to avoid as much as possible contamination and to guarantee safety during the disassembly operations. Some preliminary operations should be carried out before opening the battery: to avoid short circuit within the cell some *non-destructive tests* are used to identify the best cutting position to open the electrochemical system[2]. All of the disassembly operations have to be performed in a sealed environment filled with inert gas and suitable humidity to ensure safety and to give credibility to the test. During the disassembly process it is necessary to avoid contacting different internal battery elements to avoid cross contamination. Before proceeding with the test battery components are rinsed with dimethyl carbonate (DMC), diethyl carbonate (DEC) or ethyl methyl carbonate (EMC). According to the information we are interested in different post-mortem analysis can be carried out: morphology analysis method, composition analysis method, and structure analysis method.

Morphology analysis examines the morphology of the electrode surface and avails itself of optical microscopy, scanning electron microscopy (SEM), and transmission electron microscopy (TEM).

Composition analysis method studies the composition of the elements, the concentration distribution of elements on the surface and along with the width, and the chemical valence of surface elements.

The structure analysis focuses on the crystal structure information on the surface like for example atomic arrangement, crystal size or crystal orientation.

1.4.2 Curve-based analysis

Curve-based analysis can be performed by means of two "special" curve. Incremental capacity analysis (ICA) and differential voltage analysis (DVA) are widely used in the field of curve-based analysis. The *open circuit voltage* (OCV) curve unfortunately is not sensitive to battery operating conditions and for this reason the two aforementioned curves are born: ICA and DVA.

For the ICA the first step is to obtain the IC curve based on the battery OCV curve. This curve describes how the capacity increment $\frac{dQ}{dV}$ changes with battery voltage. The curve cannot be used as it is because of the noise, which need to be erased with a filter like the *third-order polynomial Savitzky-Golay*.

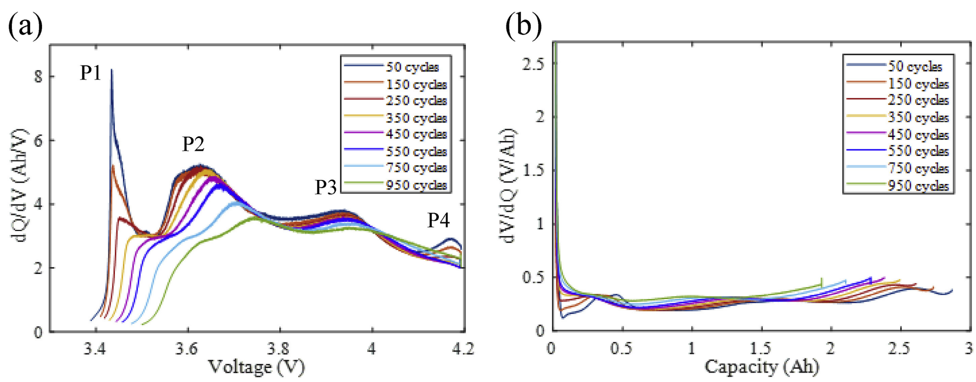

Figure 1.6: (a) IC curves and (b) DV curves of NCA battery for different cycle number [2].

As shown in fig.1.6 (a) the area between the IC curve and the horizontal axis indicates the capacity charged in the corresponding voltage interval while the peaks (numbered as P1, P2, P3, and P4) indicated various phase transition stages of the *nickel-cobalt-aluminum* (NCA) battery. The following step of the analysis is to understand the phase transitions for the two electrodes within the cell which correspond to the different peaks of the curve. For example the NCA cathode undergoes three phase transitions during battery charging: to initial hexagonal to monoclinic, monoclinic to new hexagonal, and new hexagonal to another new hexagonal. For the anode instead we have four different phase transitions. The phase transitions of the two electrodes are superimposed on the IC curve. Basically this analysis consists in different steps. The first step is to obtain the IC curve starting from the OCV curve. The following step consists in making a quantitative aging diagnosis. The diagnosis is done interpreting the IC curve in terms of changes/alterations of the magnitude, width, and position of the IC peaks in different cycles. For example the IC peaks shifting to the right (toward lower voltage values) means that the polarization resistance of the battery has increased.

Similarly the DV curve is obtained differentiating battery voltage with respect to the capacity $\frac{dV}{dQ}$ and it is used instead of IC as a diagnostic method for battery aging. It is worth to notice that the two aforementioned curves are inversely correlated meaning that the peaks of the IC curve become valleys when it comes to the DV curve. In particular the valleys of the DV curve are symptomatic of phase transitions of the electrode active material whereas a peak represents a single phase of the active material. If DV curve is used as aging diagnosis method capacity loss of each phase can be easily measured and quantified by measuring the distance between two adjacent peaks. The DV curve has an important advantage with respect to the previous mentioned IC curve since it allows quantifying degradation effects and the corresponding contribution rates more easily and promptly compared with the IC curve. Furthermore by using the DV curve we can distinguish the anode and cathode capacity loss, and determine the electrode that has a greater effect on battery aging. In practical applications these two methods are used jointly meaning that they are applied to verify the other one: it is something like saying that they are complementary.

1.4.3 Model-based analysis

Model-based diagnosis methods comprise the EIS-based method and the electrochemical parameter identification based method [2]. EIS stands for Electrochemical Impedance Spectroscopy. In the following the two methods are briefly discussed and commented.

The first mentioned method, the EIS-based method, has been developed to analyze the performance fade due to an increase in battery internal resistance.

Technically on the electrochemical system under the condition of an open circuit state a small amplitude alternating current (AC) sinusoidal potential signal is applied and the response is promptly measured. The response of the system will be a sinusoidal current response with a certain phase shift with respect to the input signal. The following step is to compute the electrochemical AC impendence in the frequency domain exploiting the sinusoidal potential signal (input) and the output signal.

This technique relates each of the resistors fitted from an Adapted Randles - Equivalent Circuit Model (AR-ECM) to conductivity losses, LLI or LAM. Using the EIS measurements, the AR-ECM is fitted based on the Non-Linear Least Squares (NLLS) algorithm [16].

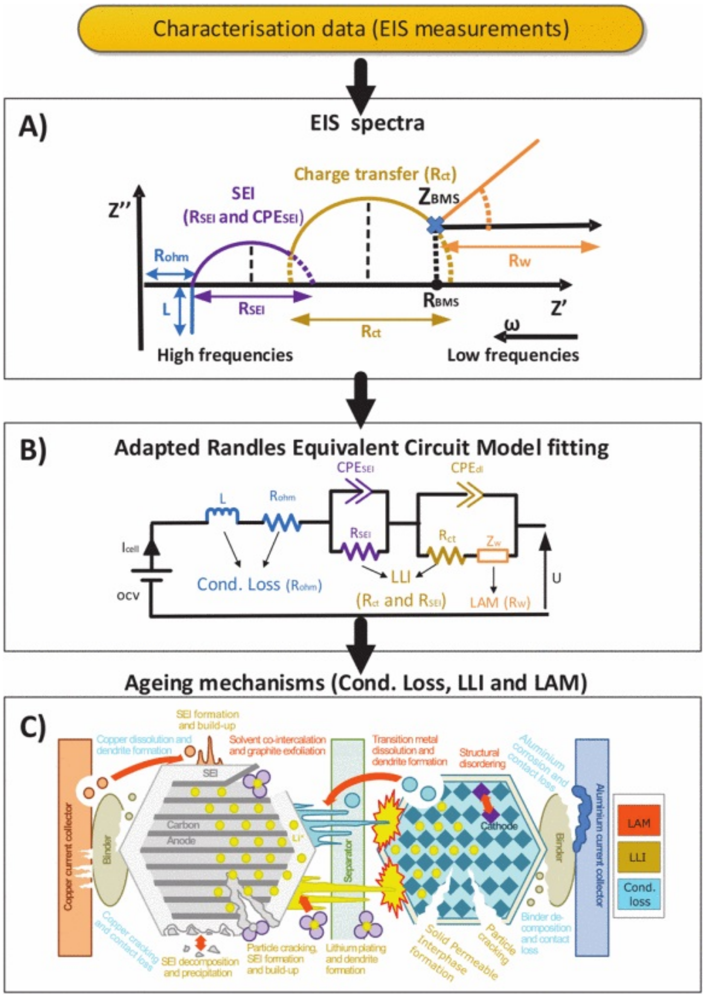

Figure 1.7: Relationship between a) EIS spectrum, b) AR-ECM and c) ageing mechanisms [16].

Fig.1.7 B) illustrates that the AR-ECM is composed of a voltage source connected in series with a resistor, an inductor and resistor and Constant Phase Elements (CPEs) parallel branches [16].

The electrochemical model (EM) instead describes the physics and the chemistry hidden within the battery such as electrochemical reactions, diffusion, migration of lithium and ohmic action. Technically speaking this method related internal battery parameters with the external characteristics. To differentiate the aging mechanisms taking place inside the battery and figuring out the corresponding aging modes it is necessary to identify, compare and interpret the EM parameters. Those parameters could be for example the volume fraction of active material, the lithium embedding rate of the electrode, the diffusion coefficient of the solid or liquid phase, and the SEI film resistance during battery aging [2].

However *quantitative aging diagnosis* and *real time on-board application* constitute two major challenges for aging diagnosis methods. It is quite complex in real applications to establish specific and robust relationships between internal aging reactions and external characteristics. The same aging mechanisms could affect different battery characteristics. Diagnostic methodologies should be able to give both qualitative and quantitative information about battery aging. Battery physics and chemistry make the determination of such relationships absolutely not trivial. Qualitative aging diagnosis methods help us in solely understanding which aging reactions are actually taking place within the battery. This information by itself is not enough in providing a complete and comprehensive overview of what is going on and how battery performances are changing. For this reason qualitative analysis should be followed by a quantitative analysis. The existing quantitative analysis consists of two steps [2]. The first one is the battery aging reactions classification and the second one is to analyze the contribution rates of the each modes which generally is expressed as the lost capacity of resistance rise. On-board application of diagnosis methods is very different from the laboratory application. The main differences are surely related with the required robustness, speed, accuracy and real time characteristics. Hence curve-based analysis and EIS-based method have drawn even more attention for on-board application and are the perfect candidates for this kind of application. *Disassembly-based post-mortem analysis* has surely the advantage of intuitive observation of the inside aging reactions. In the same time this method irreversibly destroys the battery, it is complicated and it has high experimental costs. *Curve-based analysis* instead is a non-destructive analysis thus the battery could be potentially reused immediately after the test. This method is quite flexible and versatile and has low computational efforts are required [2]. Cross-validation is needed and noise has to be carefully managed. Finally *model-based analysis* is non-destructive, versatile and very accurate. The disadvantages of this method have to be searched in its computational burden, interference between EM parameters and difficulty to measure EIS.

Chapter 2

Lifetime prediction of electrochemical systems

It is important and somehow necessary to be able to foresee the useful life of a battery in target applications in order to make sound technical and commercial decisions at the system design stage. In general to accurately predict battery lifetime other instruments have to be used besides the knowledge of ageing processes and the availability of battery models. Precise battery lifetime forecasts become crucial and extremely important for technical and commercial decision-making. On the basis of these forecasts the most suitable battery type is chosen, operating conditions are determined and replacement intervals for batteries are planned. The knowledge about the ageing processes, the stress factors that cause battery performances to diminish in time, and an understanding of the connections between the stress factors and ageing processes is fundamental in achieving a precise lifetime prediction.

Different approaches for lifetime prediction of electrochemical systems are presented and commented in the following paragraphs. Three major models [17] are used to forecast the useful life of different electrochemical energy storage devices namely: 1) physico-chemical ageing model; 2) event-oriented ageing model; 3) weighted Ah throughput ageing model.

However, when several ageing processes happen contemporary due to a complex combination of operating conditions [17] (e.g., combination of cycling, partial state of charge cycling, incomplete full charging, wide range of temperatures) attention should be payed in studying all of these interactions (between ageing processes and operating conditions). On an experimental basis is possible to reconstruct a correlation between ageing processes and lifetime forecast but only up to a certain point, as largely demonstrated in literature.

2.1 Physico-chemical ageing model

A complete and detailed physico-chemical model of the ageing process is used for time step simulation. This model gives the possibility to access some very local information such as temperature, potential, current, SoC, electrolyte concentration, etc. These parameters are also known as *state-variables* and they are the result of the operating conditions. State variables are used to somehow uniquely characterize the system under analysis. By knowing the relationship between aging effects and state variables it is possible to quantify the effect of the ageing processes at any place (and any time) within the system. It is interesting to notice that the ageing progress is incorporated within the model thus the state variables are automatically adjusted. For example if the grid resistance changes in time, the current distribution along the electrode as well as the electrolyte density at different height is automatically updated within the *physico-chemical* model.

Sauer et al. in [17] resume the general approach of this model with the scheme presented in fig.2.1. According to *Sauer et al.*, infact, this model consists of two steps. In the first step battery is modeled by means of the fundamental equations of the chemical and electrochemical reactions. The outputs of this first step are: local potential, local current density, local state of charge, microstructure of active material, local temperature, local oxygen reduction current, local corrosion current and many others. It is possible to say that the main goal of this part is to model the battery giving in output several local information to be used in the second part. The second part of the physico-chemical ageing model is in charge of quantifying ageing processes and their direct impact on battery external performance. The two sections are not isolated and separated: they are complementary. The output information of the first module are used as input in the second module and the outcomes of the second module serve to state-variables automatic adjustment.

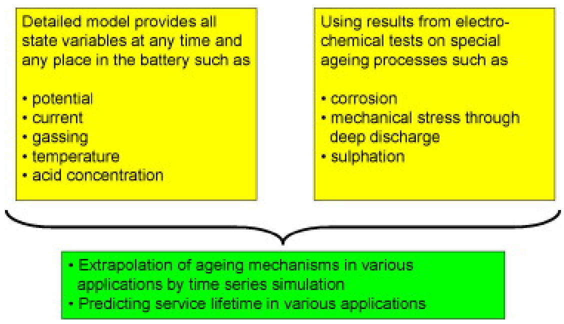

Figure 2.1: Physico-chemical ageing model [17]: general approach.

The simulation is based on a resistance network that is also named the equivalent circuit diagram (in fig.2.2, taken from [17], only the positive electrode is reported).

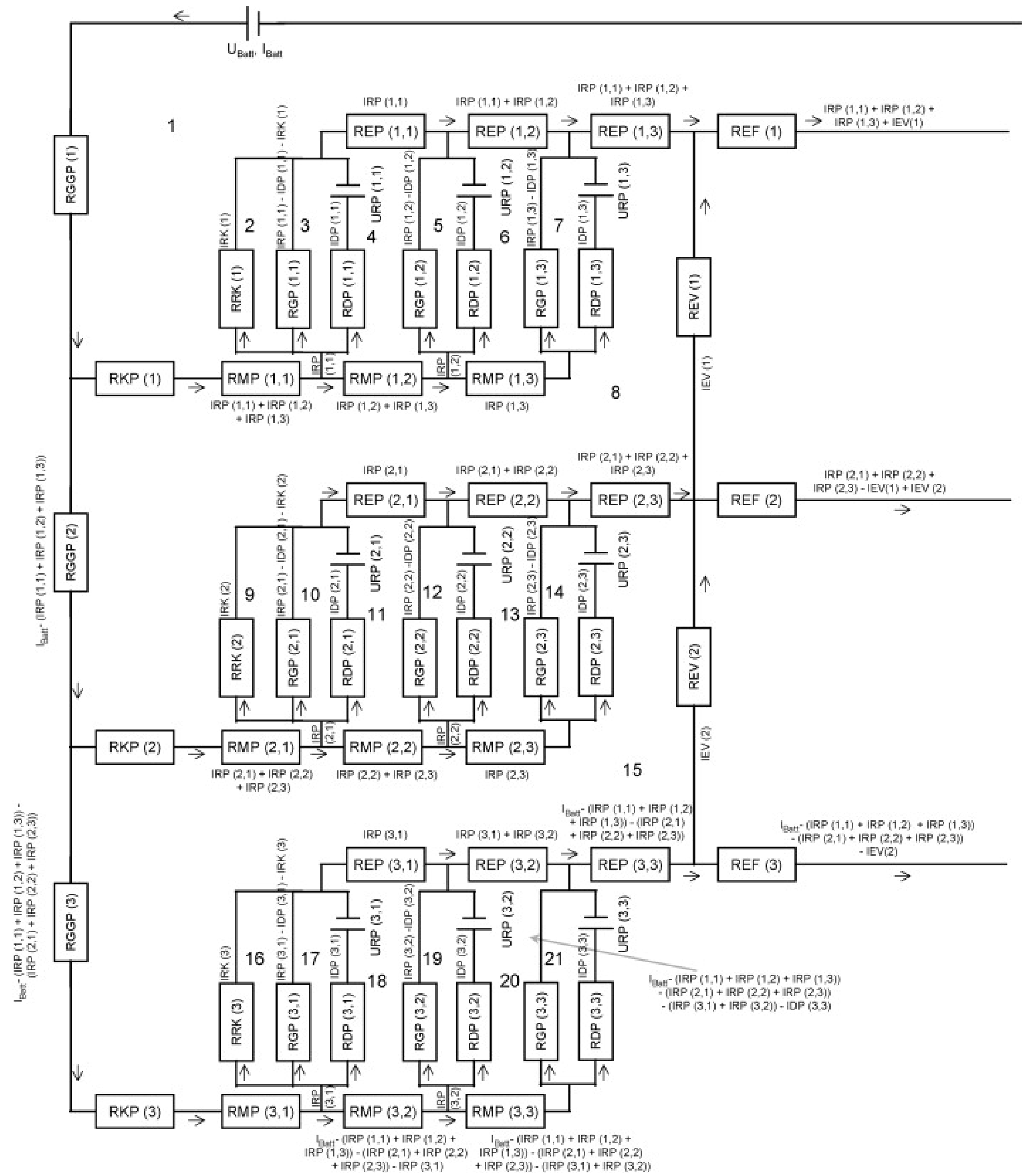

Figure 2.2: Equivalent circuit diagram of the positive electrode (left-hand side of the figure: grid; right-hand side: electrical path way through the electrolyte to the negative electrode). Electrode is split into three vertical levels and three horizontal levels within the active mass [17].

The equivalent circuit diagram is then solved at each time step and by means of *Kirchhof's laws* a full set of linear equations is obtained. *Sauer et al.* solve the equivalent circuit diagram instead of solving a set of inhomogeneous, non-linear and coupled differential equations. The solution of such a complex model can be easily obtained using the most advanced tools in the field of electronic engineering.

The model described above is only concerning the first step previously introduced of the whole physico-chemical aging model. By solving the first model, conditions at each point of time and every point in the electrodes (and electrolyte) are known. One of the advantages of this model is definitely the amount of information available. *The transfer of knowledge of the local conditions in the battery to a quantified impact on the ageing processes and battery performance in carried out in a two step approach* by *Sauer et al.* in [17]. In the first step the general dependencies of most ageing mechanisms on the state variables have to be extrapolated from the literature. In the following passage specific tests are performed in laboratory and finally this information is used to "correct" the dependencies found in literature.

From this very quick overview about the physico-chemical ageing model is clear the reason why it is the most complex model. This model deals with a plenty of local information. The physics and chemistry inside the battery are very scrupulously described. With this approach every point of each battery component is fully and completely characterized. However this in-depth modelling requires several input information.

This model requires several input information and maybe some of these requests are non-confidential data which are difficult to find/estimate. Given its intrinsic complexity it is unthinkable to use the physico-chemical ageing model in on-board application. Calculation speed is significantly lower than the two other models. Resolution of the model should not be too high otherwise the simulation time dramatically increases. On the other hand this model is quite flexible meaning that once the parameters have been identified it can be used for a great variety of operating conditions and control strategies. The physics and the chemistry behind the model allow to have more reliable and precise results with respect to the other models. Having more precise information allow to obtain better control strategies.

2.2 Event-oriented ageing model

This model takes its cue from the concept of SN or Wöhler curve after the German railway engineer who first introduced the principle as a means to determine the lifetime of railway components. This concept is associated with the concept of cumulative damage: the lifetime before breaking is estimated by assigning the incremental loss of lifetime associated with well-defined events and adding up the loss of lifetime per event [17]. In the field of mechanical engineering each event is described by one scalar value (e.g. bending moment). *Sauer et al.* renamed this scalar value as *stress factor*. If the magnitude of this stress factor changes, the number of events before breaking changes as well: the greater the induced damage the lower the number of events to breaking.

Two kinds of Wöhler curves [17] are used today to estimate the battery lifetime:

- The curve showing the number of cycles of a battery as function of the depth of discharge until the end of lifetime. Battery-makers usually provide this information in the datasheet;

- The curve showing the lifetime of a battery in days as a function of its float charging voltage or temperature;

Nevertheless, both of the aforementioned Wöhler curves are one-dimensional meaning that one only stress factor in considered as aging-inducing factor while all the other stress factors are kept constant and fixed. This assumption unluckily is not very realistic when it comes to battery and fuel cells: within these devices infact several factors contemporary happen. In real applications there is an overlap between different stress factors rather than one only stress factor.

The mathematical formulation of the *event-oriented ageing model*, Eq.2.1, is quite simple and copies exactly the mechanical formulation of cumulative damage. If $\mathrm{NE_i}$ is the number of events i occured in the observation period and $\mathrm{NE_i}^{\mathrm{max}}$ is the maximum number of events i that can occur during the lifetime of a battery until the failure occurs (under the assumption that only events i happen) the loss of lifetime can be easily evaluated.

$$LL_i = \frac{NE_i}{NE_i^{max}} \tag{2.1}$$

The portion of lifetime lost during an observation period is equal to the sum extended over all the types of events during the same "sampling" period:

$$LL = \sum_i LL_i \tag{2.2}$$

The end of lifetime is reached when LL, eq.2.2, is equal to 1. Practically speaking the meaning of eq.2.1 is that during the generic observation period a certain percentage of useful life is lost or equivalently a damage is induced within the system. The ratio in eq.2.1 compares the real number of cycles made by the battery with the potential number of cycles (under the same conditions) the battery could withstand before EOL. If the same procedure is applied also to the other conditions - events different from i - it is possible to evaluate the *cumulative damage*, eq.2.2. When this sum is equal to one end of lifetime is reached by the system.

Furthermore the use of this model is based on some assumptions [17]:

1. The loss of lifetime per event is small;

2. The loss of lifetime for a given event does not depend on the sequence/order with which events are executed;

3. The loss of lifetime related with the single event does not depend on the accumulated damage;

4. Every point of time must be assigned to exactly one event for which data from a Wöhler exist;

The first assumption is true for batteries under normal operation. Obviously this is not the case of very severe operating conditions which deplete battery performances after a few number of repetitions. For *Sauer et al.* the second assumption is fulfilled in battery practice only if the battery at the end of the event has returned to an appropriate condition.

The third assumption is the most difficult one for the researchers. In [17] *Sauer et al.* highlight the fact that in the definition of an event there is an intrinsic "allusion" with ageing: events are characterized by means of some parameters which already incorporate ageing. As a consequence ageing effects are "indirectly" considered and taken into account.

For the last assumption it is clear that a simple one-dimensional Wöhler curve is not effective to solve the problem and also the definition of each event must be carefully decided so that every point in time will be assigned to only one type of event.

In many applications battery can be considered to be subject to a combination of three different types of events: float operation, cyclic operation and cycling at a partial state of charge. The "exact" definition of event does not exist: event definition is application dependent. In [17] *Sauer et al.* define the main classes of events as follows:

- Float operation: in railway application batteries remain fully charged for a long period of time but external conditions might change. Floating mode is interrupted for example when the battery has to provide high rate discharge current to crank the internal combustion engine of the train.

- Cyclic operation: train batteries are occasionally discharged for example during *shunting manoeuvres*. Not all the battery users are disconnected from the battery and they continue absorbing power from the electrochemical system. Battery remains at very low SoC level for a few hours. Battery damage under these conditions happens very quickly. Recharging the battery always occurs via a constant current/constant voltage charging regime with I_5 and usually up to a voltage of 2.35–2.4 V cell^{-1}. In discharging operation battery current will tend to fluctuate as the loads are repetitively connected and disconnected and also during charging operations the charging current may sometimes falls below the set value as the availability of electrical power on board a train is limited.

- Cycling at partial state of charge: sometimes, a discharge cycle starts prior that battery has reached fully-charged conditions. Some undesirable reactions could happen: sulphation and acid stratification are two meaningful examples.

Cyclic operation and cycling at partial state of charge are conceptually very similar. In cycling operation battery is fully discharged and then fully charged. If the discharging process is stopped by charging currents then we talk about cycling at partial state of charge.

The weakest point of the model is surely the application-oriented definition and classification of events and information concerning the number of these events until the end of lifetime is reached.

2.3 Weighted Ah ageing model

Cycle lifetime is established by discharging the electrochemical system with a constant current to a certain DOD and a subsequent full charge under a given charging rules. The overall *Ah-throughput* until the capacity has fallen below a pre-set level is thus quantified. For lifetime prediction purposes, battery useful life corresponds to the time until the total Ah throughput - processed by the battery - is identical to the Ah throughput measured under such constant conditions. Nevertheless, real battery operating conditions might significantly differ from the test-conditions. This divergence (real operating conditions are different from standard operating conditions) makes the comparison between Ah-processed and Ah-potentially-processable meaningless: the amount of charge processed by the battery may be more or less damaging than during the standard operating conditions. The idea is that the same amount of charge might be more or less damaging in terms of battery health as function of the operating conditions under which this charge is processed. The weighted Ah ageing model literally weighs the charge processed by the battery depending on the operating conditions. The more severe the operating conditions (for battery ageing) the higher the weights the model will apply. The Ah effectively processed by the battery are then compared with the Ah-potentially-processable (experimentally obtained).

In [17] researchers take these deviations into account and make the assumption that the battery is at the end of its lifetime once the weighted Ah throughput has exceeded the expected unweighted Ah throughput which has been measured under nominal operating conditions.

Per definition [17], the end of lifetime is reached once the capacity of the battery under standard test conditions (e.g. 10 h discharge current, 25 °C) is below 80% of the nominal capacity. *Sauer et al.* use lead-acid batteries as example to explain different methods for lifetime prediction of electrochemical systems. In [17] some important considerations regarding lead-acid batteries are reported. Firstly cycling a lead-acid battery at low states of charge appears to be more damaging than cycling the same battery at high states of charge. Hence, any Ah which is charged or discharged to the battery needs to be weighted according to the SoC level. The lower the state of charge the higher this weight will be. Furthermore, *Sauer et al.* recognize that cycling of a battery while acid stratification is present is likely to result in inhomogeneous current distribution along the electrode. As a result of this uneven distribution some areas of the electrodes are stressed very much. Again, the Ah throughput needs to be weighted with a factor which depends on the degree of acid stratification. Also, long periods without a full charge of the battery are known to be detrimental as well because the sulphate crystals grow [17]. This finally leads to sulphation and capacity loss. Therefore the Ah throughput also needs to be weighted with a factor depending on the time since the last full charge. *Sauer et al.* in [17] develop a very detailed Ah throughput model for lead-acid batteries. In this model weighting factors for acid stratification, bad full charges, SOC weight and current amplitude are taken into account. The undoubted advantage of the model is the high computational speed making it suitable for system design tools where/when several systems have to be tested quickly. Additionally the structure of the model is quite simple and readily understandable: it can be easily adapted and customized for different battery technologies. Different battery technologies may have different stress factors and their quantitative impact on ageing considerably varies with battery specs. Stress factors identification and quantification are propaedeutic for aging model application and implementation. However, the model can be seen as a heuristic approach. Effectively this model does not represent ageing effects on a physical or chemical basis: the model tries to correlate stress factors with the battery performance fade. In other words, battery-makers cannot take advantage of this "simple" model to enhance battery physico-chemical technology. On the other hand this tool lends itself to all of those applications in which simulation time is considered more important than detailed information. For example this model seems to be an excellent choice for *on-board control strategies* in HEVs in which the speed in getting the information is even more important than the information itself.

2.4 Life model for graphite - LiFePO4 cells

In [18] *Wang et al.* study cycling induced capacity fade of a $LiFePO_4$ battery and a cycle life model has been realized and experimentally validated. Cell life data for ageing model construction have been gathered in a large test matrix that includes three parameters: temperature, DOD, and discharge rate.

According to *Wang et al.* at low C-rates capacity fade was mainly linked to exposure-time and temperature while the effect of the depth of discharge was practically negligible. At high C-rates, the charge/discharge rate related phenomenon become increasingly important and significantly deplete battery performance. In [18] a power law equation has been adopted: capacity loss is related to Ah-throughput - or time - by means of a power law relation whereas an Arrhenius-like relation is selected to describe temperature effect.

$LiFePO_4$ batteries are considered to be one of the best technologies for large-scale application such as automotive and space industry. Several efforts have been made both in academia and industry to study performance-fade mechanisms affecting this electrochemical system. The complexity of the problem makes everything more complex. Researchers in [18] study battery behaviour in time under different operating conditions taking advantage both of destructive and non-destructive tests and the results indicate that capacity fade in $LiFePO_4$ are mainly ascribed to *loss of active lithium* which in turn is connected with anode degradation. An optimal exploitation of the battery is enabled only by a detailed understanding of the aging phenomena happening within the battery.

In [18] *Wang et al.* develop a semi-empirical life model based on the consumption of active lithium, hence anode degradation. The researchers investigate the effect of four different parameters on battery ageing: time, temperature, DOD and charge/discharge rate. A general power law equation described by *Bloom et al.* [19], where capacity fade is connected with time through a power law relation, has been used as starting point in [18].

According to *Bloom et al.* useful cell life was strongly affected by temperature, time, state-of-charge (SoC) and change in state-of-charge (ΔSoC) [19]. During calendar life experiments, cell life was strongly influenced by temperature and time. In [19] is highlighted that the rates of area specific impedance (ASI) increase and power fade follow simple laws based on a power of time and Arrhenius kinetics. *Bloom et al.* using these two concepts model the data and finally they find that the calculated data agree well with the experimental values [19]. The calendar ASI increase and power fade data follow $time^{(1/2)}$ kinetics. This behaviour is mainly connected with the SEI film growth. Cycle life experiments made in [19] confirm this trend and in the same time indicate that power fade mechanism is more complex than layer growth.

$LiFePO_4$ cells, purchased by A123 Systems, are tested under several different conditions as reported in fig.2.3: five different temperature levels, five DOD levels, and four discharge rates. In [18] the cell capacity is de-rated to 2Ah during the definition of the DOD and c-rate.

Before proceeding with the cycling test, each cell has been characterized under four different perspectives [18]: capacity characterization, relaxation test, electrochemical impedance spectroscopy (EIS), and hybrid pulse power characterization (HPPC). For a more in-depth understanding about the characterization techniques used by *Wang et al.* the reader is referred to the complete version of [18].

	Temperature °C												
DOD (%)	-30		0		15		25		45		60		C-rate
90	1	1	2242	2240	2144	2130			1796	1661	754	518	C/2
80	1	1	2520	2520	2390		2439	563	2120	2123	1011	1006	
50	13	15	3976	3965	3827	3804			3387	3317	3355	3963	
20	2662	4979	9625	9652	9234		4711	2211 / 2204	8374	8379	9801	9821	
10	9678	12082	18579	18534	18067	17940			16235	16571	19098	19385	
	-30		0		15		25		45		60		
90	26	40							4492	4048	1276	1594	2C
80			2249 / 2315	1931 / 2197									
50					3532 / 3784	3671 / 6763							
20													
10	38733	29511									54934	54943	
	-30		0		15		25		45		60		
90			3795 / 1723	1207 / 409	700 / 480	1222 / 418							6C
80									1479	1355			
50	1114	641			4017 / 5887	8242 / 9290					1428	1854	
20													
10					36151	35898							
	-30		0		15		25		45		60		
90	56	1									274	228	10C
80			611 / 1076	1135 / 1304					683	691			
50					9648	6696							
20													
10	1	1									17511	16848	

Test Stopped   Test Ongoing

Figure 2.3: Test matrix used in [18] to build the cycle life model for $LiFePO_4$ battery. Test matrix for accelerated cycle life study. Two cells are tested for each condition. The numbers in the test matrix indicate the number of cycles attained by the cell. Green background cells were still cycling when the paper was written while the red ones have reached end of life conditions.

The test matrix of fig.2.3 is used by the authors of [18] to do some statistical evaluation of the factors affecting cycle life and in the same time it provides enough information to build the model. *Wang et al.* use capacity characterization data to quantify the capacity fade rate for the model development. Fig.2.4, taken from [18], reports the discharge curves acquired at C/2 rate for different cells tested under different conditions. It is interesting to notice, fig.2.4, that as the ageing proceeds, the measured capacities inexorably decrease although the overall shape of the curves remain quite identical.

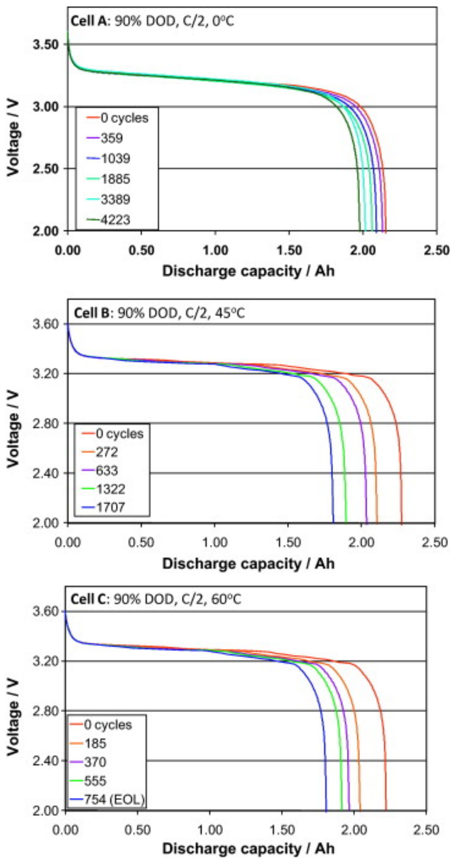

Figure 2.4: Discharge curves of the battery cells cycled at three different conditions: (Cell A) 90% DOD, C/2, 0°C; (Cell B) 90% DOD, C/2, 45°C, and (Cell C) 90% DOD, C/2, 60°C. These results are extracted from [18].

In (2.3) Q_{loss} is the lost capacity as the ageing goes on. This term depends on different elements: time, temperature, depth of discharge and charge/discharge rate.

$$Q_{loss} = f(t, T, DOD, Rate) \tag{2.3}$$

In fig.2.5 (a) [18] it is possible to see that for a given C-rate value the cell tested at DODs higher than 50% reach *end-of-life* condition sooner than those cycles at DODs lower than 50%. In fig.2.5 (b) [18], instead, the same data is plotted as function of time. By having a closer look to fig.2.5 (b) it is possible to realize that DOD has a very marginal influence on capacity fade. Thus, *Wang et al.* conclude that the effect of cycling time is more important than DOD. The little effect of

DOD suggest the authors of the paper to neglect DOD impact in the definition of the model.

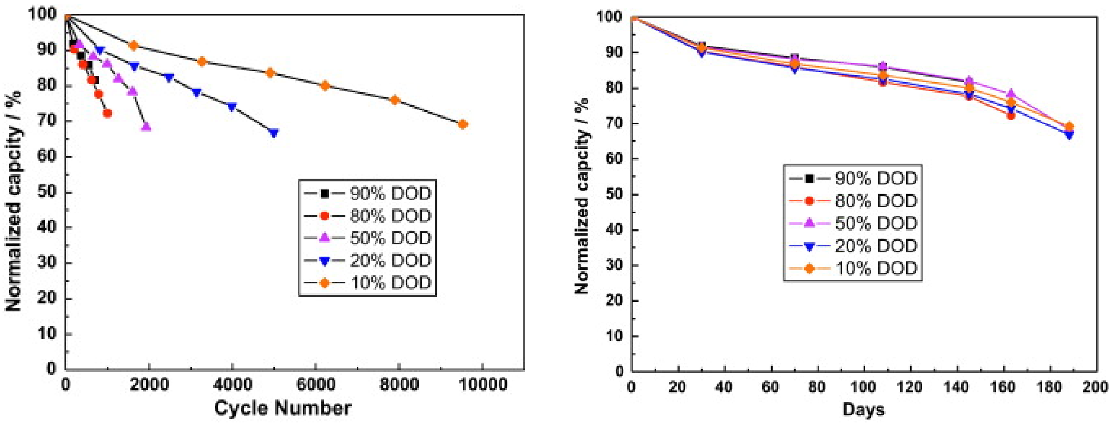

(a) (b)

Figure 2.5: (a) Capacity retention at 60°C and a discharge rate of C/2 plotted as function of cycle number, data shown for 90, 80, 50, 20 and 10% DOD. (b) Capacity retention at 60°C and a discharge rate of C/2 plotted as function of time (days), data shown for 90, 80, 50, 20, and 10% DOD. The images have been extracted from [18].

Given the negligible effect of the DOD, Eq.(2.3) becomes Eq.(2.4).

$$Q_{loss} = f(t, T, Rate) \tag{2.4}$$

By using the model introduced by *Bloom et al.* in [19] it is possible to connect the capacity fade with time and temperature with the battery life model in Eq.(2.5).

$$Q_{loss} = B \cdot exp\left(\frac{-E_a}{RT}\right) \cdot t^z \tag{2.5}$$

Instead of using *time* in Eq.(2.5) *Wang et al.* decide to link capacity fade to the Ah processed by the battery. In particular *Ah-throughput* is the charge processed by the battery during cycling operation. For every C-rate value, the charge processed by the battery is directly proportional to the time: using Ah-throughput instead of time it is possible to quantify the capacity fading behaviours for different charge/discharge rates.

Hence the battery life model previously introduced becomes Eq.(2.6). In Eq.(2.6), Q_{loss} is the percentage of capacity loss, B is named pre-exponential factor, E_a is the activation energy in Jmol^{-1}, R is the gas constant, T is the absolute temperature, and Ah is the charge processed by the battery.

$$Q_{loss} = B \cdot exp\left(\frac{-E_a}{RT}\right) \cdot (Ah)^z \tag{2.6}$$

Eq.(2.6) is rearranged as in Eq.(2.7) for analytical purpose.

$$ln(Q_{loss}) = ln(B) - \left(\frac{E_a}{RT}\right) + z \cdot ln(Ah) \tag{2.7}$$

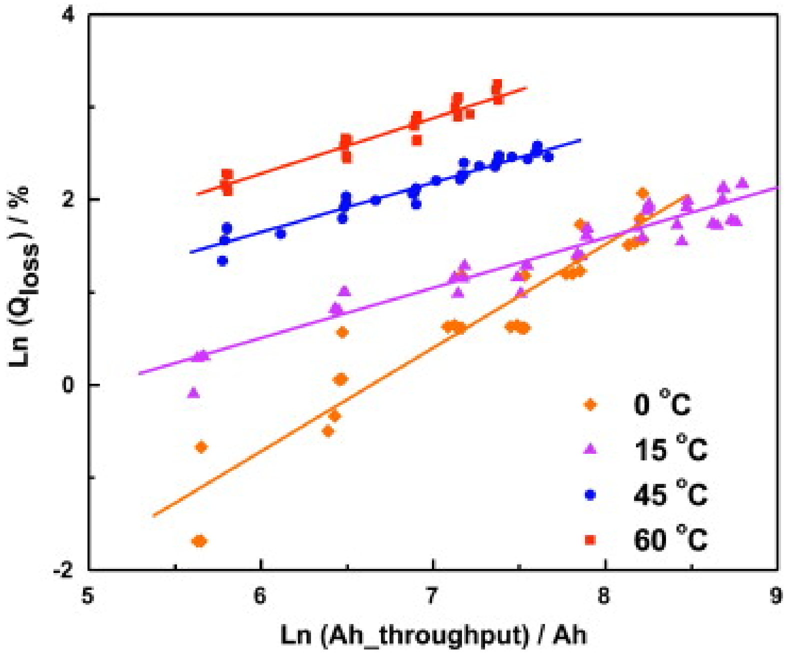

Figure 2.6: Image taken from [18]. Fit achieved when using equation to predict capacity loss as a function of temperature. Capacity loss is plotted as function of Ah throughput at 0, 15, 45, and 60 °C. *Linearity is obtained for each temperature level.*

In fig.2.6 the percentage of capacity loss is plotted as function of Ah-throughput on a log-log scale for different temperature levels. The continuous line represent the linear fit at each temperature. The lowest temperature value (-30°C) is not reported in fig.2.6 since the cell cycled at this temperature does not cycle long enough to have sufficient data. The slope of each line is the power law factor z. The fitted lines are almost parallel to each other meaning that the temperature effect is independent of the power law factor z. At 0°C the fitted line is steeper meaning that at such low temperature level ageing might proceed in different ways. *Wang et al.* conclude that at 0°C other ageing mechanism might happen hence they decide to exclude this temperature level.

2.4.1 Life model development for C/2 rate

A single step optimization has been implemented in [18] to determine the fitting parameters by rearranging Eq.(2.7). As represented in the figure fig.2.7 $ln(Q_{loss}) + E_a/RT$ is plotted versus $ln(Ah)$. The activation energy E_a in [18] is obtained from the intercept values of the best-fit non linear regression curves. By exploiting also the data for different temperature values (at C/2 discharge rate) *Wang et al.* find that the activation energy E_a is equal to 31,500 J mol^{-1}. The effect of temperature instead is described by an Arrhenius relation, which represents somehow the kinetics of a thermally induced chemical process.

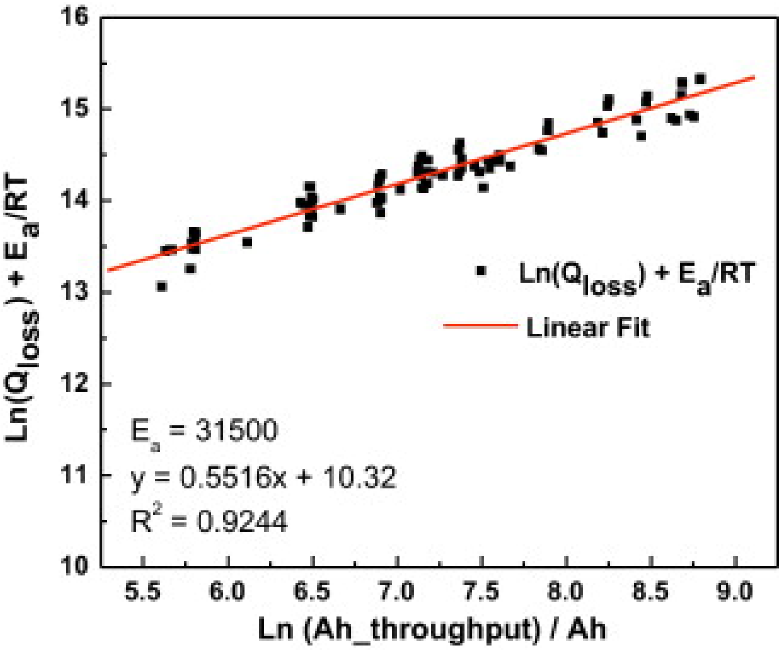

Figure 2.7: Eq.(2.7) to determine the fitting parameters for the life prediction model in which $ln(Q_{loss}) + E_a/RT$ is plotted as a function of ln(time). The activation energy was obtained from the best-fit values determined by non-linear regression, R^2. The slope and intercept of the linear fitting correspond to the power law factor, z, and the pre-exponential value, A, respectively.

The pre-exponential factor B is evaluated from the intercept of the linear fittings, reported in fig.2.7. The line slope, instead, represents the power law factor which turns out to be equal to 0.552 (for C/2 rate). Furthermore the power law factor is almost equal to 0.5 which corresponds to a square-root of time dependence. Previous papers [20, 21, 22], recognized that this square-root time relationship with capacity fade represents the irreversible capacity loss due to *SEI film growth* that depletes and consumes active lithium content within the cell. This process is regulated and controlled by a diffusion process. As a result, the capacity loss life model is expressed as in Eq.(2.8) and it can be used for qualitative simulation of capacity fade phenomenon under different operating conditions.

$$Q_{loss} = 30{,}300 \cdot exp\left(\frac{-31{,}500}{8.314T}\right) Ah^{0.552} \tag{2.8}$$

In fig.2.8 [18] cycle-life model results are compared with experimental data. By analyzing the plot in fig.2.8 it is possible to realize that a good agreement between model results and experimental data exists. Although the model marginally overestimates capacity loss at 45°C and underestimates capacity loss at 60°C the agreement between model and experiment is quite good.

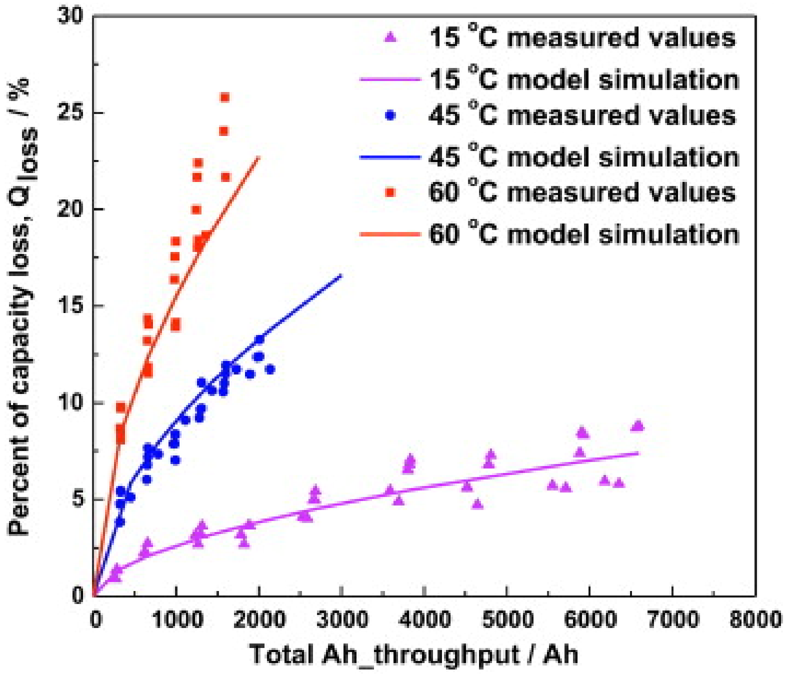

Figure 2.8: Simulation of cycle-life model prediction model (line) and experimental data (dots) at 15, 45, 60 and a C/2 discharge rate. *Source:* [18].

2.4.2 Life modeling for high C-rates

Wang et al. in [18] use Eq.(2.7) to fit the capacity fade profile at each discharge rate (2C, 6C, and 10C). They found that the experimental data follow the power law relation. For 2C discharge rate the activation energy and the power law factor are quite similar to the values of C/2, see Tab.2.1. Based on these considerations *Wang et al.* conclude that the aging-affecting factors remain similar for low and high discharge rates and for this reason they decide to use this power law to fit the capacity loss at 6C and 10C.

The optimal parameters, for each constant C-rate, of the pre-exponential factor, activation energy and z have been found by minimizing the total error which by the way is defined as in Eq.(2.9). More specifically the optimal values were found in [18] using Newton's iteration method solved in EXCEL with the SOLVER function. The calibration thus obtained for different *c-rate* values are summarized in Tab.2.1.

$$\epsilon_{opt} = \sum_{j=N} [Q_{loss,j}^{measured} - Q_{loss,j}^{model}]^2 \tag{2.9}$$

C-rates	Life model
C/2	$Q_{loss} = 30{,}300 \cdot exp(-31{,}500/RT) \cdot (Ah)^{0.552}$
2C	$Q_{loss} = 19{,}300 \cdot exp(-31{,}000/RT) \cdot (Ah)^{0.554}$
6C	$Q_{loss} = 12{,}000 \cdot exp(-29{,}500/RT) \cdot (Ah)^{0.56}$
10C	$Q_{loss} = 11{,}500 \cdot exp(-28{,}000/RT) \cdot (Ah)^{0.56}$

Table 2.1: Capacity fade equations at a given discharge rate. Model parameters have been obtained with the procedure explained before [18].

Furthermore the authors of [18] use the actual cell temperatures to fit the life model equation at high discharge rates. Cell heating during cycling operation is definitely more important at high discharge rate. At low environmental temperature the real cell temperature tends to rise more in discharging operation. Also DOD has an impact on the real cell temperature registered: several experimental tests evidence that the cells cycled at higher DODs heat up more than those tested at lower DODs.

In [18] the authors not only prove that battery life model for different discharge rate can be easily obtained also they try to formulate a ***generalized battery life model*** Eq.2.10 to explain capacity fade for very different operating conditions.

A closer examination on the activation energy reveals that the higher the discharge rate the lower the activation energy. A mathematical correlation to describe this trend can be derived. The power law factor, instead, varies from 0.552

(C/2) up to 0.56 for the highest C-rate value (10C): it assumed equal to 0.55.

$$Q_{loss} = B \cdot exp\Big[\frac{-31{,}700 + 370.3 \cdot C_{rate}}{RT}\Big](Ah)^{0.55} \tag{2.10}$$

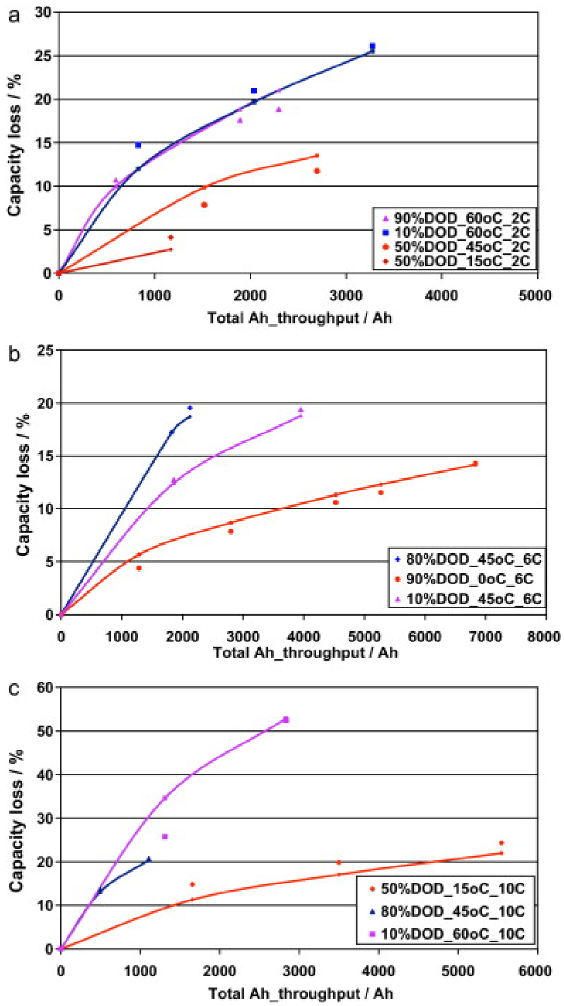

Figure 2.9: Model simulation results (lines) and experimental results (dots) at 2C (a), 6C (b) and 10C (c) discharge rates. Image taken from the paper of *Wang et al.* [18].

For the pre-exponential factor it seems that the higher the discharge rate the lower the pre-exponential factor although the identification of a mathematical relation to describe this trend is quite difficult. The authors of [18] to solve the problem use the *life model* reported in Eq.(2.10) to simultaneously fit the experimental data for all the c-rates. Even in this case *Wang et al.* try to get the values of the pre-exponential factor through a total error minimization, obtaining the results reported in Tab.2.2.

c-rate	C/2	2C	6C	10C
B values	31,630	21,681	12,934	15,512

Table 2.2: Generalized life model: pre-exponential factor values for different c-rate values [18].

In fig.2.9 simulation results obtained with the life model equation are compared with the measured capacity loss data for 2C, 6C and 10C rates. The model projections are fully and entirely consistent with the experimental data for all the C-rates.The power law factor is very close to 0.5 leading to a square-root of time dependence. Some studies [20, 21, 22] claim that the active lithium consumption rate at the anode (due to SEI film) has a square root time dependence. The authors of [18] applying and taking advantage of both destructive physical analysis and non-destructive analysis conclude saying that the major cause of battery performance fade is associated with *active lithium consumption*.

The Arrhenius relation effectively describe the kinetics of the chemical processes which are at the base of the side reactions leading to SEI formation. The major achievement of [18] is the creation (and validation) of such a simple and immediate model. The model created is in perfect sync with the experimental data. In the following this method will be used to find the best control strategy which contemporary minimizes fuel consumption and battery degradation.

2.5 Life model for a A123 Systems cell

2.5.1 Model parametrization

Wang et al. proposed a generalized capacity fade model [18] starting from cycling test results from an accelerated cycle life study on commercially available $LiFePO_4$ batteries. In the first part of the paper [18] a life model is developed to describe the time and temperature dependence of capacity fade at C/2 given that the effect of DOD for such low c-rate is negligible. In the second section this information is used to approximate the capacity fade behaviour at even higher c-rate (2C, 6C and 10C). In the last section the authors derive a generalized approach by a preliminary fitting of the life-model to the experimental data set.

In order to use this model in our application a detailed understanding of the model and its assumption is necessary. In our study the temperature of the cell is kept fixed at 25°C while *Wang et al.* test the battery in a wide temperature range. The test condition corresponding to 30 °C as highlighted before is not significant since the cell, tested in these conditions, does not cycle long enough to obtain sufficient data. The life-model obtained for C/2 rate seems to slightly overestimates capacity fade at 45°C and underestimates capacity fade at 60°C; the model results are instead perfectly aligned with the experimental data obtained at 15°C.

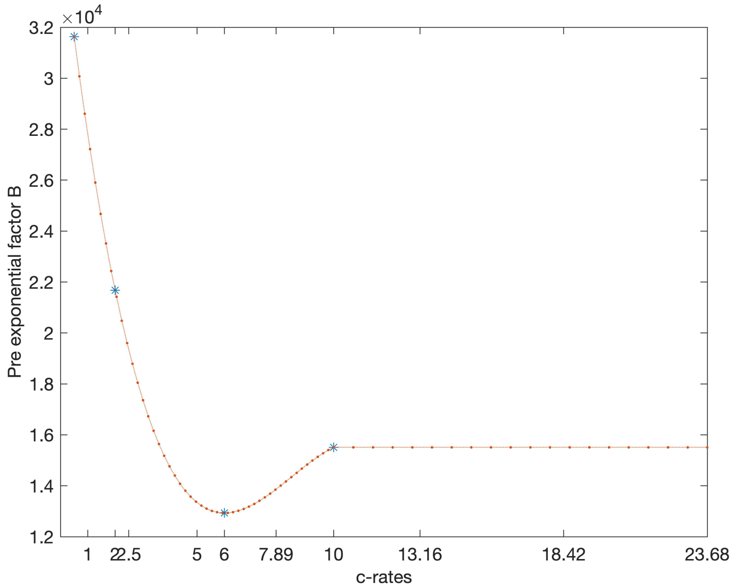

Figure 2.10: Linear interpolation of the experimental data sets. The blue points represent the values of the pre-exponential factors determined by *Wang et al.*in [18].Pre-exponential factor [-] as function of c-rate h^{-1}.

The depth of discharge of our cell is well below the DOD levels considered in [18]. The model has been validated considering more severe operating conditions in terms of depth of discharge.

The crucial point is to understand whether or not the life-model proposed by *Wang et al.* is reliable even dealing with higher c-rate values. The A123 cell under examination could reach very high discharge rate up to 23.68 h^{-1} while the maximum value of c-rate for which the life-model has been validated is 10C.

The first thing to do in order to use the unified model is to understand how the c-rate affects the pre-exponential factor. Actually in [18] the authors concluded that identifying a simple mathematical correlation between the pre-exponential factor and c-rate is not straightforward as for the activation energy. The first step of our analysis has been understanding how this parameter varies as function of charge/discharge rate. Starting from the experimental data for which the model [18] has been validated it is possible to look for a linear interpolation (fig.2.10) of the data set to establish a relation between B and *c-rate*. Given the impossibility to have access to significant data for c-rates higher than 10C a conservative approach has been used: pre-exponential factor is kept constant for c-rates higher than 10C.

Obviously the discharge rate of our application might be strongly different from those foreseen in [18] and to apply the life-model the pre-exponential factor has to be known for each *c-rate*. The information reported in fig.2.10 allow to know the value of the pre-exponential factor for each *c-rate* value.

2.5.2 Unified life model for different c-rates

In this section the unified aging model [18] is applied on a A123 ANR26650m1B cell that is tested under very different operating conditions in terms of *c-rates*. The objective of this paragraph is to test the life-model [18] to better understand whether or not it provides reasonable results.

Parameter	Description	Value
$Q_0(0)$	Nominal Capacity	7.3 Wh
V_{oc}	Open Circuit Voltage	3.34 V
T	Cell Temperature	25 °C
m	Cell Mass	0.07 kg

Table 2.3: $LiFePO_4$ cell data made by A123 Systems.

The *Ah-throughput* along the WLTC driving cycle have been evaluated by multiplying the number of cycles (treated as the independent variable) times the depth of discharge times the nominal cell capacity. This information is used in place of time given that at a fixed c-rate value the *Ah* is directly proportional to time.

Implementing the unified model Eq.2.10 it is possible to demonstrate that a clear correlation between the *c-rate* and capacity fade exists and the results are shown in fig.2.11. The higher the c-rate experienced by the cell the higher is the capacity loss foreseen by the model. By definition the end-of-life is reached when the battery capacity has dropped by 20%. For 2.5C and 5C the capacity loss seems to be less severe and this is due to the fact that the calendar-life effects were not isolated when the model was built: N cycles at low power expose the battery for a longer period of time to calendar-life effects.

This concept is going to be clarified in the following chapters of the thesis. Furthermore it is possible to notice that for the extreme values of c-rates the capacity fade appears to grow at an alarming rate.

It is worth to notice that in fig.2.11 the *c-rate* is kept constant along the entire driving cycle: in the real execution of the cycle the battery is not working with the same charge/discharge rate.

The goal of this paragraph is to check the validity of the model rather than the performance on the WLTC. This preliminary study is useful to check the validity of the model, which by the way will be implemented and used in the following for its simplicity and effectiveness.

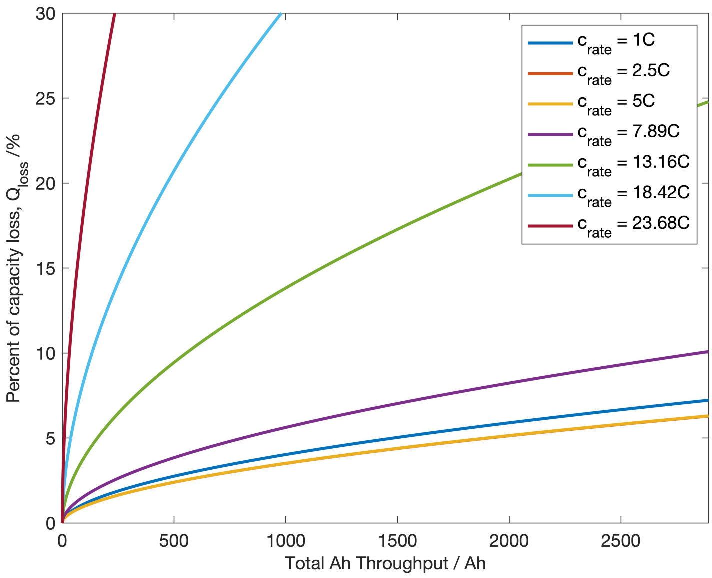

Figure 2.11: Percent of capacity loss as function of total *Ah throughput* for different c-rate values.

In fig.2.12 the same conditions of [18] are analyzed. The goal is to check the correctness and the accuracy of the model by comparing the results obtained with the results reported in [18]. In fig.2.12 the discharge rate (2C) is kept constant for all the curves. The blue curve is obtained with 50% depth of discharge and 15°C. The orange curve is obtained with 50% DOD and 45°C while the yellow curve represent 10% DOD and 60°C.

The first consideration to make is that the parametrization chosen for the pre-exponential factor of the model works quite well leading to have the same results obtained by *Wang et al.* in [18].

By looking at the three curve it is immediate to identify the more severe conditions for the battery: the cell cycled at 60°C (yellow curve) reaches the *end-of-life conditions* before than the other two cells. In fig.2.12 it is possible to realize the temperature effects on battery ageing: the DOD as explained in [18] has a minor effect on battery cycle life. The higher the temperature the steeper the curve: if the curve is steeper the end-of-life condition happen for a lower Ah processed by the same electrochemical system. End-of-life is assumed to happen when the original capacity drops of 20%.

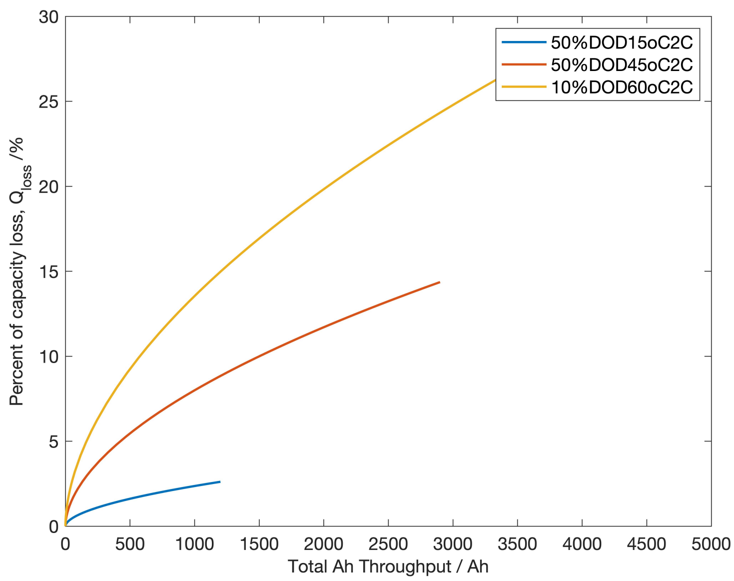

Figure 2.12: Percent of capacity loss versus total Ah throughput: check with [18].

Chapter 3

State-of-health estimation

The *State-of-Charge* of the battery is evaluated as in Eq.(3.1) where the $x_{1,0}$ is the initial state-of-charge while $Q_0(0)$ is the original energy capacity of the battery in Wh. Evidently the capacity $Q_0(t)$ decreases over time as the battery is used. In Eq.(3.2) the time derivative of the SoC is reported given that negative power values recharge the battery.

$$x_1(t) = x_{1,0} - \frac{1}{Q_0(0)} \cdot \int_0^t P_i(\tau) d\tau \tag{3.1}$$

$$\dot{x}_1(t) = -\frac{P_i(t)}{Q_0(0)} \tag{3.2}$$

Capacity fade models are usually grouped into three families [17]: 1) electrochemical models; 2) event-based models; and 3) energy-throughput-based models. Among these models the most suitable for on-board control strategies are the event-based and the Ah-throughput based models.

In the following the *energy-throughput model* will be adopted to study capacity-fade mechanism of the LIBs used in automotive application. As largely discussed in the previous chapter this model is based on the assumption that the battery can process a certain amount of charge under constant operating conditions.

Ebbensen et al.. in [23] define the *state-of-health* similarly to the *state-of-charge*, Eq.(3.3). $x_2(t)$ is the *State of Health* of the battery in time whereas the $x_{2,0}$ is the original SoH of the battery. N is the total number of cycles before end-of-life. The factor two in the denominator takes into acocunt that both positive and negative power values are integrated. When $x_2(t)$ equals zero, the end-of-life of the battery is reached.

$$x_2(t) = x_{2,0} - \frac{1}{2 \cdot N \cdot Q_0(0)} \cdot \int_0^t |P_i(\tau)| d\tau \tag{3.3}$$

It must be noted that N is not constant but it strongly depends on the operating conditions of the battery. *Wang et al.* in [18] concluded that for $LiFePO_4$ the main aging-inducing operating conditions are the *discharge rate and temperature*. The effect of the other conditions is quite marginal and it can be overlooked. *Ebbensen et al.*. in [23] reasonably fix the lumped cell temperature with a BMS. The only time-variant parameter is the discharge rate hence the primary goal is to identify a relation between c-rate and the number of cycles N.

Bloom et al. [19] found that, under constant operation, the capacity loss $\Delta Q_0(\%)$ with respect to the original value as in Eq.(2.10). Eq.(3.4) is another form of the Eq.(2.10). The activation energy dependency on the discharge rate can be expressed as $E_a(c) = (31{,}700 - 370.3 \cdot c)$ J/mol.

$$\Delta Q_0 = B(c) \cdot exp\Big(\frac{-E_a(c)}{R \cdot T}\Big) \cdot Ah(c)^z \tag{3.4}$$

The first thing to do to obtain a meaningfull expression for the number of cycles is to solve Eq.(3.4) for the *amp-hours*, see Eq.(3.5).

$$Ah(c) = \left[\frac{\Delta Q_0}{B(c) \cdot exp(\frac{-E_a(c)}{RT})}\right]^{\frac{1}{z}} \tag{3.5}$$

The number of cycle can be expressed as in (3.6).

$$N(c) = \frac{V_{oc} \cdot Ah(c)}{Q_0(0)} = \frac{Ah_{processed}}{Ah_{battery}} \tag{3.6}$$

Finally *Ebbensen et al.*. [23] using the linear transformation $c = P_i/Q_0$ arrive at the following *governing equation for the SoH*:

$$\dot{x}_2(t) = -\frac{|P_i(t)|}{2 \cdot N(|P_i(t)|) \cdot Q_0(0)} \tag{3.7}$$

In fig.3.1 the number of cycle to end-of-life is plotted as function of the discharge rate. Obviously the higher the c-rate the stronger the battery ageing will be. For intermediate c-rate values the battery seems to withstand an higher number of cycles and this can be explained *by the fact that* calendar-life *effects were not isolated when the model was build, i.e., the fact that* N *cycles take longer to process at low power than at high power, thereby exposing the battery to more calendar-life effects* [23]. The same "phenomenon" can be seen also in fig.3.2 where SoH trajectories in time are reported for different discharge rates. Even in this figure it is possible to notice that initially increasing the discharge rate the battery seems to behave better (lower aging). For 7.89C rate the number of cycle dramatically decrease (indicating that aging is more severe) in fig.3.1.

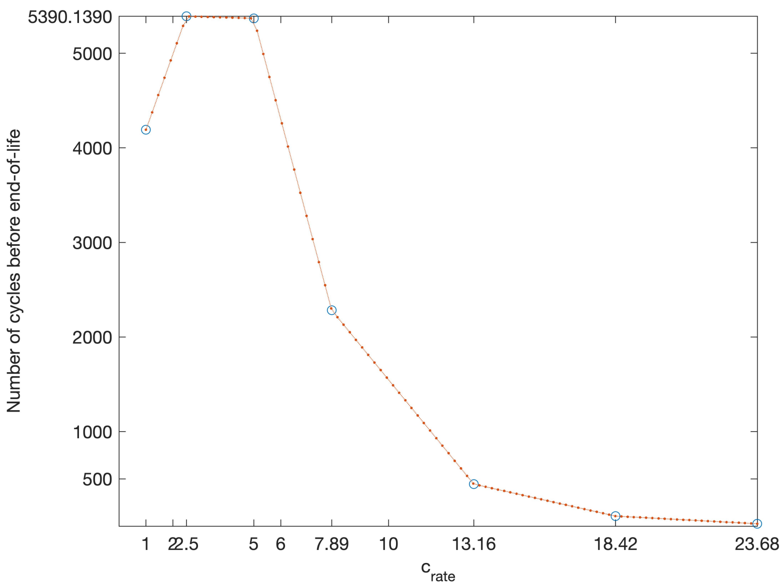

Figure 3.1: Influence of battery *c*-rate (or equivalently battery power) on number of cycles before end-of-life.

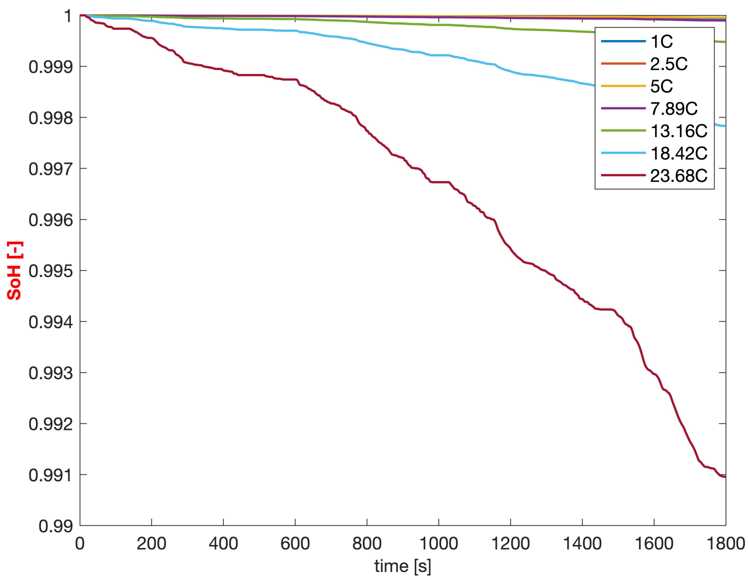

Figure 3.2: *State-of-health* trajectories in time for different *c*-rate values.

By applying the aforementioned procedure [23] it is possible to analyze battery ageing for a PHEV running in pure E-mode along the WLTC driving cycle. The PHEV under analysis is equipped with a 16 kWh battery but in this analysis the behaviour of the single cell is assumed representative of the entire battery pack. During the execution of the cycle the discharge rate experiences by the battery is not constant but it varies significantly according to the current profile. In the upper graph of fig.3.3 the WLTC speed profile is represented, in particular we are dealing with a Class 3 WLTP for high power vehicles with PWr > 34. Four sections can be identified: low, medium, high, and extra-high phase (according to the maximum speed reached in each of them). The current profile appears to be quite dynamic and it is likely to reach high value in the extra-high phase which is also the more demanding phase. The implemented model, as said before, is highly driven by the temperature and the discharge rate. Given that the temperature is kept fixed by a proper thermal management system the only critical variable is the *c*-rate. Aging is condensed in the last phase of the cycle, where the charge/discharge rates are likely to assume quite high value. Also, an harmonious connection between the current profile and the SoH exists.

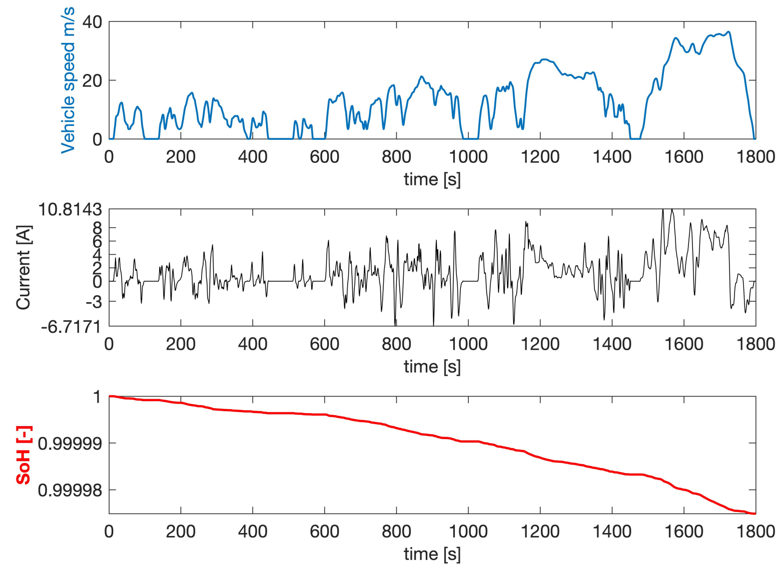

Figure 3.3: Speed profile of the WLTC (upper plot), cell current in time (middle plot) and *State-of-health* in time (lower plot). Results obtained with a battery pack of 16 kWh and using the procedure indicated in [23].

Anselma et al. in [24] use a slightly different approach. Although the ageing model used in [24] is still a throughput-based macroscale battery capacity fade model the results obtained might be significantly different. *Anselma et al.* evaluate the *state-of-health* as in Eq.(3.8) and the instantaneous SoH variation is defined as in Eq.(3.9). Eq.(3.8) is a rearrangement of Eq.(3.3), the main difference is how the number of cycles to end-of-life is intendend.

$$SoH(t_i) = SoH_0 - \int_0^t S\dot{o}H(c,T)dt \tag{3.8}$$

$$S\dot{o}H(c,T) = \frac{c}{3600 \cdot N(c,T)} \tag{3.9}$$

In the paper written by *Ebbensen et al.*., infact, the number of cycles is computed (as in Eq.(3.6)) considering only discharge cycles: the *amp-hours* processable by the battery is simply divided for the cell capacity. *Anselma et al.* instead, account for both charging and discharging phases in the battery roundtrip cycles, Eq.3.10. The number of "useful cycles" are now computed as the ratio between the processable charge and two times the cell capacity.

$$N(c,T) = \frac{Ah_{tp}(c,T)}{2 \cdot Ah_{batt}} \tag{3.10}$$

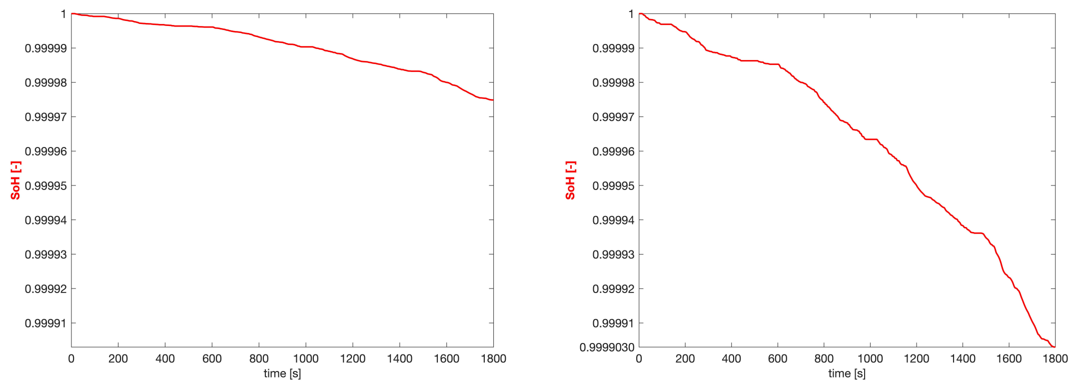

(a) **(b)**

Figure 3.4: *State-of-health* trajectories in time along the WLTC. Results obtained with a battery pack of 16 kWh. (a) *State of Health* trend obtained with the procedure indicated in [23]. (b) *State of Health* trend obtained with the procedure of *Anselma et al.* [24].

Ebbensen et al.. compute the number of discharge cycles the battery can potentially withstand before reaching end-of-life conditions. On the other hand

Anselma et al. compute the number of charge/discharge cycles for the battery to reach end-of-life condition. Obviously the approach [24] is more severe than that of *Ebbensen et al.* [23]. The increased severity is also demonstrated by the plot in fig.3.4: *State of Health* trend appears to be definitely more severe in fig.3.4b. In both there seems to be some inhomogeneities since in the *SoH* evaluation different quantities are compared. In the following paragraphs the models will be compared in detail.

If the vehicle repeats n times the WLTC driving cycle, with the same current profile, it is possible to understand how many repetitions are needed for the cell to reach EOL condition. The current profile in fig.3.3 leads to quite low discharge rate and in any case lower than five. This is certainly beneficial for the battery point of view. By integrating the speed profile in time is possible to know the distance covered during the WLTC: battery life can be expressed in terms of distance km.

	Ebbensen et al.	*Anselma et al.*	*Ebbensen revised*
SoH lost per cycle	2.5123e-05	9.6986e-05	4.8913e-05
WLTC repetitions	39804	10310	20444
Expiring distance	925,960 [km]	239,841 [km]	475,323 [km]

Table 3.1: SoH lost per cycle, WLTC repetitions and expiring distance for three different SoH approaches. Results obtained considering a battery pack of 16 kWh.

In Tab.3.1 there are summarized the main results of this preliminary analysis for three different approach. The approach named *Ebbensen revised* is basically grounded on the approach discussed before [23] but in the evaluation of the SoH it compares homogeneous quantities in terms of *real cycles* and *cycles to end of life*.

3.1 Results on different driving cycles

In this section a Plug-in Hybrid Electric Vehicle is tested on three different driving cycles: *Worldwide harmonized Light vehicles Test Cycles (WLTC), Highway Fuel Economy Driving Schedule (HWFET), and Urban Dynamometer Driving Schedule (UDDS).*

The PHEV considered is powered by a 5.16 kWh battery pack which in turn is constituted by a number of identical cell ANR26650m1B of A123 Systems arranged both in series and in parallel. As usual the behaviour of the single cell is assumed representative of the battery pack as a whole.

Fig.3.5 shows the speed profiles for the different cycles. The Worldwide harmonized Light vehicles Test Cycles (WLTC) are chassis dynamometer tests for the determination of emissions and fuel consumption for light-duty vehicles. The

WLTC replace the New European Driving Cycle (NEDC) based procedure for type approval testing of light-duty vehicles.

The Highway Fuel Economy Test (HWFET or HFET) cycle is a chassis dynamometer driving schedule developed by the US EPA for the determination of fuel economy of LD vehicles. The HWFET is used to determine the highway fuel economy rating, while the city rating is based on the FPT-75 test. The test is run twice, with a break of maximum 17 s between the runs. The first run is a vehicle preconditioning sequence, the second run is the actual test with emission measurement.

The US FPT-72 (Federal Test Procedure) cycle is also known as Urban Dynamometer Driving Schedule (UDDS). The cycle simulates a urban route of 7.5 mi (12.07 km) with very freqeunt stops. The maximum speed reached along this cycle is 56.7 mph (91.25 km/h).

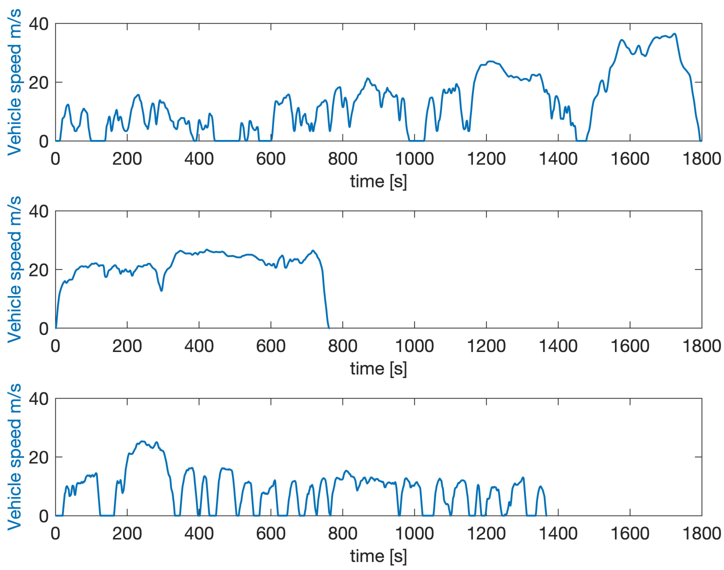

Figure 3.5: Speed profiles for different driving cycles: WLTC (upper plot), HWFET (middle plot), and UDDS (lower plot).

By having a closer look to the main characteristics of the driving cycles some conclusions can be drawn. The WLTC cycle is definitely the most severe driving cycle in terms of time duration, covered distance and maximum speed reached. In particular it can be subdivided in four different phases according to the maximum speed reached in each of them. The extra-high phase is the phase with the maximum speed and it would be representative of highway driving conditions. Nowadays, the NEDC cycle has become outdated, since it is not representative of the modern driving styles. To achieve a more realistic driving conditions, WLTC is 10 minutes longer than the NEDC (30 instead of 20 minutes), its velocity profile is more dynamic, consisting in quicker accelerations followed by short brakes.

The Highway Fuel Economy Driving Schedule (HWFET) represents highway driving conditions under 60 mph. In this case the time duration drops to 765 s, the distance covered is 16.45 km and the maximum speed is 96.4 km/h.

The EPA Urban Dynamometer Driving Schedule (UDDS) is commonly called the "LA4" or "the city test" and represents city driving conditions. It is used for light duty vehicle testing. It presents a time duration of 1370 s, a distance of 12.07 km and maximum speed of 91.2 km/h. This cycle by the way is characterized by frequent stops and this will have some repercussions in the following analysis.

The analytical procedure used for the *State of Health* estimation is basically the same of that described in the previous section of the thesis. It may be helpful to recap some of the most important steps:

1. Compute the charge/discharge rate as the ratio between the absolute value of the current and the cell rated capacity in amp-hours;

2. Compute the total amp-hours that the cell could potentially elaborate before its capacity drops of 20%;

3. Compute the total number of charge and discharge cycles before EOL is reached [24];

4. Evaluate how the *State of Health* varies in time considering different *c*-rate values for the different time instants;

For this analysis a battery pack of 5.16 kWh will be considered although the elementary unit is always an A123 Systems ANR26650m1B cell. The different battery pack capacity is reflected in a dirrent current profile. For a given power request the lower battery pack capacity the higher the current supplied.

3.1.1 WLTC driving cycle

If the PHEV runs through the WLTC driving cycle in purely electric mode then the results are summarized in fig.3.6. At the end of the mission the SoH turns out to be equal to 0.9993.

By analyzing together the SoH and the current (hence *c*-rate) profile in time it is interesting to notice that when the current takes higher value, the *c*-rate increases as well and the battery aging is more severe, leading to have some sharp descending stages in the SoH profile. Clearly in the extra-high phase the cell experiences the highest current values and as a consequence the aging is proceeding at a faster pace with respect to the initial phases of the cycle.

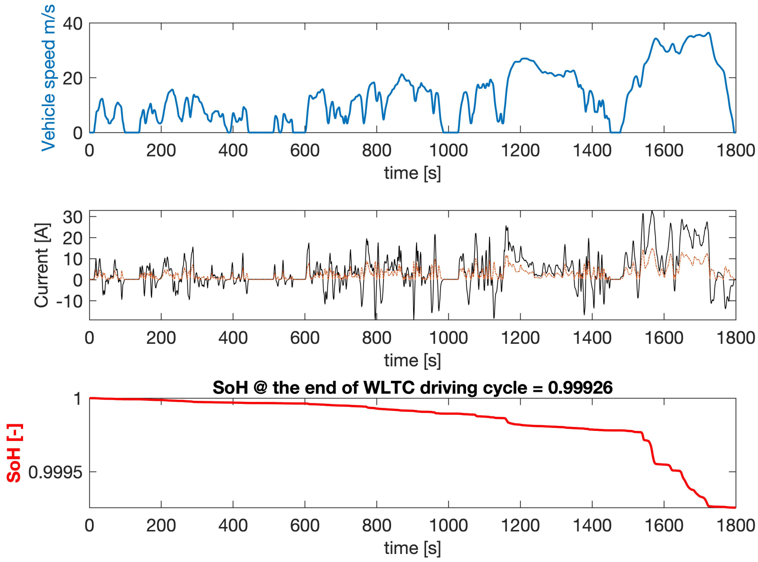

Figure 3.6: WLTC: speed profile in time (upper plot), current profile and C-rates in time (middle plot), and SoH variation in time (lower plot). Results obtained with a battery pack of 5.16 kWh. The approach used is that of *Anselma et al.* [24].

3.1.2 HWFET driving cycle

Similarly for the HWFET the same results are provided in terms of SoH and current profile in time fig.3.7. The SoH value at the end of the mission is in this case 0.99986.

Even in this case to have a clear overview on what is going on it is necessary to see together all the plots. The last plot, SoH vs time, clearly identifies which are the most severe phase during the cycle. The SoH quasi-linear trend is interrupted by some vertical stages which identify the most severe operating conditions for the battery aging. The more "linear" trend can be justified by looking at the *c*-rate profile which along the HWFET is definitely more "flat" than in the previous case.

The HWFET would be representative of constant-speed driving conditions which are typical on the highway. These driving conditions clearly explain why the current profile is more "stable" than that on the WLTC, which is more dynamic.

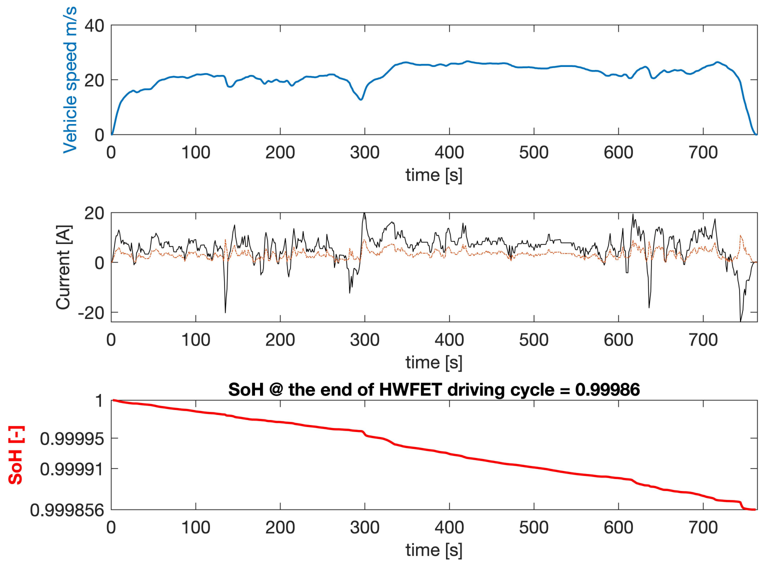

Figure 3.7: HWFET: speed profile in time (upper plot), current profile and C-rates in time (middle plot), and SoH variation in time (lower plot). Results obtained with a battery pack of 5.16 kWh. The approach used is that of *Anselma et al.* [24].

3.1.3 UDDS driving cycle

The last cycle considered is the UDDS. Also in this case the results are reported in terms of SoH and current profile in time fig.3.8. In this last case the SoH lost per cycle is around 0.000145. Even in this test case the SoH trajectory seems to decrease almost linearly except for some time instants.

After 200 s from the beginning of the mission the *State-of-Health* suddenly decreases and only after stabilizes again. This sudden SoH decrease happens in correspondence of the current peak, necessary to accelerate the vehicle up to 90 km/h. In the deceleration phase instead the current drops down to -10 A (regeneration-phase) and also in this case the SoH diminishes almost vertically, since the c-rate suddenly increases.

This aging model is highly sensitive to the operating conditions. The evidence of this can be sought in the SoH trend in time; whenever the cell experiences extreme current values, both positive and negative, the model immediately recognises those conditions as critical conditions for battery aging and in the *State-of-Health* is left the trace of these conditions.

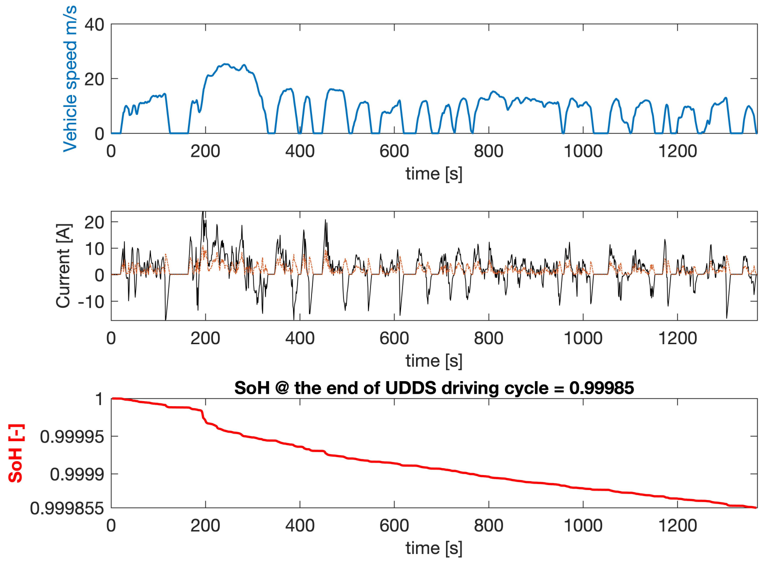

Figure 3.8: UDDS: speed profile in time (upper plot), current profile and C-rates in time (middle plot), and SoH variation in time (lower plot). Results obtained with a battery pack of 5.16 kWh. The approach used is that of *Anselma et al.* [24].

3.1.4 Conclusions

In this section there will be summarized some important conclusions of the analysis. In fig.3.9 it is plotted the SoH as function of time for the three different test cases.

The red curve represents the state-of-health variation along the WLTC driving cycle. As already mentioned the red curve reflects the severity of the operating conditions experienced during the WLTC. Surely the extra high phase, the most power demanding one, represents also the phase in which the battery aging is proceeding quite fast. The last part of the curve appears to be quite "vertical" meaning that battery aging is quite severe. On the contrary during the execution of the first parts of the driving cycle battery aging seems to proceed in a controlled manner. Above all the WLTC represent the most critical operation among the three test cases since it is not only the longest one but also the most severe one.

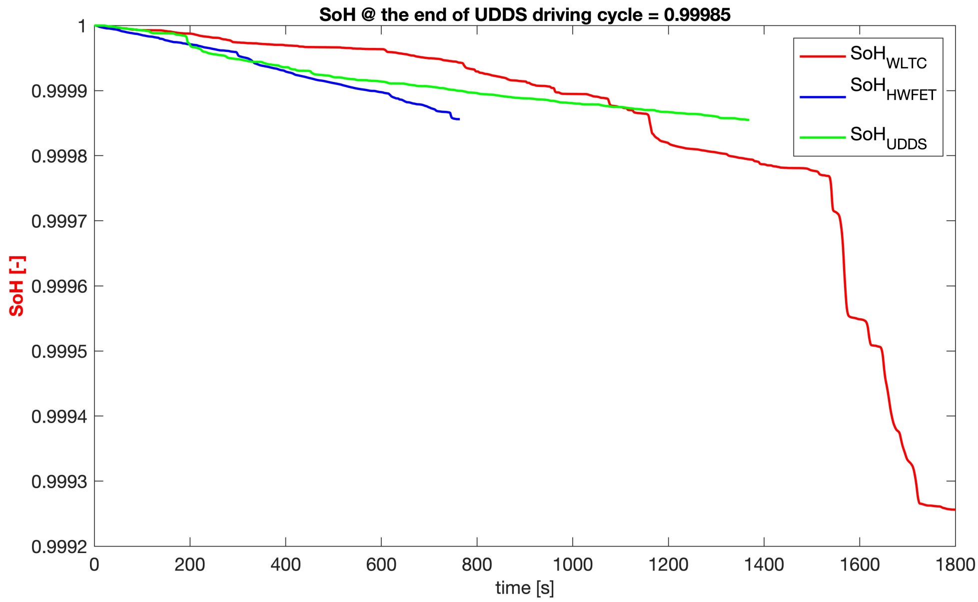

Figure 3.9: State of Health trajectories in time for different driving cycles: WLTC (red), HWFET (blue), and UDDS (green). Results obtained with a battery pack caapcity of 5.16 kWh. The SoH model used is that of *Anselma et al.* [24].

For the other two curves similar analysis can be done. The blue curve is referring to the HWFET which would be representative of highway driving conditions. Vehicle speeds during this cycle are quite high but their values remain almost constant along the entire mission. On average highway driving conditions are characterized by constant speed phases rather than frequent acceleration/deceleration which are more to the case of urban driving conditions. However this driving cycle represent the least severe in terms of operating conditions. This counterintuitive observation can be explained by looking how the *c*-rate varies in time. Although the average vehicle speed is quite high discharge rate appears to be quite stable, and quite low, on the HWFET except in some acceleration/deceleration manoeuvres during which the *c*-rate reaches high value (both in charge and in discharge) leading to more battery aging.

The green curve, instead, represents the UDDS driving cycle which is typical of urban driving conditions: speed profile appears to be much less stable. By looking at the speed profile it is very clear that now acceleration/deceleration phases are dominant in the driving scenario. Constant speed phases are almost non-existent. Basically what is possible to see is that at around 200 s the *c*-rate is rising all of a sudden up and as a consequence the *State-of-Health* decreases significantly. In the following time instants battery aging seems to be more "linear" and this is due to the fact that from now on the *c*-rate is more stable and oscillates around lower values.

These considerations allow to make some estimates about the mileage of the battery in the three test cases Tab.3.2. Definitely the most severe condition is represented by the WLTC cycle. If we apply the aging model of *Anselma et al.* imagining the vehicle to repeat many times the speed profile of the WLTC we end up having a mileage of about 31265.5 km in order to reach EOL. This result is in line with the results of the previous analysis in which we considered a battery pack of 16 kWh.

For the HWFET it is possible to find out about 114,327.5 km while for the UDDS mileage forecast turn out to be about 83,234.7 km. Again the results are perfectly those expected by considering only the *c*-rate profile in time. Generally speaking in the HWFET the current profile in time appears to be smoother than that in the UDDS. This characteristic can be ascribed to the driving scenario itself: HWFET would like to represent highway driving conditions during which the speed should remain as constant as possible. On the contrary the UDDS foresees very frequent acceleration/deceleration phases which translate in a more dynamic current profile. In conclusion, this result should not be surprising since the UDDS is characterized by more ramps thus exposing the battery to a more intensive operation

	SoH lost per cycle	Cycle repetitions	Expiring distance [km]
WLTC	0.00074373	1344	31,265.5
HWFET	0.00014387	6950	114,327.5
UDDS	0.000145	6896	83,234.72

Table 3.2: SoH lost per cycle, number of repetitions such that SoH=0 and striking distance. Results obtained with a battery pack of 5.16 kWh. Results obtained with the SoH model of *Anselma et al.* [24].

It is interesting to notice that by decreasing the battery pack capacity from 16 kWh to 5.16 kWh the battery life dramatically decreases Tab.3.3. For a given power demand, the lower the battery capacity the higher the discharge rate experienced by the battery (higher current). The energy-throughput ageing model is mainly driven by temperature and discharge rate: the higher the *c*-rate the stronger the battery aging and the shorter the life of the battery.

Pack capacity	5.16 kWh	16 kWh
WLTC	31,265 km	239,841 km

Table 3.3: Influence of battery pack capacity on the useful battery life along the WLTC. Results obtained with the SoH model of *Anselma et al.* [24].

3.2 Comparison between different SoH models

In this section the different approaches used to evaluate *state-of-health* variations in time will be analyzed and discussed. It has to be said that at the moment no standardized and consolidated procedures exist and the existing ones are however based on some assumptions. The final objective is to develop a reliable tool to predict battery aging under several operating conditions. The ageing model chosen is an *energy throughput based* one which basically connects the amp-hours processed by the battery with the capacity fade mechanisms, in a heuristic manner.

By exploiting the ageing model is possible to evaluate the total amount of charge that the battery can potentially process under specific operating conditions before end-of-life is reached, Eq.3.5.

This information is used to quantify the total number of cycles the battery could potentially withstand before its capacity drops of 20% respect to the original capacity.

$$N_{EOL,ch/disch} = \frac{Ah_{tp,max}(c,T)}{2 \cdot Ah_{batt}} \tag{3.11}$$

$$N_{EOL,disch} = \frac{Ah_{tp,max}(c,T)}{Ah_{batt}} \tag{3.12}$$

In Eq.3.11 the total number of cycles before EOL is intended as charging/discharging like while in Eq.3.12 the total number of cycles before EOL is discharging-only like. This distinction may seem trivial and unnecessary but actually it is quite important and the way N_{EOL} is computed deeply affects the final results, as shown before. Even for the *state-of-health* computation it is necessary to choose whether to consider real cycles made by the battery as charging-discharging like or not. Again this may seem trivial but actually it is not since the final results will be deeply modified.

$$SoH_t = SoH_{t-1} - \frac{1}{2 \cdot N_{EOL} \cdot Ah_{batt}} \int_{t-1}^{t} |I(t)| dt \tag{3.13}$$

$$SoH_t = SoH_{t-1} - \frac{1}{N_{EOL} \cdot Ah_{batt}} \int_{t-1}^{t} |I(t)| dt \tag{3.14}$$

By analyzing Eq.3.13 and Eq.3.14 it is simple to understand their meaning. The integral of the absolute value of the current in time returns the *amp-hours* that represents the charge effectively processed by the battery. In both of the equation the integrated value is divided by the battery nominal capacity Ah and this returns the number of *discharge-only* cycles made by the battery. The factor 2 in the denominator of Eq.3.13 is used to convert real cycles in charging-discharging quantity. The outcome of these operation is then compared with the the total number of cycles in order to quantify the damage brought by these specific operating conditions. It is important to underline the fact that the choices we make in this phase strongly and deeply affect the final results.

The literature proposes several approaches and each of them leads to have different results. *Ebbensen et al.* [23] consider Eq.3.12 and Eq.3.13 meaning that actually they are considering the total number of cycles before EOL as discharge-only cycles and the real number of cycles as charging-discharging cycles. *Anselma et al.* [24], instead, consider the total number of cycles before EOL as charging-discharging cycles, Eq.3.11. Another solution can be consider in both the cases charging-discharging cycles in order to compare homogeneous quantities in the computation of the *State-of-Health*.

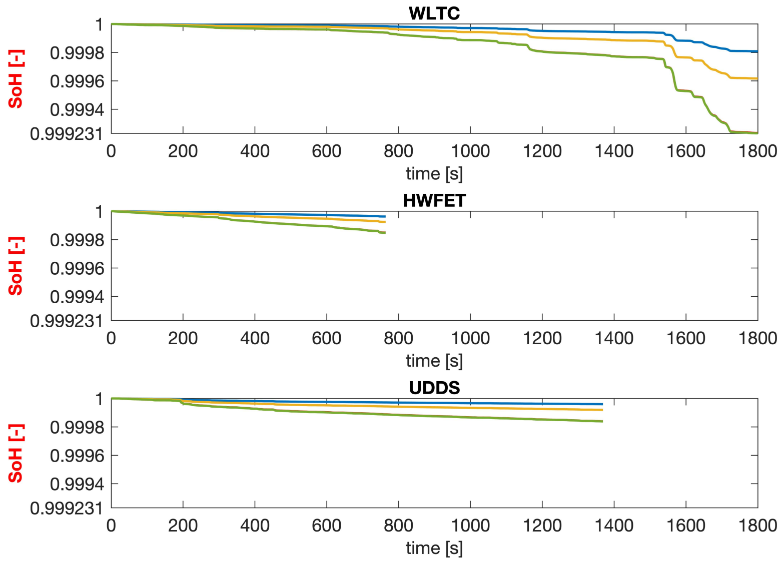

Figure 3.10: *SoH* trajectories in time for different driving cycles and with different models. In blue the model of *Ebbensen et al.* [23]. In green the model of *Anselma et al.* [24]. In yellow the model of *Ebbensen revised*, this model considers both N_{real} and N_{EOL} as charge-discharge like.

In fig.3.10 different *state-of-health* trajectories in time for different driving cycles (and obtained with different models) are presented.

The blue curve has been obtained with the model of *Ebbensen et al.* [23], in this case the *State-of-Health* has been evaluated considering the total number of cycles before EOL as discharging-only like cycles. It is the least severe model since it is actually comparing real charging-discharging cycles made by the battery with discharge-only N_{EOL}. This translates in lower SoH instantaneous variation.

The green curve has been obtained, instead, with the model presented in [24] in which the *State-of-Health* has been evaluated as in Eq.3.15. N_{EOL} is to be intended as charge-discharge like. The instantaneous SoH variation now is expressed as the ratio between *c*-rate and N_{EOL}. This ratio defines the state-of-health degradation in units of time. By integrating this ratio it is possible to know the capacity-fade percentage induced by those operating conditions.

$$SoH_t = SoH_{t-1} - \int_{t-1}^{t} \frac{c}{N_{EOL}(c,T)} dt \tag{3.15}$$

The yellow curve, representing an intermediate situation, has been obtained comparing homogeneous quantities. In this case infact both N_{EOL} and N_{real} are charging-discharging like quantities.

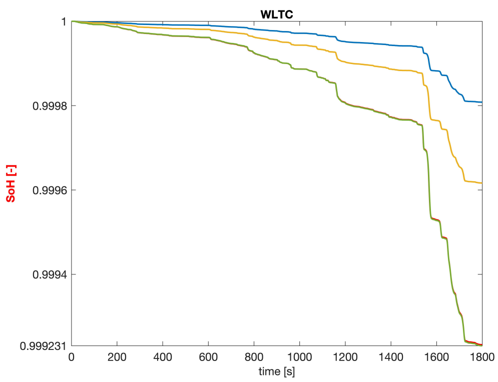

(a)

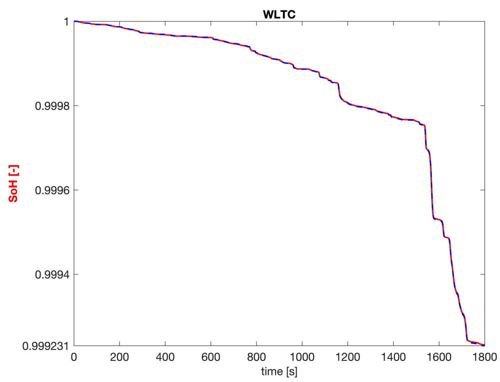

(b)

Figure 3.11: WLTC: (a) comparison between different *SoH* models: in blue the model of *Ebbensen et al.* [23], in green the model of *Anselma et al.* [24], in yellow the model of *Ebbensen revised*, this model considers both N_{real} and N_{EOL} as charge-discharge like. In (b) comparison between Mod1 (red) and *Anselma et al.* model (dashed blue). Battery pack capacity: 5.16 kWh.

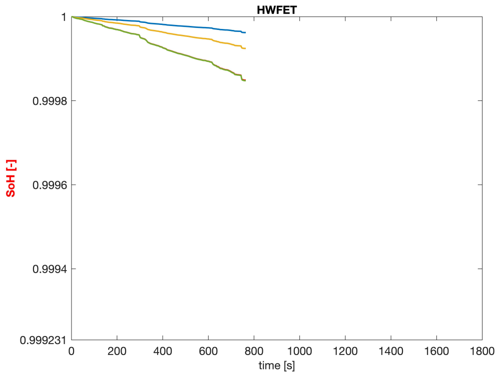

(a)

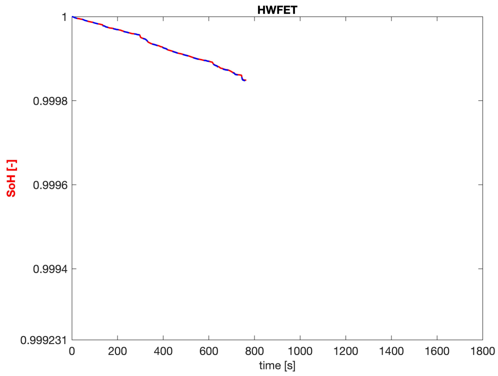

(b)

Figure 3.12: HWFET: (a) comparison between different *SoH* models: in blue the model of *Ebbensen et al.* [23], in green the model of *Anselma et al.* [24], in yellow the model of *Ebbensen revised*, this model considers both N_{real} and N_{EOL} as charge-discharge like. In (b) comparison between Mod1 (red) and *Anselma et al.* model (dashed blue). Battery pack capacity: 5.16 kWh.

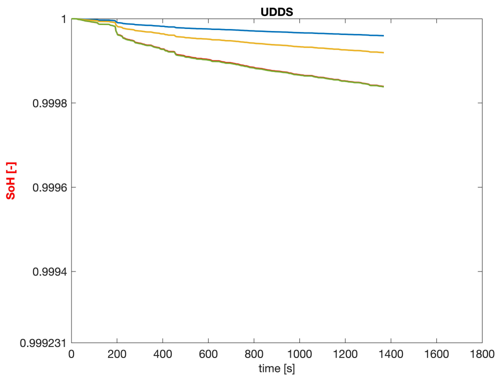

(a)

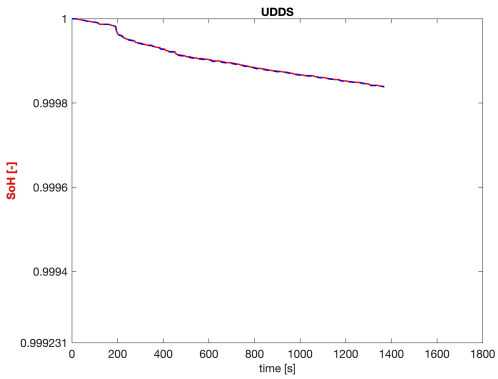

(b)

Figure 3.13: UDDS: (a) comparison between different *SoH* models: in blue the model of *Ebbensen et al.* [23], in green the model of *Anselma et al.* [24], in yellow the model of *Ebbensen revised*, this model considers both N_{real} and N_{EOL} as charge-discharge like. In (b) comparison between Mod1 (red) and *Anselma et al.* model (dashed blue). Battery pack capacity: 5.16 kWh.

In fig.3.11a, fig.3.12a, and fig.3.13a three different SoH models are used to evaluate the SoH degradation respectively along the WLTC, the HWFET and the UDDS. No matter what is the driving cycle considered the model of *Ebbensen et al.* [23] is the least severe one: SoH profile remains quite flat if compared with the other two models. On the other hand the model of *Anselma et al.* is the most severe one: it is quite sensitive to high c-rate values. The third model (*Ebbensen Revised*) represents an intermediate solution between the two previous mentioned models. Tab.3.4 compares in terms of analytical results the different models contemporary highlighting the meaning of N_{real} and N_{EOL} for each model. Furthermore in Tab.3.4 some consideration about battery pack capacity can be easily derived.

	LIB* life [km]	LIB** life [km]	N_{real}	N_{EOL}
Ebbensen [23]	121,336.6	925,960.4	ch/dis	dis
Anselma [24]	30,241.1	231,490.1	dis	ch/dis
Ebbensen revised	60,668.3	462,980.2	ch/dis	ch/dis

Table 3.4: Analytical comparison between different SoH models along the WLTC: LIB* is the *lithium ion battery* life considering a capacity of 5.16 kWh while LIB** refers to a battery capacity of 16 kWh.

Given that the meaning of the model [24] may not be immediate to understand another analysis has been conducted. By applying Eq.3.16 and Eq.3.17 (instead of using Eq.3.16 and Eq.3.18) the same results can be obtained. The combination of Eq.3.16 and Eq.3.17 is named MOD1. The graphical comparison between these two methods is showed, for different driving scenarios, in fig.3.11b, fig.3.12b, and fig.3.13b. The intrinsic meanings of the two models is perfectly the same: *SoH* profiles are identical. MOD1 is considering N_{EOL} as charging/discharging cycles while N_{real} is discharge-only cycles. Given that the results are very similar it seems that the model of *Anselma et al.* [24] is NOT considering real cycles made by the battery as charging/discharging cycles as indicated also in Tab.3.4.

$$N_{EOL}(c,T) = \frac{Ah_{tp,max}}{2 \cdot Ah_{batt}} \tag{3.16}$$

$$SoH_t = SoH_{t-1} - \frac{1}{N_{EOL} \cdot Ah_{batt}} \cdot \int_{t-1}^{t} |I(t)| dt \tag{3.17}$$

$$SoH_t = SoH_{t-1} - \int_{t-1}^{t} \frac{c}{N_{EOL}} dt \tag{3.18}$$

In conclusions it is possible to assess that the model of *Anselma et al.* is definitely more conservative than the other ones leading to have an higher SoH degradation in time which brings to a reasonable drivable distance before the battery has to be replaced.

3.3 Simulink model for SoH estimation

In this section a Simulink® macro-model is built and tested for the evaluation of the *State-of-Health* variations on different driving scenarios.

The model reported in fig.3.14 takes in input the current and temperature profile and returns in output the instantaneous SoH variation in time. The different blocks have different tasks and compute different quantities that will be send to the last block to compute the instantaneous SoH degradation.

In particular the model is actually computing SoH instantaneous degradation following the procedure seen before. It may be useful to recall the main steps: 1) compute the operating local *c*-rate; 2) compute the total *amp-hours* to reach EOL; 3) compute the total number of cycles to EOL; 4) evaluate how the SoH varies in time. This is a *forward model*: the information travels from the left side to the right side. The two red blocks on the right hand side of the model are two *to workspace* blocks which basically transfer information to the workspace. The *raw results* coming out from the model of fig.3.14 are manipulated in Matlab® to establish the SoH profile in time.

The Simulink® model has been designed in such a way that it is founded on a Matlab® script. Parameters setting happen in Matlab® and only after the simulation is launched. Different driving cycles require different *simulation times* which are set in the Matlab® environment.

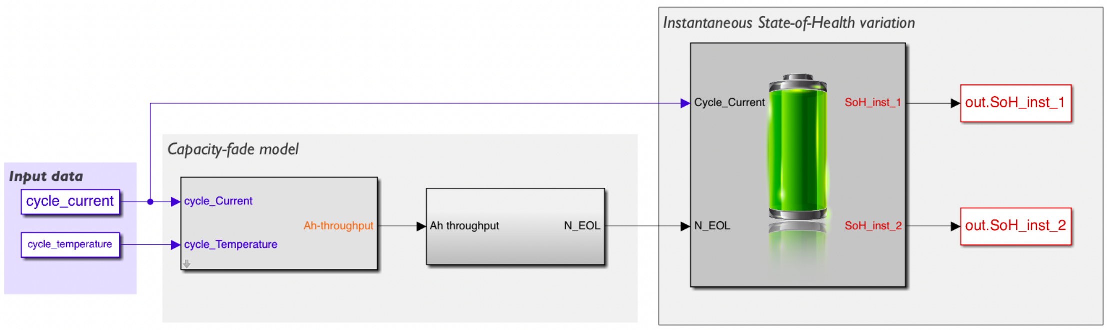

Figure 3.14: Simulink model to evaluate the SoH instantaneous variation on different driving cycles. The inputs for the model are the current and temperature profiles. The outputs are the instantaneous SoH variations (for two different SoH methods).

In order to provide a more clear understanding of the logic behind the model in the following a description of each block is presented. *Capacity-fade model* area is delegated to evaluate the maximum amount of charge (amp-hours) the battery may potentially process before its capacity drops of 20%. This information is then used in the other block in order to evaluate the total number of cycles before EOL. In this case N_{EOL} is intendend to be *charging-discharging* like but it can be easily tuned and modified. Finally the cycle current and the number of cycles (before *end-of-life*) are inputs for the last block which returns in output the instantaneous SoH variation.

3.3.1 Aging model block

In fig.3.15 it is reported the block containing the true and proper aging model which takes in input current and temperature signals and returns in output the *Ah-throughput* before EOL is reached for each time instant. Practically this block reads the current and temperature profile and by applying Eq.3.5 computes $Ah_{tp,max}$.

The fundamental idea is that of the *energy-throughput* based aging model. This kind of model links the charge processed by the battery to the performance fade. However this procedure is not straightforward: the *amp-hours* to EOL are measured under standard conditions while real batteries may be subject to quite different conditions.

Firstly this block computes the *c*-rate values as the ratio between the absolute current value of the current and the cell nominal capacity. This information is then used not only to compute the activation energy, which is function of the operating conditions, but also to evaluate the pre-exponential factor. The discharge rate is then linearly interpolated to obtain the value of B (the pre-exponential factor of the aging model).

The switch block, representing an if statement, passes through the first input port if the imposed conditions is true and passes through the second input port if not. If *c*-rate is higher than 10 the pre-exponential factor, as explained in the second chapter, is assumed to be constant.

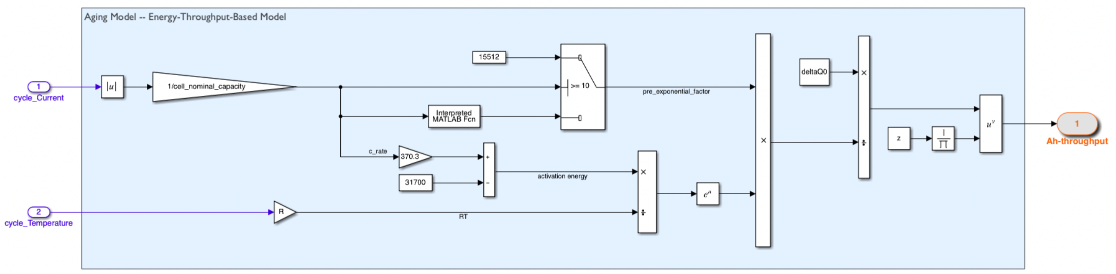

Figure 3.15: Aging model block to compute the maximum *amp-hours* processable by the battery before EOL.

3.3.2 Cycles block

In this section the cycles block will be analyzed, fig.3.16, which by the way is a very simple model. This block takes in input the *amp-hours* potentially processable (computed in the previous block) and divides it for two times the cell nominal capacity. The factor 2 in the denominator converts the number of discharge-only cycles in charging-discharging cycles.

As said before this block is computing the number of charge/discharge cycles for the battery to reach EOL: by changing the gain in the lower part of the block it is possible to obtain the number of discharge cycles.

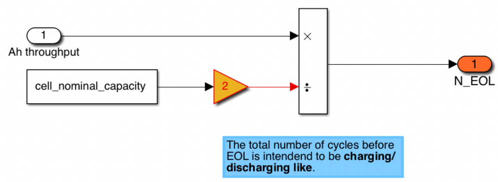

Figure 3.16: Total number of cycles block.

3.3.3 Instantaneous State-of-Health block

This block, the most important one, takes in input the current and the number of cycles before EOL and returns in output the instantaneous *state-of-health* degradation in time according to two different methods seen before.

The upper area in fig.3.17 considers the model of *Ebbensen revised*: in this model both N_{real} and N_{EOL} are intended to be charging-discharging like quantities. Unit delay block function is used to apply a unit delay to the current signal in order to compute the integral in time. The result of the integral is then divided by two times the cell nominal capacity in order to have the real cycles expressed in terms of charge/discharge cycles.

The lower area, instead, is referring to the model of *Anselma et al.* [24] in which the local SoH degradation is expressed as the ratio between the *c*-rate and the total number of charging/discharging cycles before EOL. This ratio is then integrated in time to know the damage applied to the battery under the specific operating conditions. As underlined in the previous paragraphs this model is actually comparing different quantities in the computation of the SoH but it is the most conservative one.

The two outputs of the considered block represent the instantaneous SoH variation in time and not the SoH profile in time. At this stage only the *State-of-Health* variation at each time instant is known. In Matlab® the SoH profile in time is reconstructed.

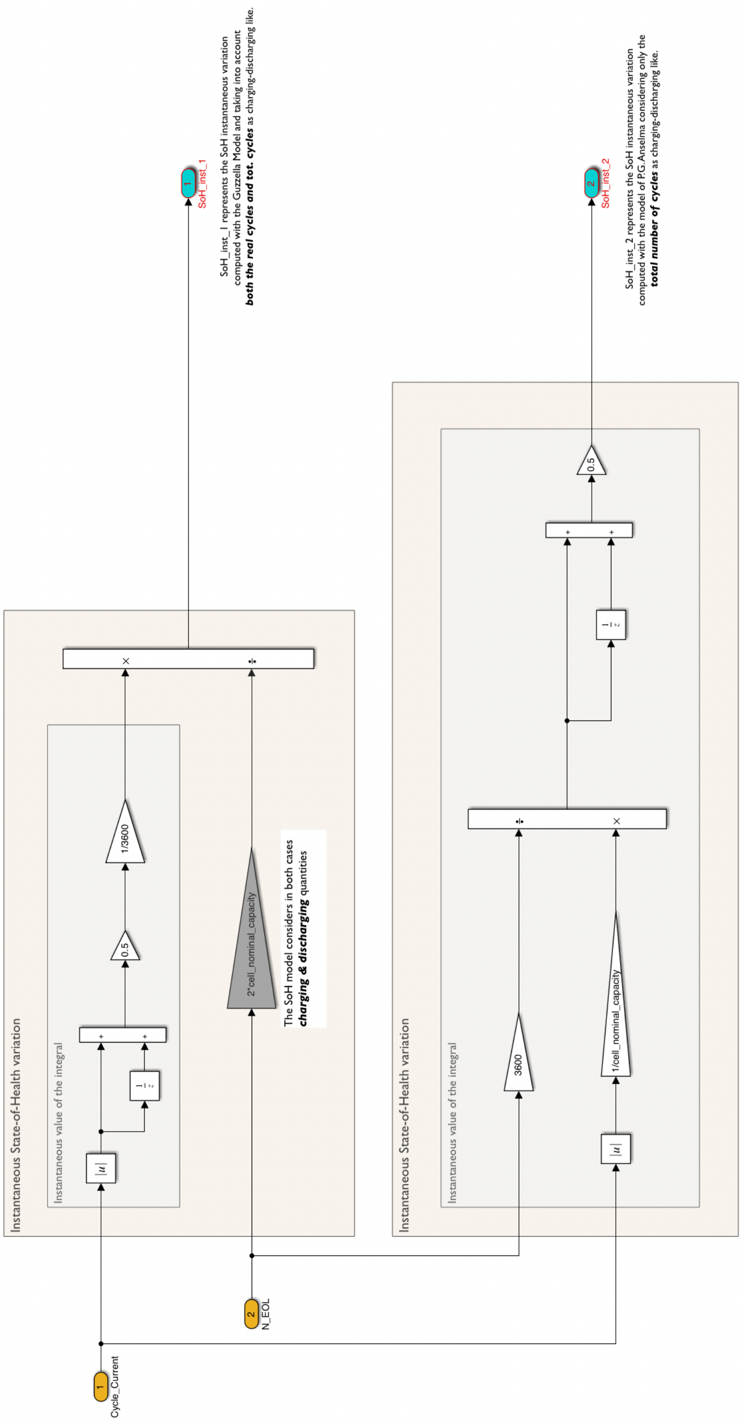

Figure 3.17: Instantaneous State of Health block.

3.4 Simulink model for battery life estimation

In this section it is presented the second model to estimate how many kilometres the vehicle can do before its battery reaches EOL conditions.

In fig.3.18 in particular the mileage model implemented in Simulink® is presented. The main objective of the model is to estimate the driveable distance before EOL. This model takes in input the two end values of the SoH trajectories, manipulated within the Matlab® script, and returns in output information about SoH lost per cycle (Eq.3.19), number of cycle repetitions (Eq.3.20) and total number of kilometres (Eq.3.21) such that SoH=0.

The central part of the model reads the speed profile in time - in [m/s] - and integrates it in time to get the distance covered during each cycle in [km].

$$SoH_{lost} = 1 - SoH(t_{end}) \tag{3.19}$$

$$n_{rep} = 1/SoH_{lost} \tag{3.20}$$

$$life_{km} = n_{rep} \cdot d_{WLTC} \tag{3.21}$$

The upper branching is referring to the first model while the lower one is referring to the second model in which the local SoH variation is expressed as the ratio between the c-rate and the total number of cycles.

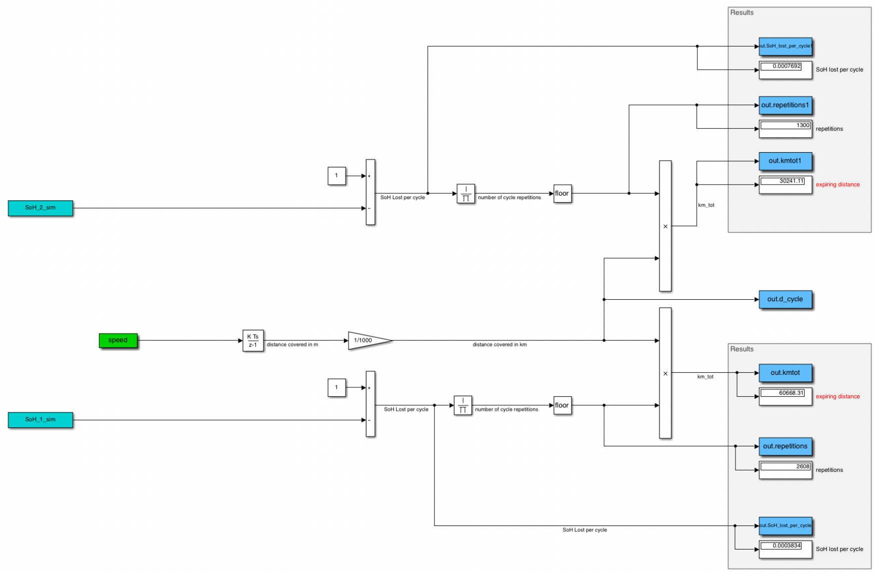

Figure 3.18: Battery life block.

3.5 Results on different driving cycles

In this section the results obtained by testing the Simulink® macro model are reported for different driving cycles. The results of the analysis have been obtained testing a PHEV powered by a 5.16 kWh lithium-ion battery pack.

The .slx model has been tested and validated for different cycles and it gives results in line with those expected. Furthermore the .slx model relies on a .m file and it can be easily used to simulate very different driving scenarios and/or different operating conditions even in terms of temperature.

Fig.3.19 shows the results obtained with the WLTC in terms of speed profile, current profile and SoH in time. For the *State-of-Health* the red curve refers to the *Ebbensen revised*: this model considers both N_{real} and N_{EOL} as charging/discharging cycle. The blue trajectories instead are obtained applying the model of *Anselma et al.* [24].

Similarly fig.3.20 and fig.3.21 show the results for the HWFET and UDDS respectively. As discussed above the WLTC for the battery is more demanding than the HWFET and the UDDS.

In this analysis also some real driving conditions are considered namely an uphill real driving scenario (altitude progressively increase in time) and a downhill real driving scenario. The main results for these two conditions are summarized in fig.3.22 and fig.3.23 respectively.

By analyzing the SoH trajectories for the two driving scenarios it is clear that the *uphill real driving conditions* appears to be definitely more severe than the other one: *State-of-Health* in fig.3.22 decreases faster than in fig.3.23. The final SoH for the uphill scenario is significantly lower than the final SoH value in case of downhill conditions. In fig.3.23 the current profile is smoother and as consequence the SoH trajectories are more flat. In fig.3.22 the battery is subjected to very severe aging due to very high current level experienced by the battery.

The battery has a capacity of 5.16 kWh and it is actually responsible for ensuring the longitudinal dynamic of the vehicle hence current profile is strictly related to the vehicle speed. In the acceleration phase the battery is called to work with very high discharge current levels whereas in the deceleration phases the battery is called to work with very high charge current levels.

In Tab.3.5 there are reported the numerical results in terms of expiring distance for the two real driving scenarios obtained with the two different methods. Even in this case it is worth to notice that the uphill scenario is definitely more severe from the battery health point of view than the downhill one during which vehicle inertia is exploited. Another important consideration is that the second method (*Anselma et al*) is actually more sensitive to high *c*-rate values hence the damage forecast turns to be higher than in the other method.

	Ebbensen Revised	*Anselma et al.*	
WLTC	60,668.31	30,241.11	[km]
HWFET	218,629.25	108,415.02	[km]
UDDS	149,158.57	74,291.52	[km]
Uphill	9,007.05	3,538.48	[km]
Downhill	69,735.57	26,664.06	[km]

Table 3.5: Different SoH models and resulting mileage.

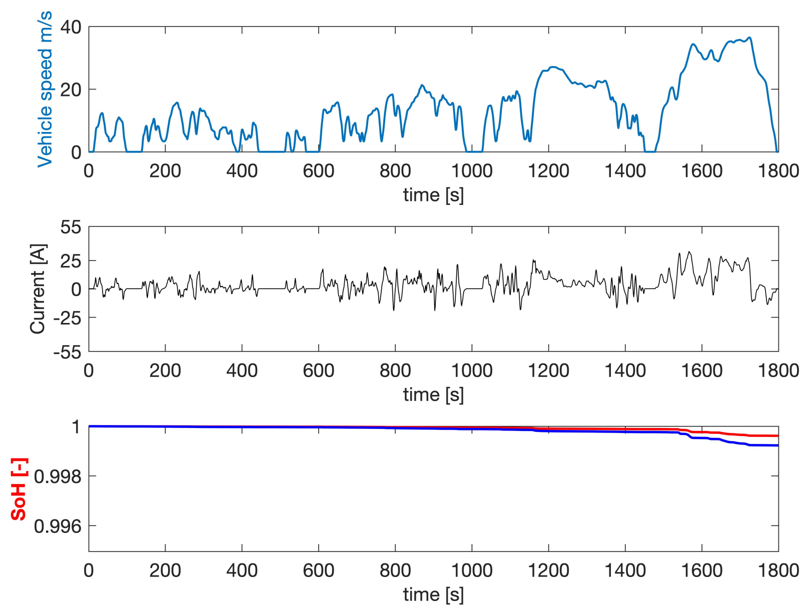

Figure 3.19: WLTC: speed profile in time (upper plot), current profile in time (middle plot), and SoH in time (lower plot).

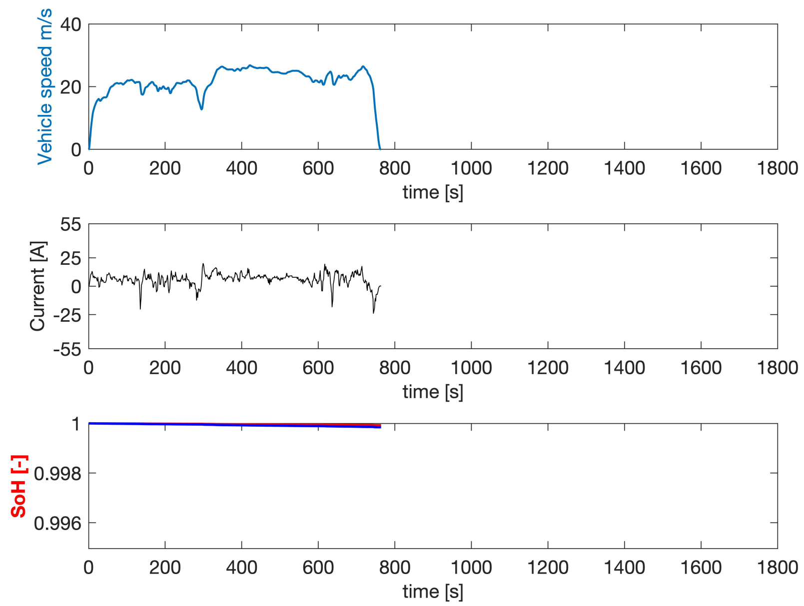

Figure 3.20: HWFET: speed profile in time (upper plot), current profile in time (middle plot), and SoH in time (lower plot).

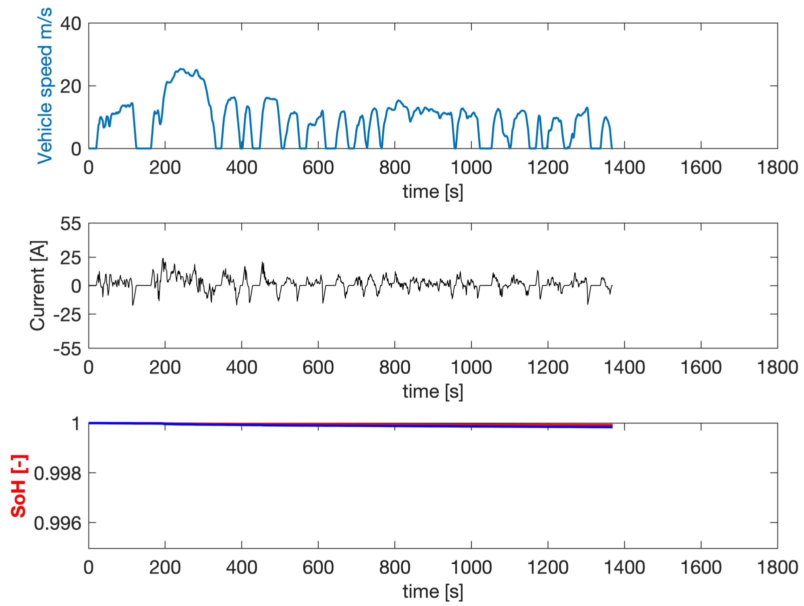

Figure 3.21: UDDS: speed profile in time (upper plot), current profile in time (middle plot), and SoH in time (lower plot).

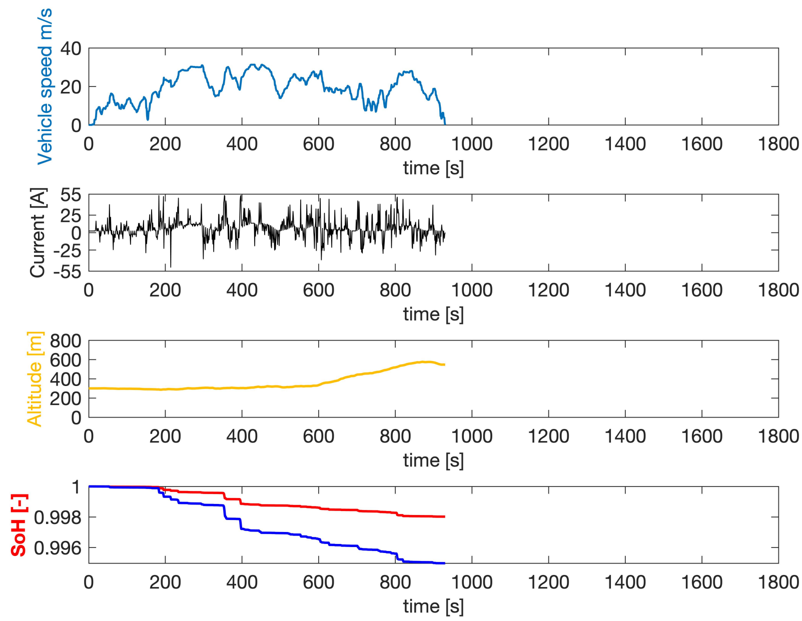

Figure 3.22: Uphill real driving conditions, starting from the upper part: speed profile in time, current versus time, altitude profile in time, and SoH in time.

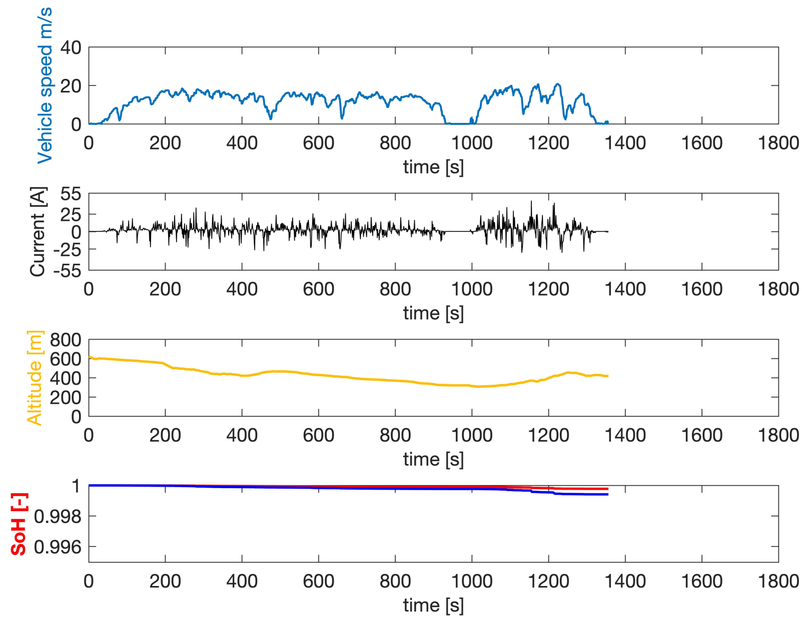

Figure 3.23: Downhill real driving conditions, starting from the upper part: speed profile in time, current versus time, altitude profile in time, and SoH in time.

Chapter 4

Equivalent Consumption Minimization Strategy

The origin of HEVs dates back to 1899, when Dr. Ferdinand Porsche, then a younger engineer at Jacob Lohner & Co, built the first hybrid electric vehicle, the Lohner-Porsche gasoline-electric vehicle. After the attempt of Dr. Porsche several other attempts were made in the early twentieth century in developing HEVs but the internal combustion engine technology improved significantly and hybrid technology disappears from the market.

Almost a century later hybrid vehicle technologies returned in vogue as a concrete alternative to fossil fuel powered engines: Toyota launched the Prius in 1998 and Honda proposed the Insight in 1999. The big step forward in the electronics and control systems fields make the new-gen HEVs more successfull than the first prototypes. A more sophisticated integration and on board cooperation between electronics and control systems helps in maximizing as much as possible the advantages of this technology.

The simple combination of two power sources within the vehicle is not enough in fighting effectively emissions and reducing fuel consumption. Energy management strategies are crucial to achieve the full potential of this technology, which can reduce fuel consumption and emissions thanks to the presence of a reversible energy storage device and one or more electric machines. Obviously the simultaneous presence of ad additional energy storage system creates new degrees of freedom and from this the necessity of finding an optimal strategy to split the power demand between the traditional engine and the battery. Different approaches can be used and very different results can be obtained. In the following a MO-ECMS will be used to solve the optimal control problem for a PHEV.

HEVs are equipped with two energy sources: a high capacity storage (a chemical fuel in liquid or gaseous form), and a lower capacity rechargeable energy storage system (REES) that can be used as an energy buffer. The REES can be hydraulic/pneumatic, electrochemical or mechanical. This bidirectional energy storage capability requires at least two energy converters. Generally speaking the acronym HEVs refers to those vehicle powered both by a traditional combustion engine, an electrochemical battery as REES and some electric machines (one or more).

The REES can be used for regenerative braking and also performs as energy buffer for the primary energy converter (ICE) which can immediately supply an amount of power different from the required load. It is precisely the flexibility in engine management which allows to place the engine operating points in high-efficiency and/or low pollution zone. With HEVs the internal combustion engine can be shut down when it is not needed (to reduce fuel consumption and tail pipe emissions) and also the fossil-fuel machine can be *downsized*. The power supply of the hybrid powertrain is now sum of the power supplied by the ICE and the power supplied by the electric motor hence it is possible to replace the original ICE with a smaller and less powerful engine. The downsized engine will operate at higher average efficiency (the smaller the engine the higher the operating load of the engine). In *Plug-in* Hybrid Electric Vehicles (PHEVs) the battery can be recharged from the electric grid and they offer an interesting range in pure electric mode. The Jeep Renagade 4xe PHEV analyzed in the following, for example, has a purely-electric range of about 50 km.

However HEVs include one or more electric machines properly coupled with the ICE and the wheel of the vehicle. According to the relative size of the electric machine(s) and the internal combustion engine the following classification [25] can be given:

1. Conventional ICE vehicles;
2. Micro hybrids (start/stop);
3. Mil hybrids (start/stop + kinetic energy recovery + engine assist);
4. Full hybrids (mild hybrids capability + electric launch);
5. Plug-in hybrids (full hybrid capability + electric range);
6. Full Electric vehicles (battery or fuel cell);

Conventional ICE vehicles and micro hybrids represent almost the same technology and the hybridization degree is quite low. The most interesting and promising technologies are those with an higher hybridization degree. In mild-hybrids vehicles, for example, the ICE is coupled with an electric machine and this allows the engine to be shut down whenever the car is stopping, coasting or braking even if pure

E-Drive is not allowed. Full hybrid vehicle, instead, run on just the engine, just the battery, or a combination of both. In full electric vehicles energy management strategies are crucial to obtain the highest possible benefit in terms of fuel consumption and emissions. PHEV battery can be recharged from the electric grid: they are very similar to full hybrids with the difference that the battery capacity can be easily restored from the external environment. Obviously by moving from (1) to (6) the hybridization degree is actually growing until *full electric vehicles* which are powered by a battery (recharged from the power grid) or a hydrogen fuel cell. Also HEV architectures can be classified as follows [25]:

- *series*: the engines drives a generator which produces electrical power which can be summed up with the electrical power coming from the battery and then the sum is transmitted to the electric motor;
- *parallel*: the power summation happens mechanically (rather than electrically): the engine and the electric machine are connected by means of a gear set, a chain or any other mechanical device. Their torques are summed and then transmitted to the wheels;
- *power split*: the engine and two electric machines are connected to a power split device (generally a planetary gear set), thus the power from the engine and the electric machines can be merged through both a mechanical and an electrical path, thus combining series and parallel operation;
- *series/parallel*: the engagement/disengagement of one or two clutches allows to change the powertrain configuration from series to parallel and vice versa, thus allowing the use of the configuration best suited to the current operating conditions;

The series architecture has the advantage of requiring only electrical connections between the power devices. Furthermore having the engine completely disconnnected from the wheels offers an incredible opportunity to choose freely engine operations (in terms of load and speed). By the way one of the weakest point of this solution is that two energy conversions are needed which introduce losses, even in cases when a direct mechanical connection of the engine to the wheels would actually be more efficient. There are conditions in which a series HEV consumes more fuel than a conventional vehicle, e.g. highway driving conditions. In parallel architecture, instead, the flexibility in choosing the engine conditions is completely erased since the engine speed is mechanically related to the vehicle speed. Finally *Power Split* and *series/parallel* are the most flexible, and give a higher degree of control of the operating conditions of the engine than the parallel architecture while applying the double energy conversion (typical of series) only to a fraction of the total power flow [25].

4.1 HEV powertrain modeling

The objective of the energy management strategies is to minimize fuel consumption while keeping the battery *state of charge* around a desired value. Usually HEVs operates in *charge sustaining* or in *charge depleting*.

In order to apply the control strategy a preliminary powertrain modeling is needed to create plant simulators. The model is in charge of reproducing the energy flows within the powertrain and the vehicle, in order to obtain an accurate estimation of fuel consumption and battery state of charge, based on the control inputs and the road load.

The net amount of energy produced at the wheels is smaller than the amount of energy introduced into the vehicle due to energy losses within the powertrain. When the energy is converted in another form then conversion losses happen. Similarly, when power flows through a connection device [25], friction losses and other kinds of inefficiencies diminish the power in output. Generally speaking in powertrain components energy losses are modeled and taken into account by using efficiency maps which basically are tables reporting the efficiency values as function of the operating conditions of the machine. These maps are built experimentally as a set of stationary points [25], i.e., input and output power values are measured only when the system has reached a steady-state configuration/condition. For this procedure the efficiency maps might result inaccurate during transient manoeuvres. Although this kind of model appears to be imprecise during transient operations it is very used since it is able to provide quickly good results.

Vehicle fuel consumption during a driving cycle can be estimated using a *backward* or a *forward* approach [25]. The first one, namely the *backward quasi static approach*, is based on the assumption that the cycle is followed exactly by the vehicle. The time axis is discretized hence divided in different time intervals and in each of these intervals an *average operating point approach* is used: speed, torque and acceleration remain constant. Somehow this means neglecting the internal powertrain dynamics [25] (e.g., engine dynamics, gear shifting).

The forward, dynamic approach is grounded on a first-principles description of each powertrain component, with dynamic equations describing the evolution of its state [25]. According to [25] *the degree of modeling detail depends on the timescale and the nature of the phenomena that the model should predict. In the simplest case, the same level of detail as the quasi-static approach can be applied, but the evolution of vehicle speeed is computed as the result of the dynamic simulation and not prescribed a priori.*

4.1.1 Equations of motion

If the vehicle is treated as a mass point then the following equations of motion can be written. In Eq.4.1 M_{veh} is the effective mass of the vehicle while v_{veh} is the longitudinal speed of the vehicle. Eq.4.1 is saying that the inertia force is equal to the tractive force generated by the powertrain minus the rolling resistance (due to tire deformations), the aerodynamic resistance and the force associated to the slope of the road.

$$M_{veh}\frac{dv_{veh}}{dt} = F_{inertia} = F_{trac} - F_{roll} - F_{aero} - F_{grade} \tag{4.1}$$

More specifically the aerodynamic resistance is expressed as in Eq.4.2 where ρ_{air} is the air density (1.25 kg/m^3 in normal conditions), A_f is the frontal area of the vehicle and C_d is the aerodynamic drag coefficient.

$$F_{aero} = \frac{1}{2}\rho_{air}A_f C_d v_{veh}^2 \tag{4.2}$$

$$F_{roll} = c_{roll}(v_{veh}, p_{tire}, \dots) \cdot M_{veh} \cdot g \cdot cos\delta \tag{4.3}$$

In Eq.4.3 F_{roll} is computed as the product between c_{roll}, the mass of the vehicle, the gravity acceleration and the cosine of δ which is the road slope angle. Obviously the product $M_{veh}gcos\delta$ is the vertical component of the vehicle weight. The coefficient c_{roll} actually depends on several parameters and those dependencies are not always simply identifiable and for this reason a simple function is defined in [25] (Eq.4.4).

$$c_{roll} = c_{r0} + c_{r1}v_{veh} \tag{4.4}$$

The grade force corresponds to the horizontal component of the weight and it is expressed as in Eq.4.5. This component opposes to vehicle motion if the vehicle is moving uphill and facilitates vehicle motion if the vehicle is moving downhill.

$$F_{grade} = M_{veh}gsin\delta \tag{4.5}$$

4.1.2 Forward and Backward modeling approaches

Eq.4.1 can be manipulated to calculate the tractive force the powertrain has to produce, given the acceleration as in the following equation.

$$F_{trac} = F_{pwt} - F_{brake} = F_{inertia} + F_{grade} + F_{roll} + F_{aero} \tag{4.6}$$

Eq.4.1 and Eq.4.6 correspond to the *forward* and *backward* modeling approaches: in Eq.4.1 the acceleration of the vehicle is computed as a consequence of the net tractive force generated by the powertrain and the speed is subsequently obtained integrating the acceleration profile in time: this is the *forward approach* and it describes the physical causality of the system [25]. Fig.4.1 represents schematically the information flow in a forward simulator [25].

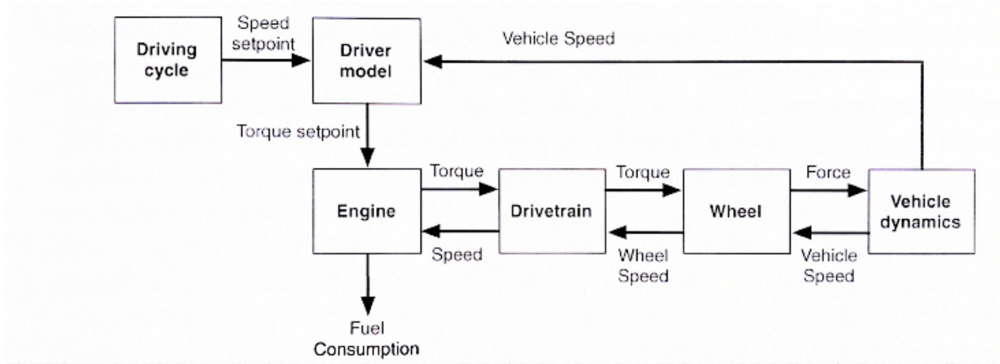

Figure 4.1: Information flow in a forward simulator [25].

On the contrary, in the backward simulator described by Eq.4.6 forces follow velocity and the powertrain generated force is calculated from the inertia force: F_{trac} is the force the powertrain must supply for the prescribed mission. Fig.4.2 represents schematically the information flow in a backward simulator [25]. The forward approach is the option preferred in many simulators (fig.4.1). For example, in [25] the authors write that in case of a hybrid vehicle the desired speed (driving cycle) is compared to the actual speed and every braking or throttle command is generated by a driver model (PID controller) in order to follow the requested speed profile. As showed also in fig.4.1 the driver model provides to the engine map the torque set-points according to the speed deviation registered by the controller.

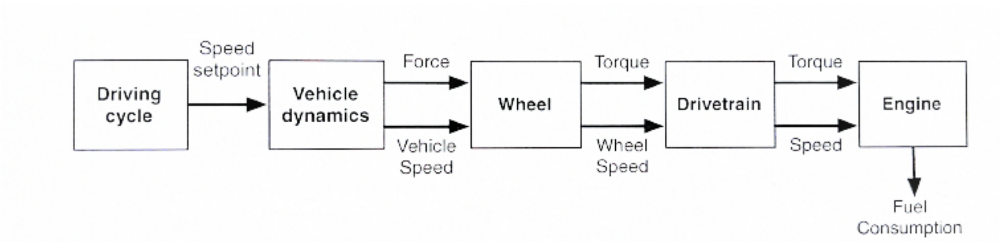

Figure 4.2: Information flow in a backward simulator [25].

In a backward controller no driver model is needed, see fig.4.2; in this case the speed profile of the driving cycle is the main input for the model and the outputs are the engine torque and fuel consumption. Technically speaking the simulator decides the net tractive force to be applied on the base of the velocity, payload, and grade. This is the starting point for the evaluation of the torque the powertrain has to supply and only after the torque/speed of the different powertrain components are calculated.

Both the forward and backward approaches have their relative advantages and disadvantages. Fuel economy simulations [25] are conducted on predetermined cycles hence the *backward approach* can be useful in this case to guarantee that the results are entirely and fully comparable at the end of the analysis. In contrast a *forward simulator* is not able to follow exactly the speed profile and at the end the results might not be comparable. On the other hand the *backward* simulator does not account for limitations of the powertrain actuators in computing the vehicle speed and this opens a problem of evaluating demanding cycles which may ask more power than the actual powertrain capability. A forward simulator does not have this kind of problem and it can be used also for acceleration tests since the speed is computed starting from the torque/force output.

4.2 Jeep® Renegade 4xe PHEV modeling

In this section, a HEV model with P4 configuration, which is based on Jeep® Renegade 4xe PHEV, is realized in Matlab® with a *backward quasi-static approach.*

The Jeep® Renegade 4xe Plug-In Hybrid, fig.4.3, consists of a P4 parallel hybrid electric drivetrain. The 1.3 l FireFly turbocharged gasoline engine is mounted on the front axle while the rear axle is powered by a 44 kW electric machine and a battery pack of 11.4 kWh. The driving cycle considered in the following is the *Worldwide harmonized Light vehicle Test Cycles* (WLTC or WLTP).

More specifically the new Jeep® Renegade PHEV can rely on a gasoline engine dedicated to the propulsion of the front wheels and an electric machine dedicated to the rear wheels. The electric motor is powered by a 11.4 kWh Li-ion battery that is recharged while driving (regenerative braking) or externally.

This architecture allows easily to realize *all-wheels drive configuration* and it is also known as *Through-The-Road* (TTR). The mechanical coupling between the two powertrains happens through the wheels, hence through-the-road. Fig.4.3 schematically shows how a P4 architecture is operatively realized: the traditional powertrain is completely disconnected from the electrical one.

The internal combustion engine on the front axle is connected to the front wheels by means of a gearbox and a differential whereas the electric machine is connected to the wheels through a differential and in the same time it is electrically connected to the energy source by means of a *bidirectional DC-DC converter.*

Fig.4.3 and fig.4.4 represent the same P4 architecture in two different ways. The schematic representation presented in fig.4.4 has been used as the starting point to model the hybrid powertrain.

(a)

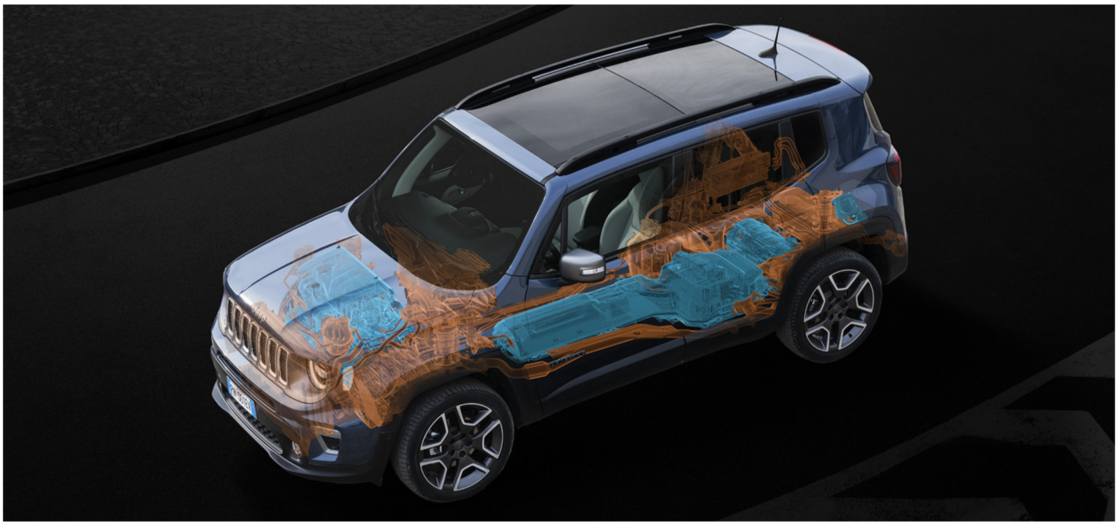

(b)

Figure 4.3: Source: *https://www.jeep-official.it/4xe-ibrido/renegade-4xe*. (a) Jeep® Renegade 4xe Plug-In Hybrid and (b) P4 architecture insights and real on-board implementation.

In the *backward quasi-static approach* force follows velocity: the main input is the speed profile. By knowing the velocity of the vehicle it is possible to compute the angular velocity of the wheels with Eq.4.7 where $v(t)$ is the vehicle velocity (according to the mission) and $r_{wh,dyn}$ is the dynamic rolling radius of the tyres. Front and rear wheels share the same angular (no slip between the two axles). However this information can be used in two different ways: on the front axle to compute the angular velocity of the internal combustion engine ω_{ICE} and on the rear axle to evaluate the angular velocity of the electric machine ω_{MG}. ω_{ICE} is computed with Eq.4.8 while ω_{MG} is the result of Eq.4.9.

$$\omega_{wheel}(t) = \frac{v(t)}{r_{wh,dyn}} \tag{4.7}$$

$$\omega_{ICE}(t) = \omega_{wheel}(t) \cdot \tau_{gear}(k_{gb}) \cdot \tau_{f,f} \tag{4.8}$$

$$\omega_{MG}(t) = \omega_{wheel}(t) \cdot \tau_{f,r} \tag{4.9}$$

In Eq.4.8, τ_{gear} represents the gearbox transmission ratio which in turn depends on the gear engaged ($\mathrm{k_{gb}}$) while $\tau_{f,f}$ is the transmission of the front final drive. Similarly in Eq.4.9 $\tau_{f,r}$ accounts for the transmission ratio of the final drive insisting on the rear axle. This methodology clarifies the *modus operandi* of the *backward quasi-static approach*: from the wheels backward to the engine passing through different elements looking out the driveline.

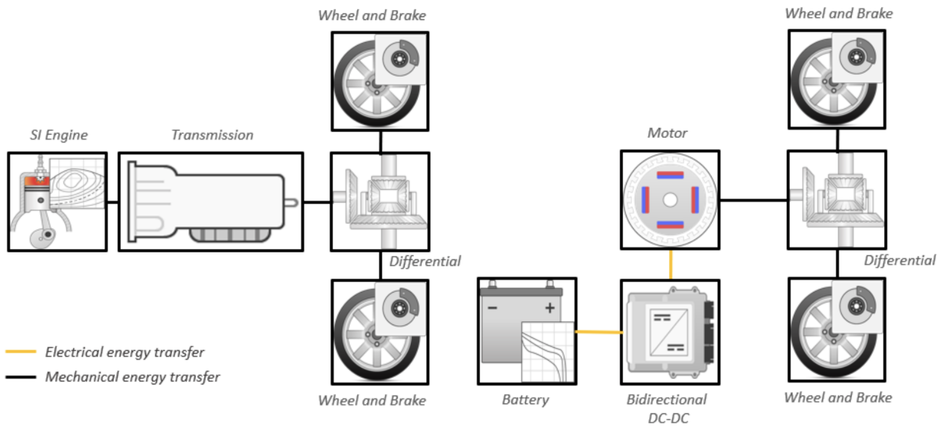

Figure 4.4: Schematic representation of a P4 Hybrid Electric Vehicle architectures. Source: *https://www.mathworks.com/help/autoblks/ug/explore-the-hybrid-electric-vehicle-p4-reference-application.html*

In Eq.4.6, $\mathrm{F_{trac}}$ is the tractive force generated by the powertrain and the brakes at the wheels. It is possible to define a resistive force as in the following equation. In the previous paragraphs each of the terms presented in Eq.4.10 has been explained in detail. However carmakers often provide the *coast down coefficients* to protect sensitive information. Eq.4.11 allows to evaluate the resistive force with the *coast down coefficients*: F_1, F_2, and F_3.

$$F_{res} = F_{grade} + F_{roll} + F_{aero} \tag{4.10}$$

$$F_{res} = F_0 + F_1 \cdot v + F_2 \cdot v^2 \tag{4.11}$$

The inertia force F_i is the product between the apparent mass and the acceleration, as highlighted in Eq.4.12. m_{app} actually considers not only the static masses (e.g., vehicle weight, battery weight) but also the inertia of the rotating masses. The apparent mass can be evaluated with Eq.4.13.

$$F_i = m_{app} \cdot a \tag{4.12}$$

$$m_{app} = m_{veh} + J_{wh}\frac{1}{r^2} + J_{ICE}\frac{\tau_{gear}^2 \tau_{f,f}^2}{r^2} + J_{MG}\frac{\tau_{f,r}^2}{r^2} \tag{4.13}$$

Finally it is possible to evaluate the torque request at the wheel that represents the starting point of the analysis, Eq.4.14.

$$T_{wh} = (F_{res} + F_i) \cdot r_{wh} \tag{4.14}$$

Given the powertrain configuration (P4) the torque (power) split between the on-board power sources has to be decided at the wheels level. The optimal power split in this study (between the ICE and the MG unit) is the power split that contemporary minimizes the fuel consumption and the battery ageing. Given that battery performances degrade in time and depending on the operating conditions it becomes important to establish a control strategy able to contemporary account for fuel consumption and battery aging. An unbridled exploitation of the battery will severely deplete battery performances and the system is no more able to perform according to the original design parameters. The variable u, introduced in Eq.4.15 represents the torque which has to be supplied by the MG unit. The variable u decides the power split between the front and rear axle. Technically speaking in Eq.4.15 the torque request at the wheels is dragged backward along the driveline to obtain T_{ICE} which represents the torque the ICE has to supply at the crankshaft level (before the gearbox). Eq.4.16 evaluates the torque demand seen by the electric machine upstream the final drive. $\eta_{m,front}$ and $\eta_{m,rear}$ are the mechanical efficiencies of the drivelines and definitely they are lower than one. In Eq.4.15 and Eq.4.16 mechanical efficiencies appear at the denominator and they increase the torque the ICE (and the MG) has to supply: to compensate the losses along the driveline the engine has to supply an higher torque to comply with the "real" request at the wheel.

$$T_{ICE} = \frac{(1-u) \cdot T_{wh}}{\tau gear \cdot \tau_{f,f} \cdot \eta_{m,front}} \tag{4.15}$$

$$T_{MG} = \frac{u \cdot T_{wh} + T_{brk}}{\tau_{f,r} \cdot \eta_{m,rear}} \tag{4.16}$$

The ICE model is a *map-based stationary engine* model, fig.4.5. There is no delay between the torque request and the torque response of the engine [26]: transients cannot be explained by the model. As explained in the previous sections these maps are obtained under steady state conditions: when the engine reaches the steady condition the fuel flow rate is measured. By knowing the angular velocity ω_{ICE} of the engine and the torque T_{ICE} it is possible to find the fuel mass flow $\dot{m}_f$ (Eq.4.17) handled by the engine (worked out by linear interpolation).

$$\dot{m}_f(t) = f(T_{ICE}(t), \omega_{ICE}(t)) \tag{4.17}$$

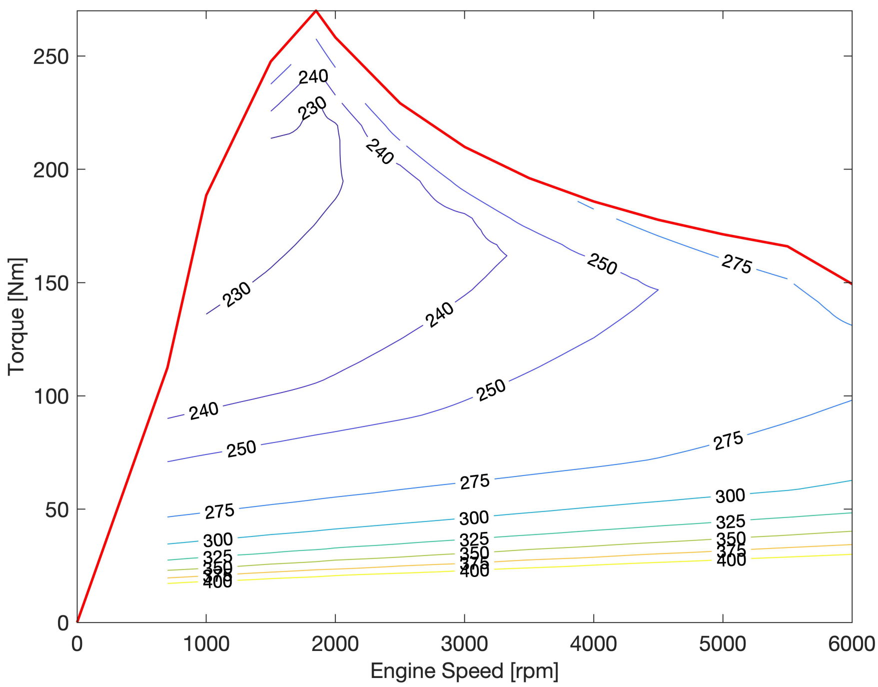

Figure 4.5: ICE map: *brake specific fuel consumption* as function of torque and engine speed. The full load curve is reported in red.

Similar to the ICE, the E-module is based on the characteristic diagram of E-Drive, which takes the role for the conversion between mechanical and electrical energy. Desired values of electrical power and or torque can be used as control input. The efficiency map provides a relation between the torque at the shaft and the electric power. Efficiency map can also include the power electronics between the main electric bus and the machine to provide directly the electric power exchanged with the battery [25]. It is possible to write down that the electrical power of the E-Drive is depending upon the torque (from the operation strategy) and the angular velocity of the machine. The efficiency map is shown in fig.4.6.

$$P_{MG}(t) = f(T_{MG}(t), \omega_{MG}(t)) \tag{4.18}$$

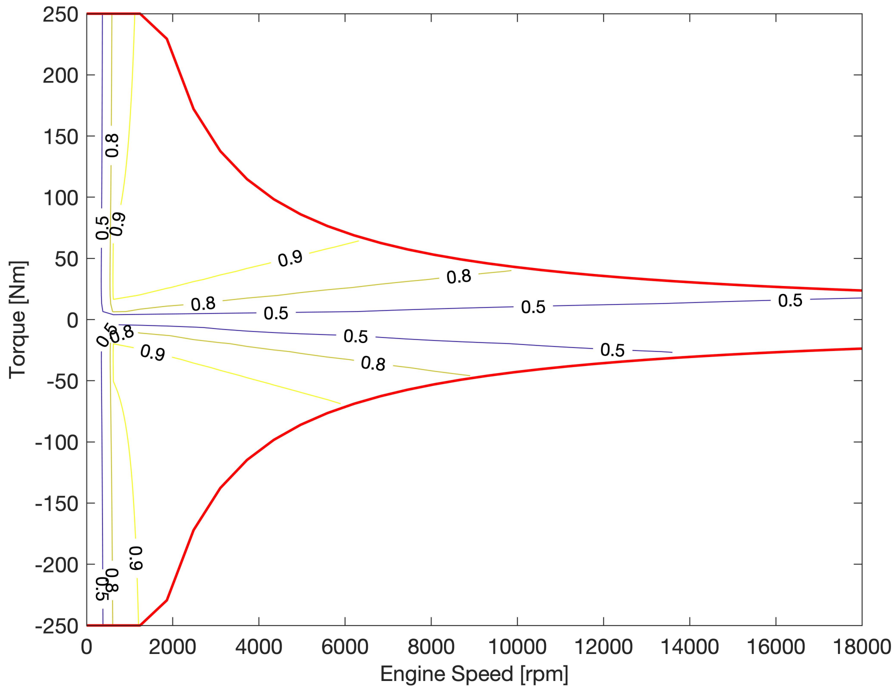

Figure 4.6: MG map: *MG efficiency* as function of torque and engine speed.

If the functioning mode is the motoring mode then the mechanical power supplied by the MG unit can be expressed as in Eq.4.19. The efficiency of the MG unit is function of η_{MG} and P_{elec}. Obviously if the MG acts as a motor it has to convert electric power into mechanical power but unfortunately the electric power is not fully converted, because of losses and inefficiencies.

$$P_{mech} = \omega_{MG} \cdot T_{MG} = \eta_{MG} \cdot P_{MG} \tag{4.19}$$

If the MG unit is used as generator then the relation between mechanical and electric power is quite different, Eq.4.20. In the *generating mode* the mechanical power at the shaft is used to produce electric power (to recharge the battery). Considering this transformation the efficiency operates in the other way around: the electric producible power is lower than the mechanical input power at the shaft.

$$P_{mech} = \omega_{MG} \cdot T_{MG} = \frac{1}{\eta_{MG}} \cdot P_{MG} \tag{4.20}$$

If the desired output is the electric power rather than the mechanical one, Eq.4.21 and Eq.4.22 are useful. Eq.4.21 is valid for the motoring mode while Eq.4.22 is true for the generating mode.

$$P_{MG} = \frac{1}{\eta_{MG}} \cdot P_{mech} = \frac{1}{\eta_{MG}} \cdot \omega_{MG} \cdot T_{MG} \tag{4.21}$$

$$P_{MG} = \eta_{MG} \cdot P_{mech} = \eta_{MG} \cdot \omega_{MG} \cdot T_{MG} \tag{4.22}$$

The subsystem auxiliary includes a 12 V electric system, in which a constant power demand P_{aux} and a constant efficiency for DC/DC converter $\eta DC/DC$ are assumed, [26]. The total electrical power demand in the battery P_{batt} comprises the total electrical power of the E-Drive and the electrical power demand coming from the auxiliary systems, Eq.4.23.

$$P_{batt} = P_{MG}(t) + \frac{P_{aux}}{\eta_{MG}} \tag{4.23}$$

The battery is simplified as an equivalent circuit model, as in [26], where V_{oc} is the open circuit voltage and R_i is the equivalent internal resistance and both of them depend on the *state-of-charge* (Eq.3.1). According to Eq.4.24 and Eq.4.25, $\mathrm{I_{batt}}$ and $\dot{S}oC$ can be worked out.

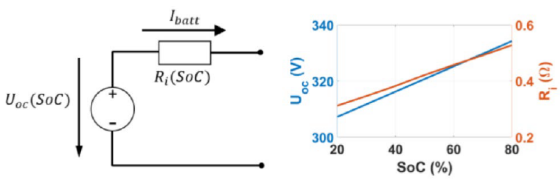

Figure 4.7: Equivalent circuit model of the battery [26]: U_{oc} is the open circuit voltage while $\mathrm{R_i}$ is the equivalent internal resistance.

$$I_{batt}(t) = \frac{V_{oc}(SoC(t)) - \sqrt{V_{oc}(Soc(t))^2 - 4 \cdot R_i(SoC(t)) \cdot P_{batt}(t)}}{2 \cdot R_i(SoC(t))} \tag{4.24}$$

$$\dot{S}oC(t) = -\frac{I_{batt}}{C_{nom}} \tag{4.25}$$

In the evaluation of the battery current I_{batt} charging and discharging operations must be distinguished since the internal resistance of the battery is deeply affected by the *functioning mode*. The internal power of the battery is given by

$$P_i(t) = V_{oc} \cdot I_b(t) \tag{4.26}$$

The battery model has been parametrized considering a $LiFePO_4$ battery cell made by A123 Systems (ANR26650M1). The maximum power of the electric machine of 44 kW effectively limits the maximum charge and discharge current of the battery to 132.5 A. The battery pack is composed by 120 elementary cells connected in series to form a module. Twelve such modules are connected in parallel to form a battery pack. At this point it is possible to compute the charge/discharge rate as the ratio between the battery current and the nominal battery capacity. With the *c*-rate the pre-exponential factor can be found and the $Ah_{throughput}$ is evaluated at each time instant. By knowing the amount of charge the battery might potentially cope with the number of cycles EOL can be evaluated.

In fig.4.8 the information flow in the simulation model is presented. The starting point of the analysis is the cycle information: namely the speed profile foreseen by the mission. The modeling approach is a *backward quasi-static approach*. Vehicle speed is used to compute the torque request at the wheel in the *Vehicle Dynamics module*. The *Vehicle Dynamics* module is responsible for establishing the angular velocity and the torque demand at the wheel. The torque requested at the wheel T_{wheel} is the input for the *Operation Strategy module* which is in charge of the torque splitting between the front and rear axle. The *Operation Strategy module* chooses how to split the torque between the two axles. The *transmission sub-module*, taking into consideration the torque-split, evaluates the internal combustion engine torque T_{ICE} and the motor generator unit torque T_{MG}. The *transmission sub-module* is also responsible for the kinematics of the powertrain. When T_{wheel} is negative T_{brk} is activated and used to recharge the battery pack: under these conditions the MG unit is functioning as generator. Knowing the angular speed and the torque of the ICE it is possible to know the fuel flow rate, hence the fuel consumption along the mission. Similarly, knowing the angular speed and the torque of the MG it is possible to evaluate the electrical power of the MG (passing through the efficiency). The power demand at the battery is the sum of the E-Drive power and the auxiliary systems power. Finally battery operating conditions can be described in terms of current (and discharge-rate) and the *ageing model* can be applied. Battery operating conditions are used for both the SoC evaluation and battery performances fade assessment.

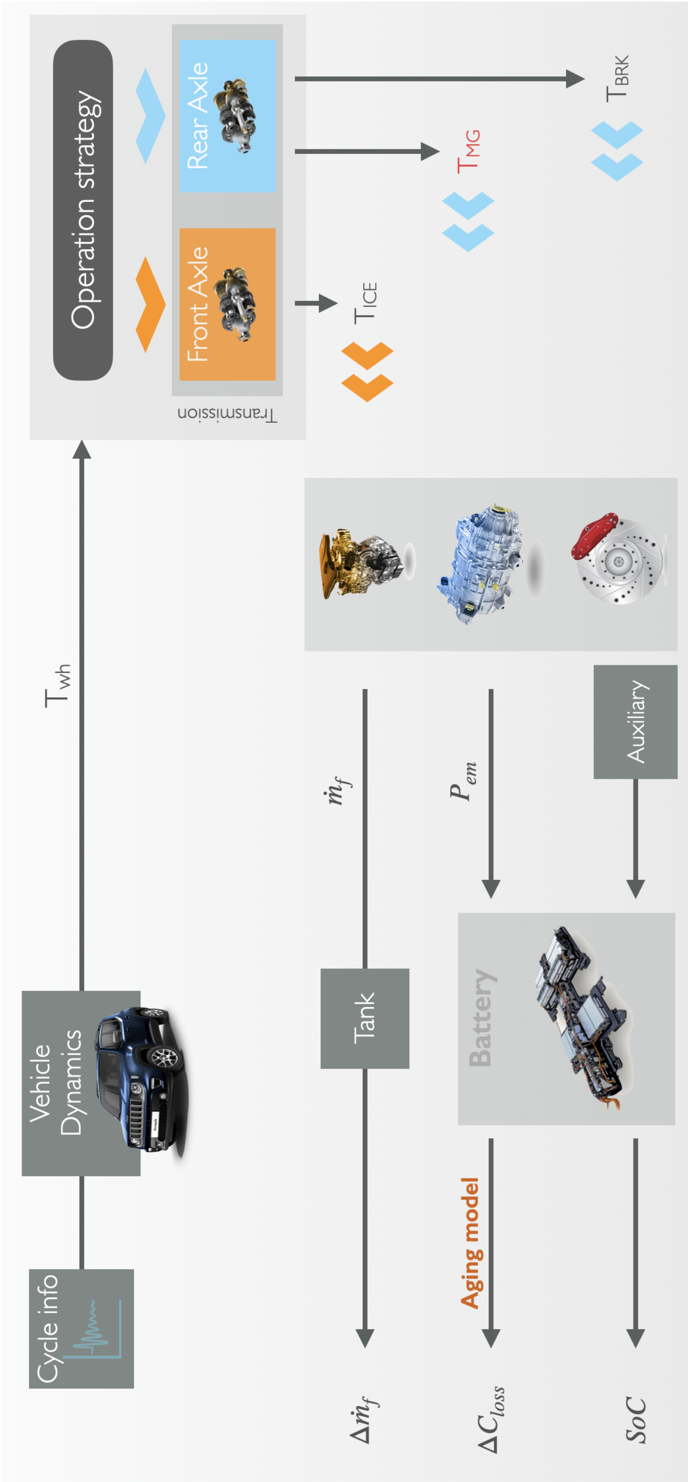

Figure 4.8: Signal flow in the simulation model.

4.3 ECMS

Regardless of the powertrain topology, the essence of HEV control problem is the instantaneous managament of power flows from energy converters to achieve the control objectives, [25]. Control objectives are mostly integral in nature (e.g., fuel consumption) or semi-local in time, such as drivability while the control actions are local in time, as deeply explained in [25]. Besides that, the control objectives are often subject to integral constraints like keeping the state-of-charge within a predetermined range. Generally speaking, the energy management problem in HEV can be transformed into an optimization problem over a finite time horizon [25], whose solution can be found with *optimal control theory* methods. Those methods are very useful in finding the control law for a given system such that a certain "optimal criterion" is achieved.

The optimal energy management problem in HEV consists of finding the control that leads to the minimization of fuel consumption over the considered mission, see Eq.4.27. In Eq.4.27 $\dot{m}_f$ is expressed in g/s and it is the fuel flow rate. The solution of the problem would be the solution which minimizes the performance index J. Obviously the minimization of J is subject to a number of constraints [25] linked for example to the limitation in the energy stored in the REES and the need to maintain SoC within a specific range. All these considerations make the control problem a *constrained, finite-time optimal control problem* where the objective function has to be minimized under several constraints [25].

$$J = \int_{t_0}^{t_f} \dot{m}_f(u(t), t)dt \tag{4.27}$$

The Equivalent Consumption Minimization Strategy (ECMS) is a heuristic method to address the optimal control problem. ECMS was firstly applied by Paganelli in 1999 as a method to reduce the global minimization problem to a local minimization problem to be solved at each time instant.

The ECMS is based on the notion that, in charge-sustaining HEVs, the difference between the original and final SoC level is perfectly negligible. This means that the energy storage system is mainly used as buffer: all energy comes from fuel, and the battery can be seen as an auxiliary, reversible fuel tank. Any stored electrical energy used during battery discharge must be restored/recovered at some point in the future. Two cases are possible [25]:

1. The battery power is positive (discharge) at the present time fig.4.9a; this implies that in the future the battery has to be recharged resulting in some additional fuel consumption. How much fuel will be required to restore the SoC lost depends mainly on two factors: (1) the operating condition of the engine at the time the battery is recharged; and (2) the amount of energy that can be recovered through regenerative braking.

2. The battery power is negative (charge): the stored energy is used to help the engine in satisfying the vehicle road load causing an instantaneous fuel saving fig.4.9b.

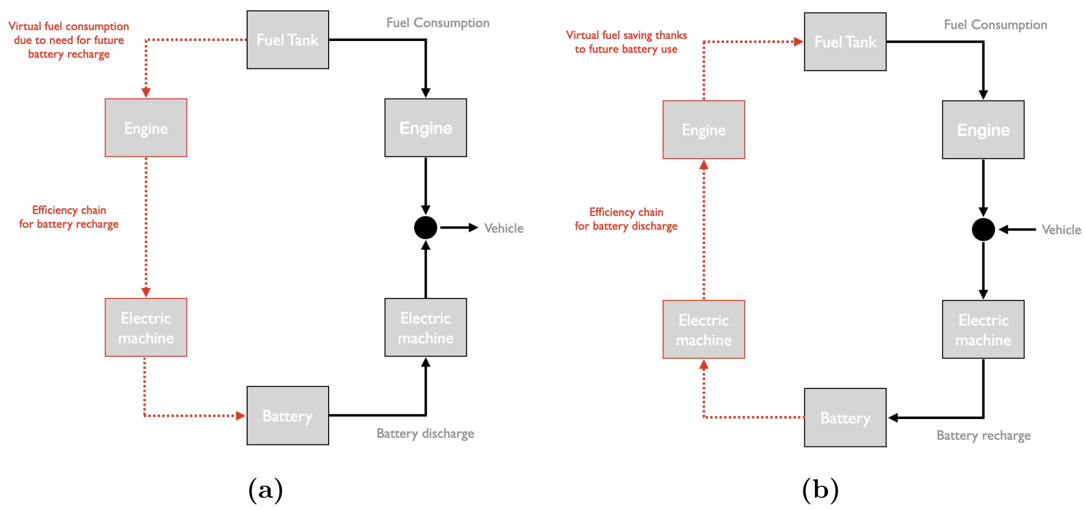

Figure 4.9: Energy path during discharge (a) and charge (b) in a parallel HEV [25].

The main principle of the ECMS is that a cost is assigned to the electric energy in such a way the use of electrical energy is made equivalent to use (or save) a certain quantity of fuel. Obviously this weighting factor is not known *a priori* but it has been shown that the cost can be related to the driving conditionn in a broad sense.

In the discharge case of fig.4.9a the electric machine provides mechanical power and the battery is discharging. The dotted red route represents a virtual fuel consumption related to the need of future battery recharge: an approximate mean efficiency is set given that the operating point of this recharge is not known a priori.

Conversely in the case of fig.4.9b the electric machine behaves as a generator and technically it converts mechanical power into electrical power used to recharge the battery pack on board. Even in this case the dotted red path represents a virtual fuel saving due associated to the future use of electric energy to produce mechanical power. This amount of mechanical energy has not to be supplied by the ICE and for this reason it is a fuel saving.

In both discharge and charge phase an equivalent fuel consumption can be associated with the use of electrical energy: the equivalent future (or past) fuel consumption, $\dot{m}_{REES}$ [g/s], can be summed to the present real fuel consumption

- fuel mass flow rate $\dot{m}_f(t)$ [g/s] - to obtain the instantaneous fuel consumption, $\dot{m}_{f,eqv}(t)$ as in the following equation.

$$\dot{m}_{f,eqv}(t) = \dot{m}_f(t) + \dot{m}_{REES}(t) \tag{4.28}$$

As deeply explained in [25] similarly to a traditional ICE which consumes real fuel, Eq.4.29, the electric machine "burns" a certain "virtual fuel" amount, Eq.4.30.

$$\dot{m}_f(t) = \frac{P_{eng}(t)}{\eta_{eng} Q_{lhv}} \tag{4.29}$$

$$\dot{m}_{REES}(t) = sfc_{eq}(t) \cdot P_{batt}(t) \tag{4.30}$$

In Eq.4.29 P_{eng} is the power supplied by the engine, η_{eng} is the operating efficiency of the internal combustion engine and Q_{lhv} is the fuel lower heating value in [MJ/kg]. In Eq.4.30 the virtual fuel consumption is computed using a *virtual specific fuel consumption*, sfc_{eq} [g/kWh] which in turn is directly proportional to an *equivalence factor s(t).* Thus the virtual fuel consumption, $\dot{m}_{REES}$ is evaluated as in Eq.4.31.

$$\dot{m}_{REES} = \frac{s(t)}{Q_{lhv}} \cdot P_{batt}(t) \tag{4.31}$$

The equivalence factor *s(t)* is a vector of values, one for charge and one for discharge. The main objective of the equivalence factor as explained before is to assign a cost to the use of electricity, converting electrical power into equivalent fuel consumption. The equivalence factor *s(t)* represents the efficiency chain for energy conversion (from mechanical to electrical and vice-versa).

Depending on the operating mode of the battery (charge or discharge), the virtual fuel flow rate can be either positive or negative, thus increasing or decreasing the equivalent fuel consumption with respect to the real fuel consumption $\dot{m}_f$.

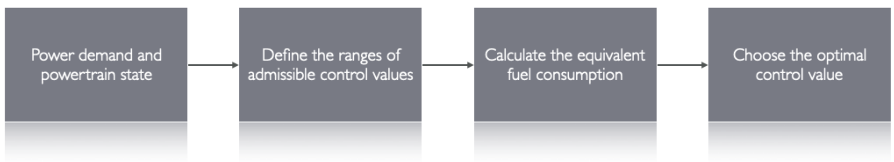

Figure 4.10: ECMS algorithm flow [25].

The ECMS is used to reduce the global optimization problem of the total cost in a local (instantaneous) optimization problem. At each time instant, the equivalent fuel consumption should be evaluated with Eq.4.28 for different value of control variables which in our case is the torque of the electric machine. The following passages [25] must be repeated at each time instant, as showed in fig.4.10, to realize the ECMS:

1. Given the state of the system in terms of T_{wh}, ω_{ICE}, ω_{MG}, $\ldots$, identify the acceptable range of control $[T_{MG,min}, \ldots, T_{MG,max}]$ which satisfies the instantaneous constraints;

2. Discretize the interval $[T_{MG,min}, \ldots, T_{MG,max}]$ into a finite number of control candidates;

3. Calculate the equivalent fuel consumption corresponding to each control candidate;

4. Select the control value $T_{MG}(t)$ that minimizes the equivalent fuel consumption at each time instant;

It has been proven that this approach closely approximate the global optimal solution. Moreover the instantaneous minimization problem requires a lower computational effort if compared with the *dynamic programming* and it can be applied real-worlds situations since it does not rely directly on information about future driving conditions.

4.4 Multi-Objective ECMS

Ebbensen et al. in [23] develop a causal optimal control-based energy management strategy for a parallel hybrid electric vehicle. The control scheme of *Ebbensen et al.* not only tries to reduce fuel consumption but to minimize battery wear. The optimal control problem formulated by *Ebbensen* et al is reported in Eq.4.32 and Eq.4.32. Namely the control problem consists of finding the optimal control strategy u that, subject to a number of constraints, minimizes the equivalent fuel consumption on the mission. The optimization problem can be expressed mathematically as in Eq.4.32 and Eq.4.32.

$$\min_u : \quad \int_0^T P_f(u, v, a, t)dt \tag{4.32}$$

$$\begin{aligned}
&\dot{x}_1(t) = -P_i(u(t))/Q_0(0) \\
&x_2(t) = -|P_i(u(t))|/(2 \cdot N(|P_i(u(t))|) \cdot Q_0(0) \\
&x_1(0) = x_{1,0} \\
&x_2(0) = 1 \\
&x_1(T) \geq x_{1,0} \\
&x_2(T) \geq 0 \\
&x(t) \in \chi \\
&u(t) \in U(t)
\end{aligned} \tag{4.33}$$

In [23] the state and input constraints are defined by the sets χ and U, respectively. In [23], $\chi in[0.3, 0.9]$ is fixed on the state of charge to preventively avoid large discharge rate. The idea is to introduce a *state of health* perceptive energy management strategy, as also done in [23] and in many other different papers. The ECMS desribed before try to improve fuel economy by an online minimization of a proper cost-to-go function composed by the sum of an instantaneous fuel consumption and an equivalent fuel consumption, converted through an *equivalence factor*. The ECMS derives from the *Pontryagin's minimum principle* and under certain hypothesis it leads to the globally optimum solution.

The *Pontryagin's minimum principle* applied to the optimal control problems of [23] leads to the definition of an Hamiltonian function as in Eq.4.34. Furthermore Eq.4.34 can be rewritten as in Eq.4.35.

$$H(u(t), \lambda(t), t) = P_f(u(t)) - \lambda_1(t) \cdot \dot{x}_1(t) - \lambda_2 \cdot \dot{x}_2(t) \tag{4.34}$$

$$\begin{aligned} H(u(t), \lambda(t), t) = & \, P_f(u(t)) \\ & + s_1(t) \cdot P_i(u(t)) \\ & + s_2(t) \cdot w(u(t)) \cdot |P_i(u(t))| \end{aligned} \tag{4.35}$$

Eq.4.35 is made by three main terms: (1) P_f is the chemical power introduced through the fuel; (2) $s_1(t) \cdot P_i(u(t))$ is the term accounting for the use of electrical energy and s_1 is the actual cost of electricity; (3) $s_2(t) \cdot w(u(t)) \cdot |P_i(u(t))|$ is the "ageing" conscious part of the model. s_1 *and* s_2 in Eq.4.35 are expressed in Eq.4.36 and in Eq.4.37 respectively. The weight $w(u(t))$ in Eq.4.35 is simply for *Ebbensen et al.* the ratio $1/N(u(t))$.

$$s_1(t) = -\lambda_1(t) \cdot \frac{1}{Q_0(0)} \tag{4.36}$$

$$s_2(t) = -\lambda_2(t) \cdot \frac{1}{2 \cdot Q_0(0)} \tag{4.37}$$

It is worth to notice that for $s_2(t) = 0$ the Hamiltonian function Eq.4.35 reduce to the traditional ECMS. If $s_2(t) > 0$ an extended version of the ECMS is obtained where the traditional ECMS is augmented by a term penalizing both battery charging and discharging.

The optimal solution must satisfy the constraints reported in Eq.4.33 and also the following adjoint equations:

$$\dot{s}_i(t) = -\frac{\partial H}{\partial x_i(t)} \quad i = \{1{,}2\}$$

Finally the optimal control trajectory is given:

$$u^*(t) = arg \min_{u \in U} H(u, s(t), t) \tag{4.38}$$

The Hamiltonian function is independent of $x(t)$. The adjoint equations say that $s_1(t)$ and $s_2(t)$ are constants. In the following the same strategy of *Ebbensen et al.* is used in the formulation of the cost-to-go function. The idea is to derive an extended version of the traditional ECMS to preserve as much as possible battery life. Although the *standard version* of the ECMS provides quickly reliable results it is no longer suitable to meet the need of actual HEVs. Li-ion batteries constitute an important part of the vehicle cost and from this the necessity to preserve their performances in operation. Fuel consumption-only oriented control strategies tend to minimize fossil fuel consumption by severely exploiting the REES. A severe exploitation of the electrochemical system will lead to a severe aging hence battery life is drastically diminished. This is the reason why a more "health-conscious" control strategy is needed to account for both fuel consumption and battery ageing.

4.5 MG power saturation level

In fig.4.11a and fig.4.11b some important results are presented. The control variable u (the torque of the electric machine) is ranging from 0 up to 54%. Technically speaking it means that the electric machine can provide up to 54% of the torque request at the wheel. This value (54%) is not casual rather it is a direct consequence of the MG power saturation level: if the electric machine is called to provide an higher percentage the power saturation level is reached. In fig.4.11a the MG power is reported in time considering different control candidates. The first candidate $u = 43\%$ is within the operating power range of the electric machine and power saturation level is not reached in operation. By choosing a more severe control strategy power saturation level is likely to be reached especially in the extra-high phase of the WLTC which is the most demanding phase ($P_{MG,max} = 44.7 \quad$ [kW]).

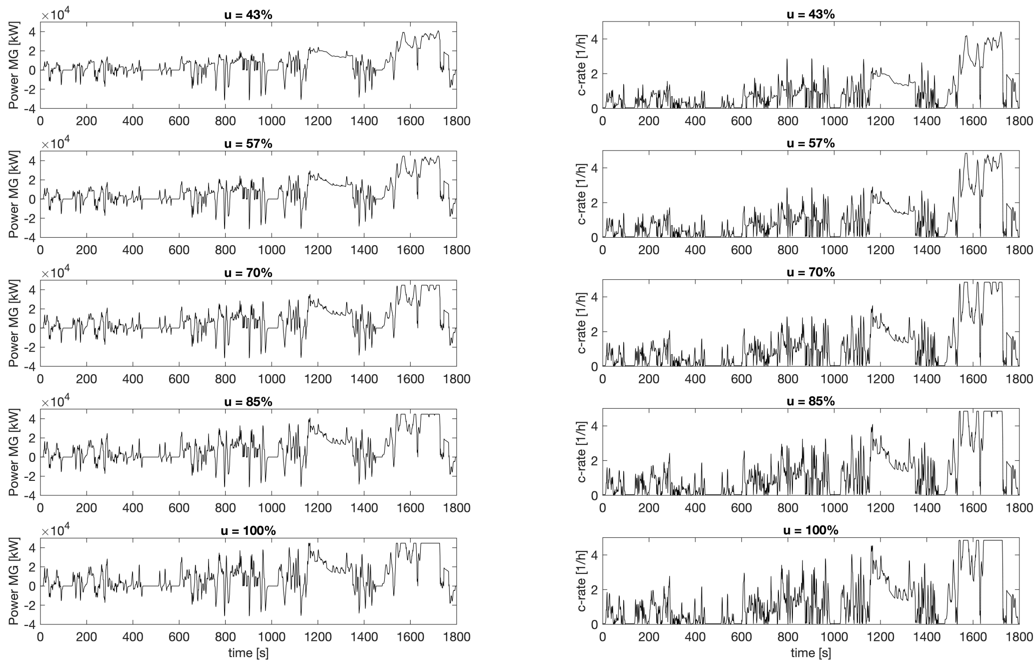

(a) **(b)**

Figure 4.11: MG power saturation level: (a) MG power in [kW] in time for different control candidates (43%, 57%, 70%, 85%, 100%) and (b) c-rate [1/h] in time for different control candidates (43%, 57%, 70%, 85%, 100%). The driving cycle considered is the WLTC.

In fig.4.11b the c-rate is reported in time for different control candidates. Also in this case with the least severe control strategy ($u = 43\%$) power saturation level of the electric machine is not reached. By increasing the percentage of the torque request that burdens the MG unit, the power saturation level of the electric machine is reached and the discharge-rate of the battery is capped and limited at a value lower than 5 [1/h]. By fixing the power of the electric machine also the c-rate experienced by the battery in operation is somehow limited. This choice may be helpful in limiting battery ageing through an "indirect saturation" of the discharge rate but at the same time severely restricts the potential of a PHEV.

Another interesting consideration is that the power saturation level of the electric machine is reached only during discharging operation: when the MG is functioning in *motoring mode*. When the MG unit is used in *generating mode*, negative power values, the saturation level is not reached. The results presented in fig.4.11 are not considering any regeneration-torque control meaning that T_{wh} is entirely regenerated and used to recharge the battery pack (obviously when $T_{wh} < 0$). This strategy may be helpful in guarantee the charge-sustaining mode but surely battery ageing will proceed faster.

In fig.4.12 different regeneration-torque control-strategies are reported in terms of MG power in time, Tab.4.1. In fig.4.12a no regeneration control is foreseen meaning that the entire torque at the wheel (when $T_{wh} < 0$) powers the generator to recharge the battery pack. This is the worst strategy in terms of useful battery life. In fig.4.12b the regeneration control is made with one only control variable (u). In this case u, used in motoring mode, is also adopted to control the regeneration phase. This is the most conservative strategy and leads to the longest battery life. The third and last strategy, reported in fig.4.12c, differentiates the two control (traction and regeneration) by using two different control variables (u and u^1).

No Regeneration Control	6.39 [l/100km]
	116,793 [km]
	0,24854 [-]
Regeneration Control with u	6.49 [l/100km]
	160,158 [km]
	0,21318 [-]
Regeneration Control with u_1	6.38 [l/100km]
	119,098 [km]
	0,2511 [-]

Table 4.1: Results obtained with different regeneration control strategies in terms of fuel consumption, battery life and SoC at the end of the mission. Results obtained with $s_1 = [1.93,1]$ and $s_2 = 88.2$.

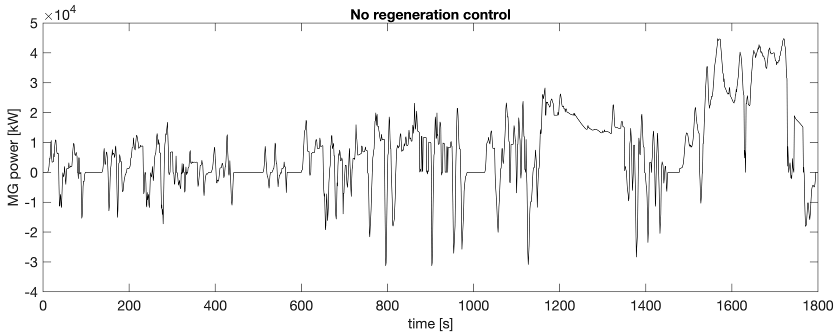

(a)

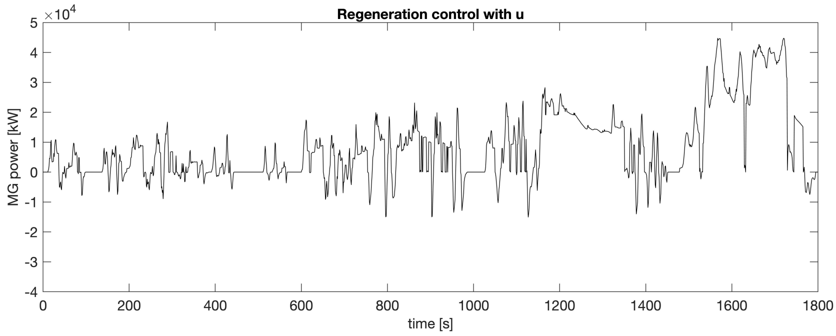

(b)

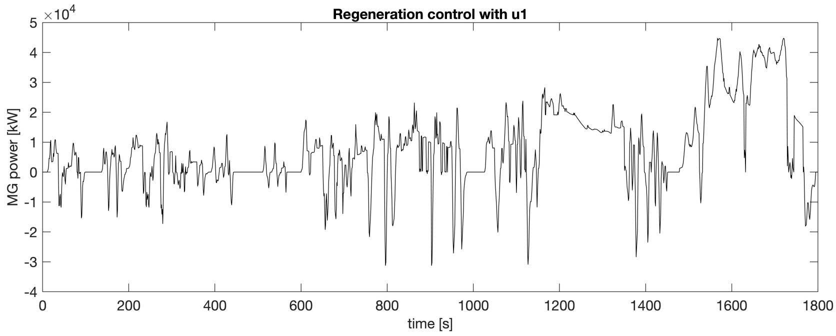

(c)

Figure 4.12: Motor-Generator unit power in time for different regeneration-torque control-strategies: (a) no regeneration control; (b) regeneration control with one control variable (u); (c) regeneration control with two control variables.

4.6 MO-ECMS calibration and results

The starting point of the calibration is the original ECMS ($s_2 = 0$). By increasing the value of the equivalence factor s_2 battery degradation becomes crucial in deciding the control strategy. The optimization cycle is constituted by two well distinguished phases. Since the original ECMS is extremely demanding for the battery pack the first step of the optimization cycle has been to find a better solution from the battery-health perspective. The main driver of this phase is to preserve battery health in operation. The battery-health oriented optimization phase effectively leads to a lower battery ageing in operation but the fuel consumption increases significantly. The MG unit is underused to target the first objective and by doing so the potential advantages of HEVs are strongly resized/reduced. The last phase of the optimization cycle is in charge of the fuel consumption reduction while keeping under control battery ageing.

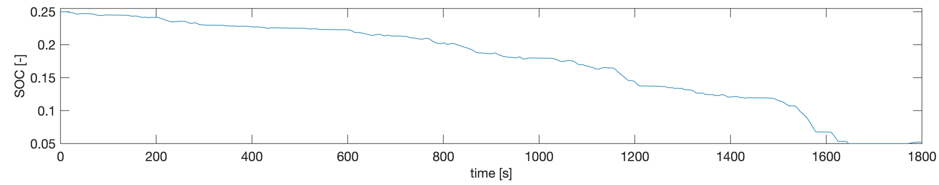

(a)

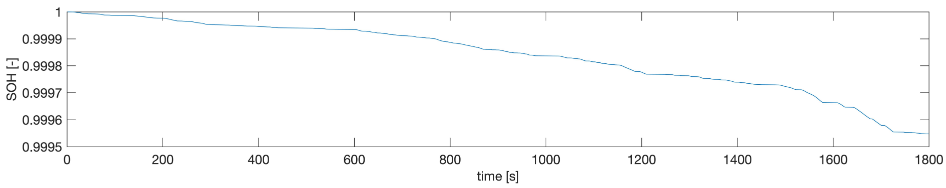

(b)

Figure 4.13: Original ECMS, $s_1 = [1, 1]$ and $s_2 = 0$. Regeneration-torque control with u. (a) *State-of-Charge* trend in time along the WLTC and (b) *State-of-Health* trend in time along the WTLC.

In fig.4.14 the results in terms of operating points are presented on the ICE and MG map. By imposing $s_2 = 0$ the cost-to-go function (Eq.4.35) reduces to the original ECMS. The original ECMS seeks to maximize fuel economy, it is not "conscious" of battery degradation: this is evident looking at the *State-of-Health* trajectory depicted in fig.4.13b. Given that the electric machine is mainly used as motor the *State-of-Charge* is vertically depleted, fig.4.13a. From these considerations it is clear that the traditional ECMS leads to have the best fuel consumption but also the highest battery degradation. Fig.4.14b shows the operating points of the electric machine: in the original ECMS the MG unit is extensively used. The operating points of the internal combustion engine, instead, are localized in a quite limited area and they are characterized by lower torque value (the missing torque with respect to T_{wh} is provided by the electric machine). The key idea of this work is to sensitize the ECMS to battery health preservation to achieve a optimal solution both in terms of fuel consumption and battery life.

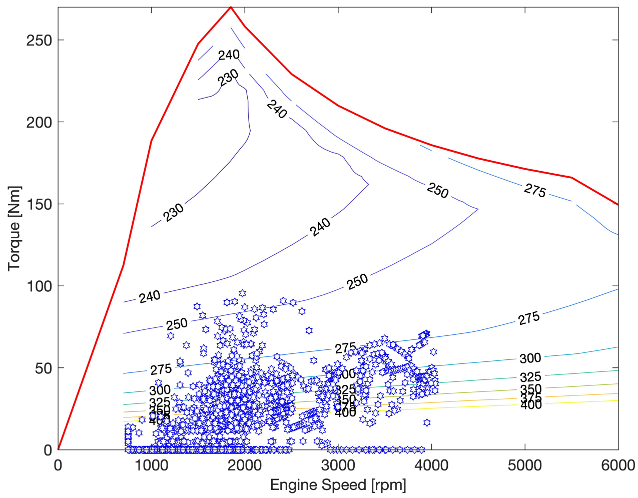

(a)

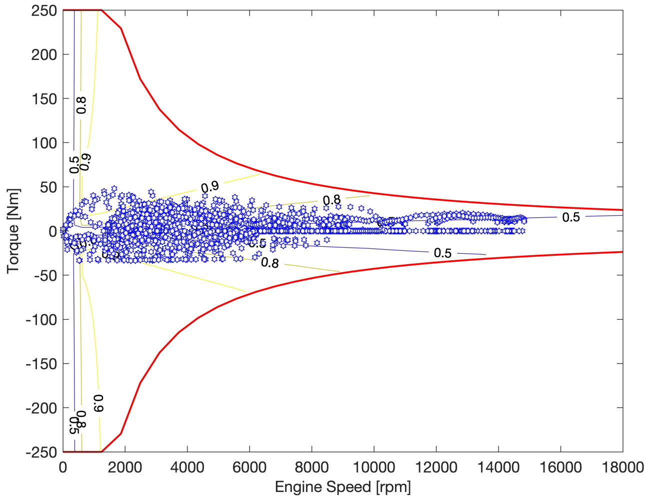

(b)

Figure 4.14: Original ECMS: operating points on the ICE map (a) and on the electric machine map (b).

By increasing the value of the equivalence factors s_1 and s_2 it is possible to obtain a better solution from the point of view of the battery. By imposing $s_1 = [2.121]$ and $s_2 = 100$ the results reported in fig.4.15 and in fig.4.16 can be observed.

This simulation is an important step forward to preserve battery in operation with respect to the traditional ECMS. Battery aging can be reduced and battery life can be increased in terms of km. Obviously this has a cost and the cost is hidden in the increased fuel consumption. Fuel consumption is 6.77 l/100km while battery end on life happens after 230,533 km. By comparing fig.4.15 and fig.4.13 it is immediate to see that with this calibration a charge sustaining mode is ensured and the *state-of-health*, which provides a reliable measure of the battery health, remains quite flat if compared with the original ECMS. This is definitely the first big difference between the two calibrations. With the original ECMS, battery SoC is severely depleted since the battery operates with important discharge currents to power the MG unit.

By comparing instead the ICE and the MG maps, fig.4.16, it is possible to draw other important conclusions: the operating points of the MG appears reduced and in any case the electric machine is mainly used as generator. Motoring functioning of the electric machine is strongly limited to preserve battery performances in time. Furthermore the operating points on the ICE map are spread on a larger zone since the internal combustion engine now has to provide an higher torque (to compensate for the under-utilization of the electric machine).

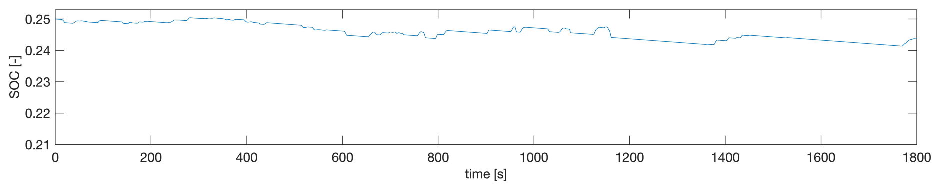

(a)

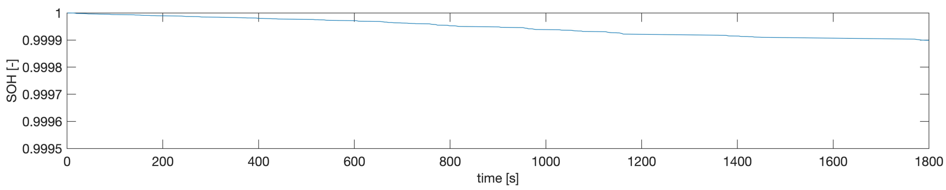

(b)

Figure 4.15: $s_1 = [2.12, 1]$ and $s_2 = 100$. Regeneration-torque control with u. (a) *State-of-Charge* trend in time along the WLTC and (b) *State-of-Health* trend in time along the WLTC.

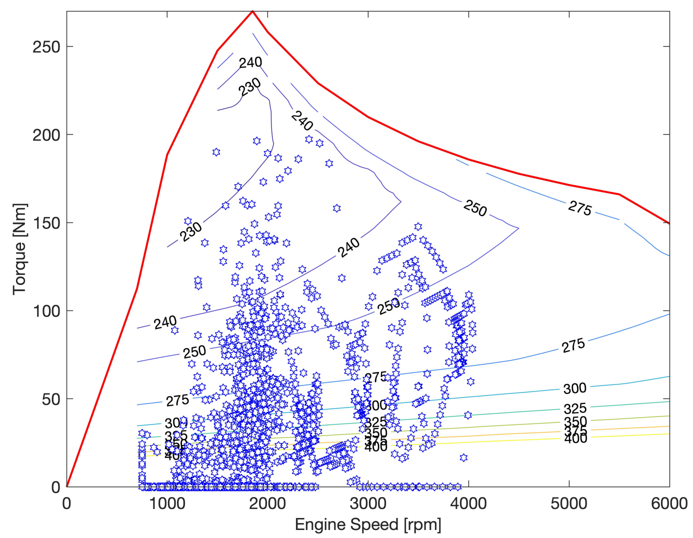

(a)

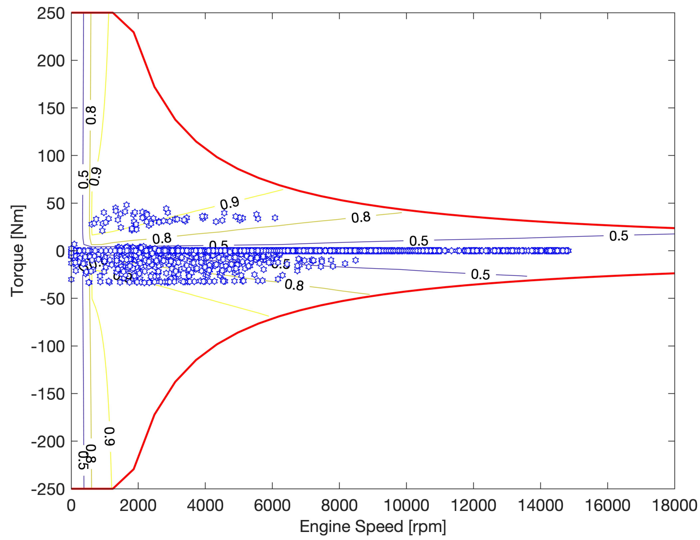

(b)

Figure 4.16: $s_1 = [2.12, 1]$ and $s_2 = 100$. Operating points on the ICE map (a) and on the electric machine map (b).

The simulation showed in fig.4.16 allows the battery to last for about 230,000 km but with a fuel consumption of 6.77 l/100km. Given that the carmakers usually offer an 8-years (or 160,000 km) warranty on the battery pack it is possible to "convince" and force the control algorithm to take more advantage from the electric part of the powertrain in order to achieve a reduction in the fuel consumption. Practically speaking this corresponds to the second step of the optimization cycle. With this calibration ($s_1 = [1.93, 1]$ and $s_2 = 88.2$) the fuel consumption turns out to be 6.49 l/100km while the battery life is of about 160,158 km.

Now the operating points on the ICE map, fig.4.18a, appear to be less while the electric part is exploited more than the previous calibration to reduce fuel consumption. The electric machine is mainly used as generator to recharge the battery pack and to assist the internal combustion engine during sharp transient operations. There are not significant differences in the *SoH* profile, reported in fig.4.17b whereas the *SoC* profile is quite different with respect to that reported in fig.4.15a. By decreasing the values of the equivalence factors s_1 and s_2 the control becomes more fuel-oriented. By setting the equivalence factor for the electricity consumption to 1.93 and the equivalence factor for the battery ageing to 88.2 it is possible to find a better solution for the fuel consumption. The idea is to use part of the 230,000 km of the previous simulation as margin to achieve a fuel consumption benefit.

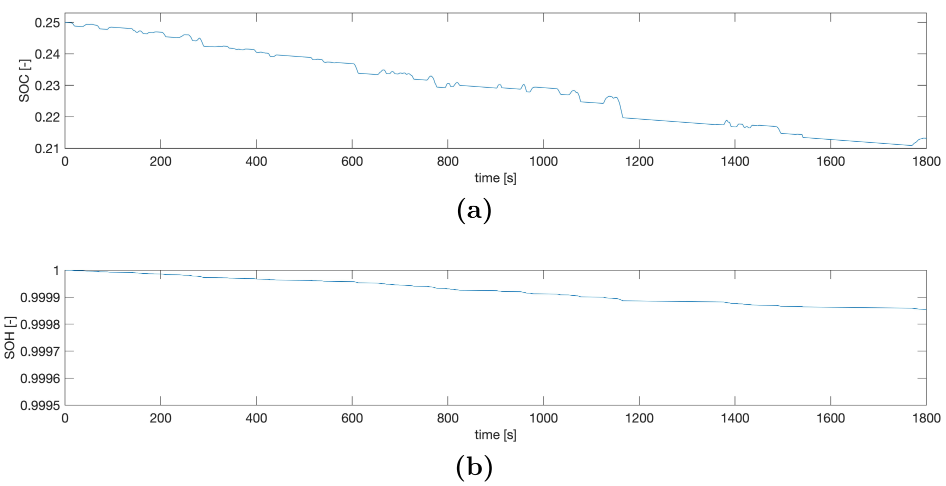

Figure 4.17: $s_1 = [1.93, 1]$ and $s_2 = 88.2$. Regeneration-torque control with u. (a) *State-of-Charge* trend in time along the WLTC and (b) *State-of-Health* trend in time along the WTLC.

The *leitmotif* of these study is that s_1 is impacting more than s_2 and this sentence can be explained simply by understanding how the cost-function (Eq.4.35) has been defined. In the definition of the cost-function the absolute value of the battery internal power is weighted on the number of cycle to EOL thus the impact of s_2 on the calibration outcomes is somehow mediated by $w(u(t))$. On the contrary s_1 is impacting directly on the cost-to-go function.

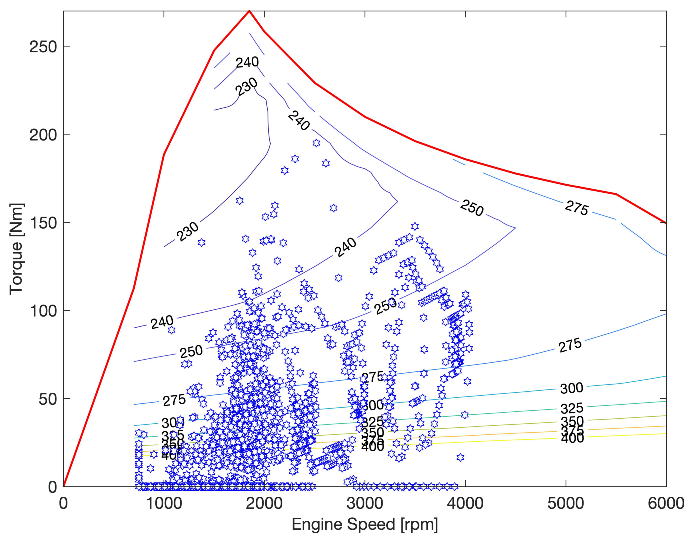

(a)

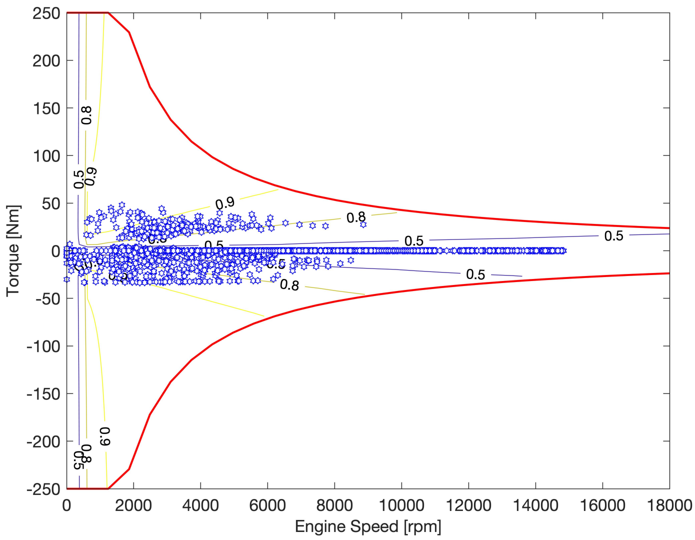

(b)

Figure 4.18: $s_1 = [1.93, 1]$ and $s_2 = 88.2$. Operating points on the ICE map (a) and on the electric machine map (b).

In Tab.4.2 the main results of the analysis in terms of fuel consumption and battery life. The fuel consumption records in the table, and in the entire thesis work, have been corrected according to the ECE/TRANS/180 standard according to which whenever the *State-of-Charge* at the end of the mission is lower than the initial value a fuel correction should be applied. Practically speaking if the SoC at the end of the mission is lower than the initial value some fuel must be virtually consumed to recharge the battery pack up to the original SoC.

	Fuel Consumption [l/100km]	Battery Life [km]
$s_1 = [1,1]$ and $s_2 = 0$	4.9257	51,416
$s_1 = [2.12,1]$ and $s_2 = 100$	6.7706	230,533
$s_1 = [1.93,1]$ and $s_2 = 88.2$	6.4913	160,158

Table 4.2: Main results of the analysis in terms of fuel consumption and battery life for the three calibration seen before. Results obtained with the *SoH* model of *Ebbensen revised*.

In fig.4.19 the most important result of the analysis is reported: the Pareto front between fuel consumption and battery life. This plot easily allows to explore the trade-off between fuel consumption and battery life. By changing the value of s_1 and/or s_2 it is possible to move on the trade-off curve obtained.

The Pareto front has been obtained with a s_2 sweep for different s_1 values. The stronger impact of s_1 with respect to s_2 is clearly demonstrated in the Pareto front. The action of s_1 is more effective in changing the outcomes of the analysis.

The blue part of the trade off curve has been obtained by sweeping s_2 and keeping fixed s_1: in this part the trade off is quite sharp and appears to be quite vertical. This verticality translates in an important dependency of the fuel consumption on the equivalence factor for the battery ageing. By changing the value of s_2 (for a given value of s_1) battery life remains almost unchanged while the consumption sharply increases.

The yellow part of the trade off is the result of a s_2 sweep with $s_1 = 1.4$: this zone is more flat meaning that by increasing the value of s_2 fuel economy gets worse but battery life increases almost in the same proportion.

The last part, the green one, has been obtained with a s_2 sweep while maintaining $s_1 = 1.8$. It is the flatter zone: if s_2 changes the effects on fuel consumption are marginal while the effects on the battery life are significant. The "same" trade-off can be obtained by keeping s_1 fixed and sweeping only s_2 toward very high values (to obtain comparable values). By changing s_1 it is possible to "move" faster on the trade-off curve. According to the trade-off region the relative impact of s_2 is different. In the first zone the effect of s_2 on fuel consumption is quite important while its effects on battery life is marginal. In the last part the opposite is likely to happen: the effect of s_2 on fuel consumption is "negligible" while the effect on battery health is significant.

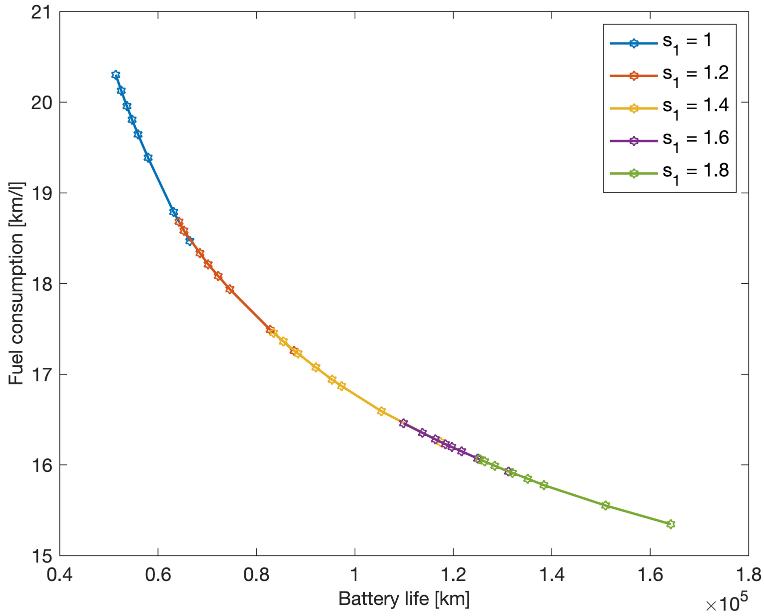

Figure 4.19: Pareto front between fuel economy and battery life for different s_1 values. Each front has been obtained by sweeping the equivalence factor s_2 (0, 20, 40, 60, 80, 100, 150, 200).

4.7 Gearshift strategy

In a PHEV two variables have to be controlled at each time instant: the gear engaged and the torque split between the ICE and the electric machine. While for the torque split a control logic based on the ECMS has been defined in the previous paragraphs for the gear engaged a rule-based control is applied.

When the engine speed overcomes 2000 [rpm] an higher gear is engaged whereas when the engine speed falls below 1000 [rpm] then a lower gear is chosen. Obviously this gearshifts happen within the model with a certain delay (respect to the attainment of the threshold rpm). This delay is not only induced by analytical reason also it is used to give more credibility to the model trying to bring it closer to what happens in reality. During real driving conditions the gearshift is not performed instantaneously rather it happens with a certain delay. When the threshold is reached (both for up-shift and down-shift) the "new" gear is engaged only with a certain delay.

Tab.4.3 shows the results obtained with different gear shift strategies in terms of induced delays in terms of fuel consumption, battery life, final SoC and number of gearshifts. For the fuel consumption the trend is quite clear: the higher the induced delay the higher the fuel consumption. On the other hand for the battery life the trend is not so clear: we can conclude that battery life is almost insensitive to induced delay. Also the SoC registered at the end of the mission appears to be not influenced by the gear-shift delay. The last row of Tab.4.3 reports the number of gearshift along the WLTC driving cycle: the higher the delay the lower the number of gearshifts.

	1s delay	2s delay	3s delay
Fuel consumption [l/100km]	6.4913	6.5296	6.5653
Battery life [km]	160158	159640	160052
SoC @ the end [-]	0.21318	0.2129	0.21296
Gearshifts nr. [-]	128	124	112

Table 4.3: Analytical comparison between gear strategies with different induced delay. The equivalence factors used in the ECMS to obtain these results are $s_1 = [1.93, 1]$ and $s_2 = 88.2$. Gearshift strategies are compared in terms of fuel consumption, battery expiring distance, SoC at the end of the mission and number of gearshifts.

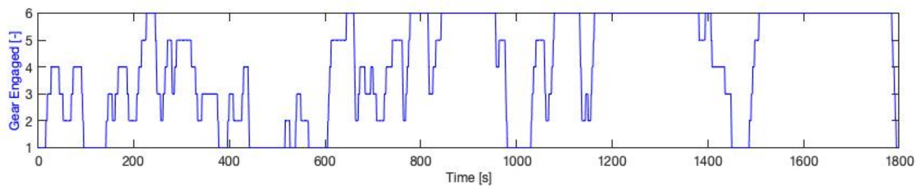

Figure 4.20: Gearshift strategy with 1 [s] delay in time.

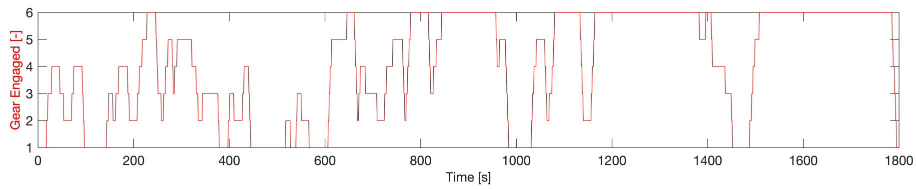

Figure 4.21: Gearshift strategy with 2 [s] delay in time.

In fig.4.20, fig.4.21 and fig.4.22 the gearshift profile, along the WLTC, is reported for 1 [s], 2 [s] and 3 [s] respectively. In fig.4.23 the results of the analysis are reported as operating points on the ICE and MG maps.

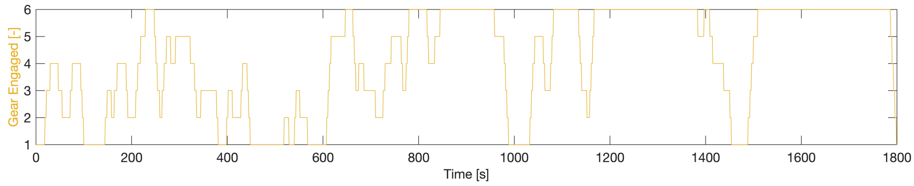

Figure 4.22: Gearshift strategy with 3 [s] delay in time.

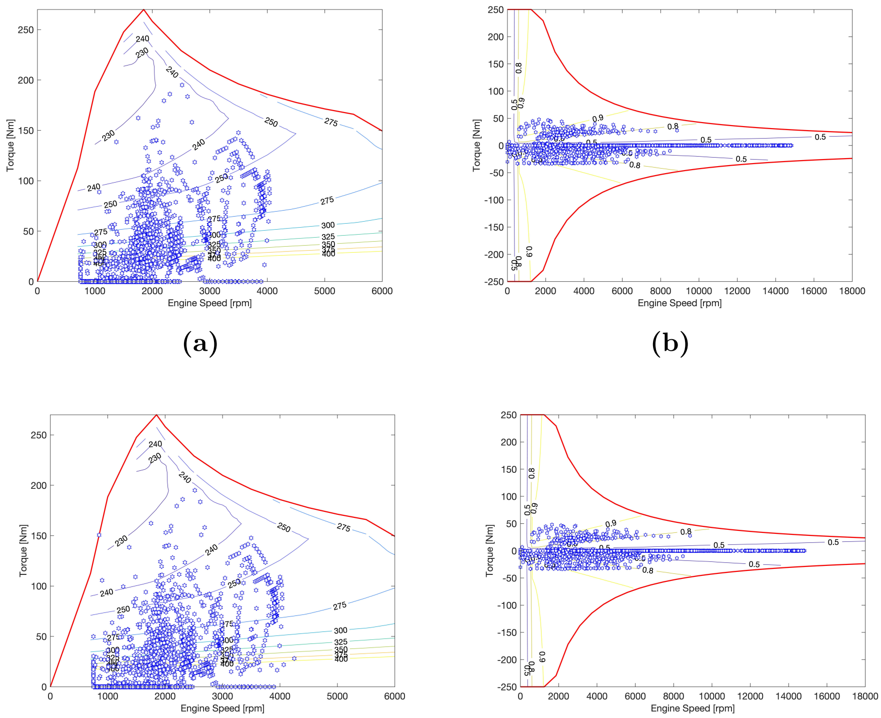

(a) **(b)**

(c) **(d)**

Figure 4.23: $s_1 = [1.93, 1]$ and $s_2 = 88.2$. In (a) operating points on the ICE map with 2 s delay in the gearshift; (b) operating points on the MG map with 2 s delay in the gearshift; (c) operating points on the ICE map with 3 s delay in the gearshift; (d) operating points on the MG map with 3 s delay in the gearshift.

By increasing the delay in the gearshift strategy the angular velocity of the internal combustion engine is likely to increase: if the delay increases the "actual" gear is maintained for a longer time before engaging another gear and the ICE speed progressively increases during this time interval. This is one of the most important results of the analysis: if the gearshift takes longer time the internal combustion engine has more time to continue raising its velocity. This effect can be clearly seen in fig.4.23a and fig.4.23c in terms of operating points and also in fig.4.24 where the engine speed in rpm is reported for the different induced delays.

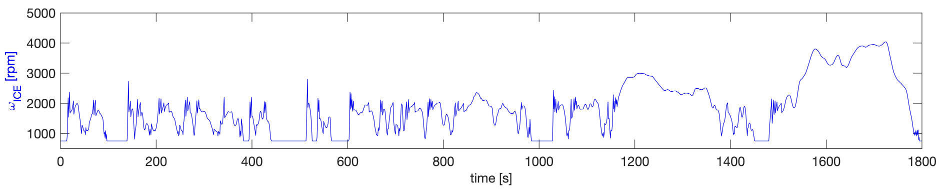

(a)

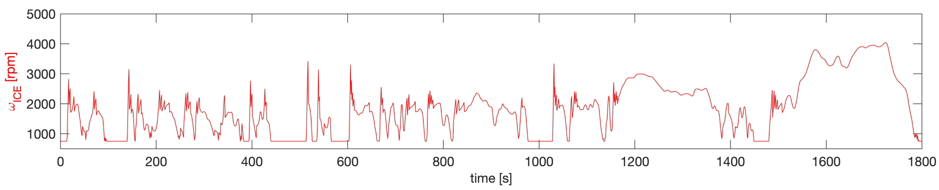

(b)

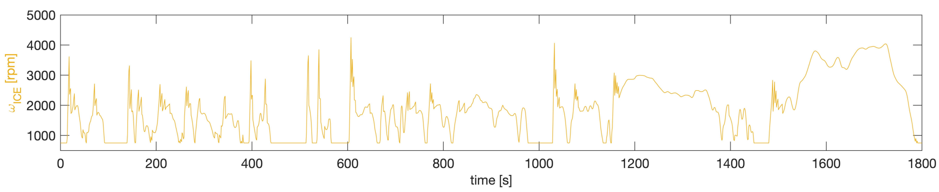

(c)

Figure 4.24: Engine speed [rpm] with 1 [s] delay (a) in the gearshift strategy; (b) engine speed [rpm] with 2 [s] delay in the gearshift strategy; (c) engine speed [rpm] with 3 [s] delay in the gearshift strategy.

4.8 Internal resistance analysis

The main goal of this section is to understand how the internal resistance of the battery varies for different operating conditions trying to identify the best operating conditions. Firstly it is necessary to distinguish discharging and charging operation of the battery. Fig.4.25 shows how the internal resistance of the battery varies as function of the *State-of-Charge* and the discharge rate during discharge operation. The maximum internal resistance of the battery in discharging operation is of about 0.3 Ω which is also representing the worst condition. This resistance value verifies within the battery for low SoC value and high discharge rates. If the battery operates under these conditions (low SoC and high *c*-rate) then it offers the maximum resistance to the current flowing through.

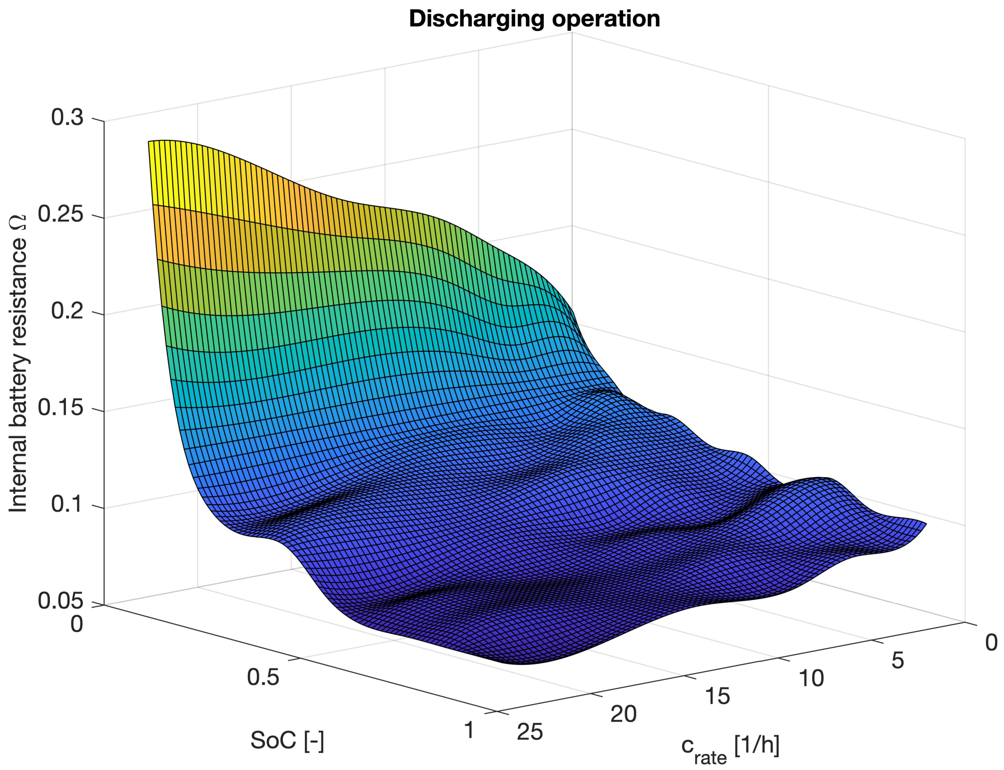

Figure 4.25: Battery internal resistance as function of the *c*-rate and the *State-of-charge* during discharging operation.

Similarly, fig.4.26 shows how the internal battery resistance is affected by operating conditions during charging. In this case the maximum resistance value is well below the maximum value found in fig.4.25. Also during charging operation the internal battery resistance surface appears to be quite flat meaning that the variability of operating conditions is definitely more "impacting" when the battery is discharging. However, in this case the battery shows the highest resistance for low charge/discharge rate and low SoC values. Under these conditions the maximum value is of about 0.1 Ω.

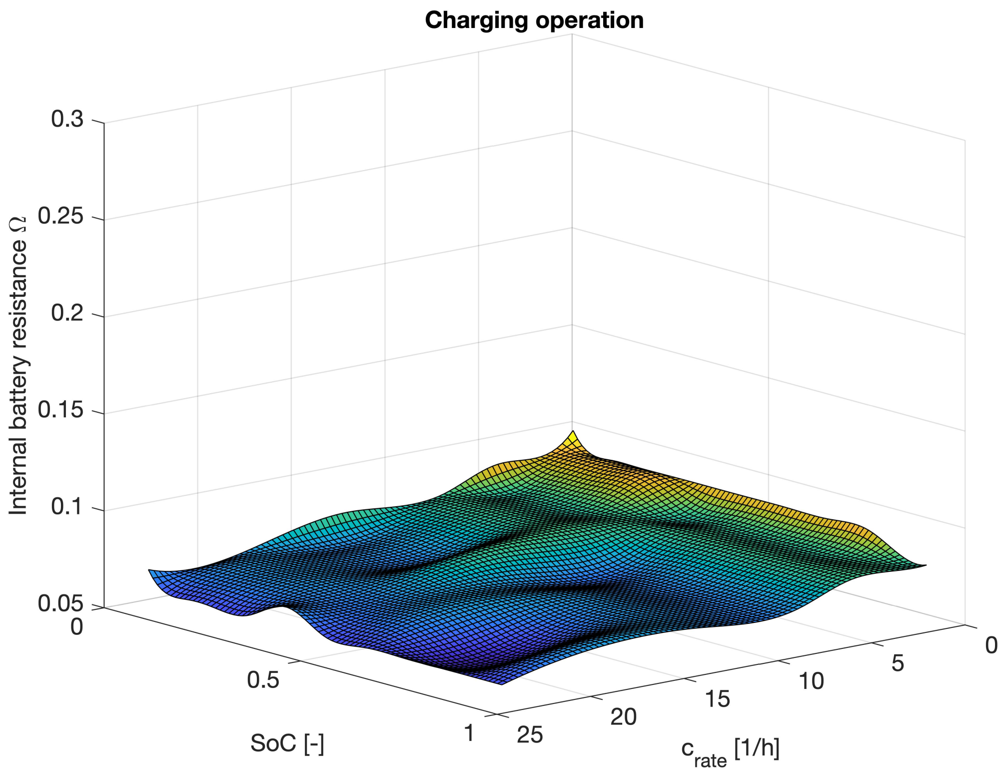

Figure 4.26: Battery internal resistance as function of the c-rate and the *State-of-charge* during charging operation.

The internal resistance offered by the battery to the current flowing through is highly influenced by the operating conditions. The resistance maps, reported in fig.4.25 and fig.4.26, are useful to understand which are the best operating conditions (in terms of SoC) for the battery. To isolate the SoC trend, the c-rate dependency has been eliminated by assuming an average c-rate value on the mission ($c_{rate,avg} = 1[h^{-1}]$). This average value is not casual but it is the result of the most aggressive control strategy for the battery pack. With $u = 54\%$ the discharge rate reaches the maximum (4.85 [1/h] saturated) and the average c-rate value on the mission turns out to be equal to 0.98 [1/h]. To be conservative an average value of 1 [1/h] has been considered.

The two curves reported in fig.4.27 are technically two sections of the resistance maps reported in the previous figures (fig.4.25 and fig.4.26). The plot reported in fig.4.27 allows to spot the optimal SoC windows from the battery point of view. Both the resistance curves (the red one and the blue one) reach a minimum in the neighbourhood of a SoC of 0.9 (precisely $SoC(r_{disch,min}) = 0.84$ and $SoC(r_{ch,min}) = 0.93$). Definitely the optimal SoC window is located around a SoC of 0.9.

The discharge resistance function has a local minimum at around $SoC = 0.6$ and in this range of SoC the charging resistance remains quite flat: it is an interesting window.

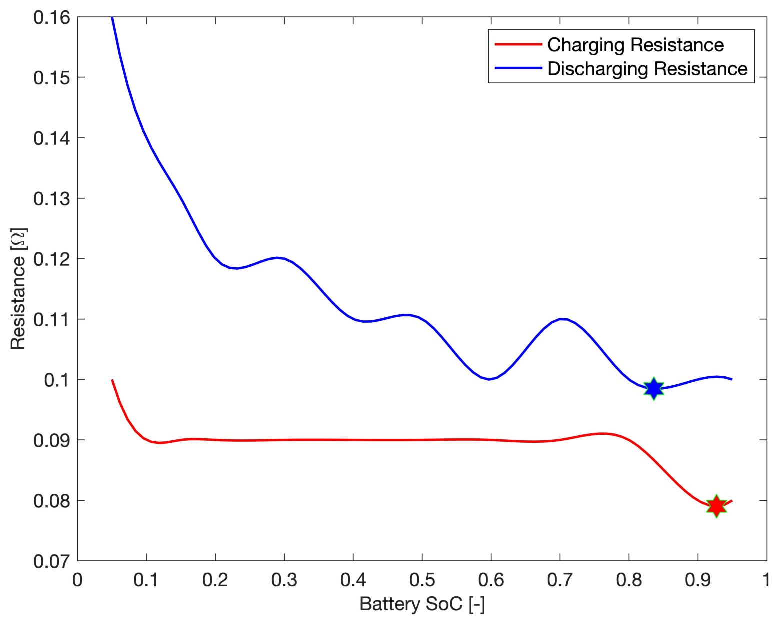

Figure 4.27: Internal charging resistance, red, and internal (discharging) resistance, blue, as function of the *state-of-charge* of the battery. Identification of the local minimum.

The idea now is to exploit this knowledge to force the battery operates in the best possible conditions. All the simulations done before consider an initial SoC of 25%. To place the battery in the best possible conditions an initial SoC of 84% has been chosen. By keeping constant the ECMS calibration ($s_1 = [1.93, 1]$ and $s_2 = 88.2$) if the battery operates in one of the optimal SoC windows identified before then the advantages are obvious, Tab4.4.

In Tab.4.4 two situations are compared, namely the operation out of the first optimal SoC window and the operation within the first optimal SoC window. The initial SoC considered to force the battery operate under optimal conditions is of 84%. If the battery works within the optimal SoC window (and the ECMS calibration remains the same) the fuel consumption is slightly reduced (from 6.49 to 6.47 l/100km) and battery life is increased. By forcing the battery to operate in this SoC window two benefits are recorded: fuel consumption reduces and battery life increases (the lower the internal resistance the lower the aging the longer the life).

	Out of the SoC window	Within the SoC window
F.C. [l/100km]	6.49	6.47
B.L. [km]	160,158	161,377

Table 4.4: Fuel consumption (F.C.) and battery life (B.L.) out of the optimal SoC window (SoC_0 = 25%) and within the optimal SoC window (SoC_0 = 84%). Results obtained with s_1 = [1.93,1] and s_2 = 88.2.

This dual advantage gives us a double operating margin: it is possible to use this margin to lower fuel consumption or to further increase battery life. With a new calibration of the ECMS it is possible to further lower fuel consumption. The increased battery life (from 160,158 to 161,377 km) can be used to force the ECMS to exploit more the electric part of the powertrain (to reduce fuel consumption). By looking at the results reported in Tab.4.5 it is possible to see that the *extra-km*, achieved by forcing the battery operates in the optimal SoC window, are cancelled with the new calibration and the fuel consumption is further reduced. In the other way around the advantage on the fuel consumption can be used to increase battery life.

	Re-calibrated ECMS
F.C. [l/100km]	6.45
B.L. [km]	159,619

Table 4.5: Fuel consumption (F.C.) and battery life (B.L.) with a new calibration of the ECMS. Results obtained with $s_1 = [1.93, 1]$ and $s_2 = 81.84$.

The same procedure is applied for the second optimal SoC window identified in fig.4.27. By selecting an initial state-of-charge of 63% the battery is forced to work within the window. The expected benefits are obviously lower than that obtained for the first window since the resistance is higher. It is true that for a SoC of 60% the discharging resistance reaches a minimum but it is also true that very small SoC fluctuations leads to a "vertical" increase of the discharge resistance. In

Tab.4.6 some important results are reported. The operation out of the SoC window is the same described before. If the battery, instead, operates within the second optimal SoC window some benefits can be obtained: fuel consumption reduces up to 6.47 l/100km while battery life increases until 160,971 km.

	Out of the SoC window	Within the SoC window
F.C. [l/100km]	6.49	6.47
B.L. [km]	160,158	160,971

Table 4.6: Fuel consumption (F.C.) and battery life (B.L.) out of the optimal SoC window ($SoC_0 = 25\%$) and within the second SoC window ($SoC_0 = 63\%$). Results obtained with $s_1 = [1.93{,}1]$ and $s_2 = 88.2$.

Even in this case the battery suffers less and surely the operating conditions are more favourable. The main difference with respect to the previous case has to be found in the obtained margin Tab.4.7. Now the margin is smaller and the new calibration of the ECMS has to take into account this feature. The idea is that less *km* can be used to reduce fuel consumption. The difference between the two windows reflects also in the new equivalence factors: in the first case the calibration of the EMCS is more aggressive and it has been obtained lowering the equivalence factor (s_2) up to 81.84. In the second case the "new-ECMS" exploits more the HEV potential but the calibration is more conservative.

	Re-calibrated ECMS
F.C. [l/100km]	6.46
B.L. [km]	159,999

Table 4.7: Fuel consumption (F.C.) and battery life (B.L.) with a new calibration of the ECMS. Results obtained with $s_1 = [1.93, 1]$ and $s_2 = 87.5$.

Conclusions

This study attempted to provide an answer to the question: "Are there realistic solutions to account for battery cycle-aging in the definition of the optimal HEV control strategy?". Several attempts have been made to give a credible answer to this question and still many researchers work on this theme. In HEVs the conventional internal combustion engine works in synergy with one or more electric machines. In this context the role of the control strategy is to find the best split possible contemporary satisfying external power demand. One of the main drivers that enables the diffusion of this solution is the fuel consumption reduction if compared with conventional powertrains. Fuel consumption can not be the only concern of the control strategy if a compromise has to be found.

For the aforementioned reasons also the control strategy should be hybrid meaning that two objectives have to be contemporary achieved. The first step of the work aims at presenting the major aging mechanisms happening within the lithium-ion batteries. The understanding of the performance fade mechanisms is cardinal and pivotal to describe what happens within the electrochemical system under very variegated operating conditions. *Xiong et al.* in [2] dissect in detail the *lithium ion batteries aging* with an emphasis on the effect of the operating condition. This knowledge is crucial to achieve an health-oriented control for HEV. *Wang et al.* in [18] investigate the effect of several parameters on battery aging by carrying out very accurate experimental tests. The experimental results have been used by the authors to establish a link between the charge processed by the battery, the operating conditions and the battery ageing. Definitely this model does not pretend to describe the physics and the chemistry of the side reaction rather it aims to represent them under a semi-empirical perspective. Its intrinsic simplicity represents also its greatest strength.

The model presented by *Wang et al.* has been firstly adapted to operate with a wider operating conditions spectrum (in terms of charge/discharge rate) and then embedded within a *State-of-Health* model. The *State-of-Health* is an index of battery-health and it is used as mainstream to evaluate the *remaining useful life* (RUL) of the battery. Different SoH estimation procedures presented in the literature ([23], [24]) in this work are compared, analyzed and used to built a

Simulink® model able to simulate the operation of a HEV on different driving scenarios. Since the very beginning it is important to assign the right meaning to the real number of cycles made by the battery and the number of cycles the battery might potentially withstand with (before end-of-life). The choices made in this phase severely affect the outcomes of the analysis in terms of battery life. The model of *Guzzella et al.* appears to be the least severe one while the model of *Anselma et al.* appears to be the most conservative one. The model chosen by the way represents an intermediate situation between the two and compares homogenous quantities in the evaluation of the SoH index.

In the second section of the thesis, instead, an innovative energy management strategy is presented and applied on a PHEV, namely the Jeep® Renegade 4xe Plug-In Hybrid. An extended version of the ECMS has been proposed to solve the optimal control problem and to establish the best possible power-split between the internal combustion engine and the electric machine. While the traditional version of the ECMS looks for a fuel-oriented solution of the control problem the proposed version offers a new perspective to look at the same problem. The proposed ECMS, infact, attempts to reach an optimal solution both in terms of fuel consumption and battery ageing leading to satisfactory results. Battery life increases with a moderate increase in the fuel consumption. The primary objective of the work has been to sensitize the control logic to the battery health while deciding the best control strategy. An health-conscious control strategy is the key to fully exploit the potential of HEVs; a fuel-only-oriented strategy could seriously threaten battery health, and safety, masking the advantages of electric propulsion.

The answer to the first question is definitely "Yes, there are!". The future HEVs control strategies will be increasingly careful to safeguard battery in operation in order to extend its useful life and to take at the same time the biggest possible advantage. Although the physico-chemical reactions happening within the battery are not always simply describable there are some effective instruments which allow to have reliable results.

Bibliography

[1] Michel Armand et al. «Lithium-ion batteries – Current state of the art and anticipated developments». In: *Journal of Power Sources* 479 (2020), p. 228708. ISSN: 0378-7753. DOI: `https://doi.org/10.1016/j.jpowsour.2020.228708`. URL: `https://www.sciencedirect.com/science/article/pii/S0378775320310120` (cit. on p. 2).

[2] Rui Xiong, Yue Pan, Weixiang Shen, Hailong Li, and Fengchun Sun. «Lithium-ion battery aging mechanisms and diagnosis method for automotive applications: Recent advances and perspectives». In: *Renewable and Sustainable Energy Reviews* 131 (2020), p. 110048. ISSN: 1364-0321. DOI: `https://doi.org/10.1016/j.rser.2020.110048`. URL: `https://www.sciencedirect.com/science/article/pii/S1364032120303397` (cit. on pp. 3–5, 7, 11–13, 15, 105).

[3] Mathias Storch, Severin Lukas Hahn, Jochen Stadler, Ramanathan Swaminathan, Dragoljub Vrankovic, Carsten Krupp, and Ralf Riedel. «Post-mortem analysis of calendar aged large-format lithium-ion cells: Investigation of the solid electrolyte interphase». In: *Journal of Power Sources* 443 (2019), p. 227243. ISSN: 0378-7753. DOI: `https://doi.org/10.1016/j.jpowsour.2019.227243`. URL: `https://www.sciencedirect.com/science/article/pii/S0378775319312364` (cit. on p. 4).

[4] Lydia Terborg, Sascha Weber, Franziska Blaske, Stefano Passerini, Martin Winter, Uwe Karst, and Sascha Nowak. «Investigation of thermal aging and hydrolysis mechanisms in commercial lithium ion battery electrolyte». In: *Journal of Power Sources* 242 (2013), pp. 832–837. ISSN: 0378-7753. DOI: `https://doi.org/10.1016/j.jpowsour.2013.05.125`. URL: `https://www.sciencedirect.com/science/article/pii/S0378775313009154` (cit. on p. 5).

[5] P.G. Balakrishnan, R. Ramesh, and T. Prem Kumar. «Safety mechanisms in lithium-ion batteries». In: *Journal of Power Sources* 155.2 (2006), pp. 401–414. ISSN: 0378-7753. DOI: `https://doi.org/10.1016/j.jpowsour.2005.

12.002. URL: https://www.sciencedirect.com/science/article/pii/S0378775305016629 (cit. on p. 7).

[6] Rachid Yazami and Yvan F Reynier. «Mechanism of self-discharge in graphite–lithium anode». In: *Electrochimica Acta* 47.8 (2002), pp. 1217–1223. ISSN: 0013-4686. DOI: https://doi.org/10.1016/S0013-4686(01)00827-1. URL: https://www.sciencedirect.com/science/article/pii/S0013468601008271 (cit. on p. 7).

[7] M. Kassem, J. Bernard, R. Revel, S. Pélissier, F. Duclaud, and C. Delacourt. «Calendar aging of a graphite/LiFePO4 cell». In: *Journal of Power Sources* 208 (2012), pp. 296–305. ISSN: 0378-7753. DOI: https://doi.org/10.1016/j.jpowsour.2012.02.068. URL: https://www.sciencedirect.com/science/article/pii/S0378775312004284 (cit. on pp. 7, 8).

[8] Marco-Tulio F. Rodrigues, Farheen N. Sayed, Hemtej Gullapalli, and Pulickel M. Ajayan. «High-temperature solid electrolyte interphases (SEI) in graphite electrodes». In: *Journal of Power Sources* 381 (2018), pp. 107–115. ISSN: 0378-7753. DOI: https://doi.org/10.1016/j.jpowsour.2018.01.070. URL: https://www.sciencedirect.com/science/article/pii/S0378775318300703 (cit. on p. 9).

[9] K. Jalkanen, J. Karppinen, L. Skogström, T. Laurila, M. Nisula, and K. Vuorilehto. «Cycle aging of commercial NMC/graphite pouch cells at different temperatures». In: *Applied Energy* 154 (2015), pp. 160–172. ISSN: 0306-2619. DOI: https://doi.org/10.1016/j.apenergy.2015.04.110. URL: https://www.sciencedirect.com/science/article/pii/S0306261915005735 (cit. on p. 9).

[10] Thomas Waldmann, Marcel Wilka, Michael Kasper, Meike Fleischhammer, and Margret Wohlfahrt-Mehrens. «Temperature dependent ageing mechanisms in Lithium-ion batteries – A Post-Mortem study». In: *Journal of Power Sources* 262 (2014), pp. 129–135. ISSN: 0378-7753. DOI: https://doi.org/10.1016/j.jpowsour.2014.03.112. URL: https://www.sciencedirect.com/science/article/pii/S0378775314004352 (cit. on p. 9).

[11] Ting Guan, Shun Sun, Yunzhi Gao, Chunyu Du, Pengjian Zuo, Yingzhi Cui, Lingling Zhang, and Geping Yin. «The effect of elevated temperature on the accelerated aging of LiCoO2/mesocarbon microbeads batteries». In: *Applied Energy* 177 (2016), pp. 1–10. ISSN: 0306-2619. DOI: https://doi.org/10.1016/j.apenergy.2016.05.101. URL: https://www.sciencedirect.com/science/article/pii/S0306261916306985 (cit. on p. 9).

[12] Simon F. Schuster, Tobias Bach, Elena Fleder, Jana Müller, Martin Brand, Gerhard Sextl, and Andreas Jossen. «Nonlinear aging characteristics of lithium-ion cells under different operational conditions». In: *Journal of Energy Storage* 1 (2015), pp. 44–53. ISSN: 2352-152X. DOI: https://doi.org/10.1016/j.est.2015.05.003. URL: https://www.sciencedirect.com/science/article/pii/S2352152X15000092 (cit. on pp. 9–11).

[13] J. Vetter et al. «Ageing mechanisms in lithium-ion batteries». In: *Journal of Power Sources* 147.1 (2005), pp. 269–281. ISSN: 0378-7753. DOI: https://doi.org/10.1016/j.jpowsour.2005.01.006. URL: https://www.sciencedirect.com/science/article/pii/S0378775305000832 (cit. on p. 10).

[14] Shoichiro Watanabe, Masahiro Kinoshita, Takashi Hosokawa, Kenichi Morigaki, and Kensuke Nakura. «Capacity fading of LiAlyNi1xyCoxO2 cathode for lithium-ion batteries during accelerated calendar and cycle life tests (effect of depth of discharge in charge–discharge cycling on the suppression of the micro-crack generation of LiAlyNi1xyCoxO2 particle)». In: *Journal of Power Sources* 260 (2014), pp. 50–56. ISSN: 0378-7753. DOI: https://doi.org/10.1016/j.jpowsour.2014.02.103. URL: https://www.sciencedirect.com/science/article/pii/S0378775314003048 (cit. on p. 10).

[15] B Markovsky, A Rodkin, Y.S Cohen, O Palchik, E Levi, D Aurbach, H.-J Kim, and M Schmidt. «The study of capacity fading processes of Li-ion batteries: major factors that play a role». In: *Journal of Power Sources* 119-121 (2003). Selected papers presented at the 11th International Meeting on Lithium Batteries, pp. 504–510. ISSN: 0378-7753. DOI: https://doi.org/10.1016/S0378-7753(03)00274-X. URL: https://www.sciencedirect.com/science/article/pii/S037877530300274X (cit. on p. 11).

[16] C. Pastor-Fernández, W. Dhammika Widanage, J. Marco, M. Gama-Valdez, and G. H. Chouchelamane. «Identification and quantification of ageing mechanisms in Lithium-ion batteries using the EIS technique». In: *2016 IEEE Transportation Electrification Conference and Expo (ITEC)*. June 2016, pp. 1–6. DOI: 10.1109/ITEC.2016.7520198 (cit. on pp. 14, 15).

[17] Dirk Uwe Sauer and Heinz Wenzl. «Comparison of different approaches for lifetime prediction of electrochemical systems—Using lead-acid batteries as example». In: *Journal of Power Sources* 176.2 (2008). Selected Papers presented at the10th ULM ElectroChemical Days, pp. 534–546. ISSN: 0378-7753. DOI: https://doi.org/10.1016/j.jpowsour.2007.08.057. URL: https://www.sciencedirect.com/science/article/pii/S0378775307016199 (cit. on pp. 16–23, 38).

[18] John Wang, Ping Liu, Jocelyn Hicks-Garner, Elena Sherman, Souren Soukiazian, Mark Verbrugge, Harshad Tataria, James Musser, and Peter Finamore. «Cycle-life model for graphite-LiFePO4 cells». In: *Journal of Power Sources* 196.8 (2011), pp. 3942–3948. ISSN: 0378-7753. DOI: https://doi.org/10.1016/j.jpowsour.2010.11.134. URL: https://www.sciencedirect.com/science/article/pii/S0378775310021269 (cit. on pp. 24–37, 39, 105).

[19] I Bloom et al. «An accelerated calendar and cycle life study of Li-ion cells». In: *Journal of Power Sources* 101.2 (2001), pp. 238–247. ISSN: 0378-7753. DOI: https://doi.org/10.1016/S0378-7753(01)00783-2. URL: https://www.sciencedirect.com/science/article/pii/S0378775301007832 (cit. on pp. 24, 27, 39).

[20] R. Spotnitz. «Simulation of capacity fade in lithium-ion batteries». In: *Journal of Power Sources* 113.1 (2003), pp. 72–80. ISSN: 0378-7753. DOI: https://doi.org/10.1016/S0378-7753(02)00490-1. URL: https://www.sciencedirect.com/science/article/pii/S0378775302004901 (cit. on pp. 29, 33).

[21] R.B Wright et al. «Calendar- and cycle-life studies of advanced technology development program generation 1 lithium-ion batteries». In: *Journal of Power Sources* 110.2 (2002), pp. 445–470. ISSN: 0378-7753. DOI: https://doi.org/10.1016/S0378-7753(02)00210-0. URL: https://www.sciencedirect.com/science/article/pii/S0378775302002100 (cit. on pp. 29, 33).

[22] M Broussely, S Herreyre, P Biensan, P Kasztejna, K Nechev, and R.J Staniewicz. «Aging mechanism in Li ion cells and calendar life predictions». In: *Journal of Power Sources* 97-98 (2001). Proceedings of the 10th International Meeting on Lithium Batteries, pp. 13–21. ISSN: 0378-7753. DOI: https://doi.org/10.1016/S0378-7753(01)00722-4. URL: https://www.sciencedirect.com/science/article/pii/S0378775301007224 (cit. on pp. 29, 33).

[23] S. Ebbesen, P. Elbert, and L. Guzzella. «Battery State-of-Health Perceptive Energy Management for Hybrid Electric Vehicles». In: *IEEE Transactions on Vehicular Technology* 61.7 (2012), pp. 2893–2900. DOI: 10.1109/TVT.2012.2203836 (cit. on pp. 38, 39, 41–43, 52–55, 84, 105).

[24] P. Anselma, P. Kollmeyer, G. Belingardi, and A. Emadi. «Multitarget Evaluation of Hybrid Electric Vehicle Powertrain Architectures Considering fuel Economy and Battery Lifetime». In: *SAE International* (2020, doi=https://doi-org.ezproxy.biblio.polito.it/10.4271/2020-37-0015) (cit. on pp. 41–43, 45–55, 58, 61, 105).

[25] S.Onori, L.Serrao, and G. Rizzoni. *Hybrid Electric Vehicles: Energy Management Strategies*. Springer, 2016 (cit. on pp. 66–71, 76, 80–83).

[26] Li J., Huber T., and C. Beidl. «Predictive Multi-Objective Operation Strategy Considering Battery Cycle Aging for Hybrid Electric Vehicles». In: *SAE International J. Alt. Power. 7(3):217-232* (2018,) (cit. on pp. 75, 77).